

DEPHASED RAPID GROUND STATE MAPPING:
ADVANCING ORCA QUANTUM MEMORIES

Author

OTTO T. P. SCHMIDT

Supervised by

DR SARAH. E. THOMAS
PROF. IAN A. WALMSLEY
PROF. TILMAN ESSLINGER

A Thesis submitted in fulfillment of requirements for the degree of
Master of Science in Quantum Engineering

Department of Physics
Eidgenössische Technische Hochschule Zürich
2024

Abstract

The usage of quantum light, i.e., single photons carrying information, has become important in a variety of applications. Prominent examples are the use of entanglement and squeezing in quantum computation, but also in quantum communication.

Many of these applications require the storage of quantum states of light, be it for synchronisation of photonic inputs or manipulation of light states. The storage of single photons or weak coherent states of light requires the use of a quantum memory.

Here we report on the conception and implementation of a quantum memory protocol. We propose an extension of the established ORCA quantum memory, called DRAGON, which seeks to overcome crucial limitations of ORCA.

We present the theoretical framework of the model and its experimental implementation. Both theory and experiment are put into context with numerical results from simulations.

Declaration of Originality

I hereby declare that the work presented in this thesis is my own unless otherwise stated. To the best of my knowledge the work is original and ideas developed in collaboration with others have been appropriately referenced.

Copyright Declaration

The copyright of this thesis rests with the author and is made available under a Creative Commons Attribution Non-Commercial No Derivatives licence. Researchers are free to copy, distribute or transmit the thesis on the condition that they attribute it, that they do not use it for commercial purposes and that they do not alter, transform or build upon it. For any reuse or redistribution, researchers must make clear to others the licence terms of this work.

Acknowledgments

There are different parties that I need to thank in particular.

First, I would like to thank the PQI group at Imperial College London. Not only for hosting me, but also for really letting me work independently on many different tasks, be it numerical, theoretical or experimental.

My time at Imperial would not have been possible at all had Ian not offered me the position. Thank you, Ian, for the trust!

Then at Imperial, research for me would have been impossible without Sarah. Sarah, you have been a very strong supervisor during my stay. It was a pleasure learning from you!

My stay also corroborated my decision to switch more to theory and simulations. I was able to explore the various theoretical and numerical facets of my project because Mikhael was doing most of the hard work in the lab. I have learned a lot of experimental tricks from you. You have been a very important buddy for me during my stay!

Whenever I had a question I could ask the dream team Ilse and Paul. Especially Paul's expertise on theoretical and numerical questions was irreplaceable. My life in the office at Imperial would have been very dull, were it not for Shisheng sitting next to me. We had very good and inspirational talks about different topics.

On the other side, in Switzerland, I have to thank Tilman Esslinger for hosting me as well. The mandatory monthly report was a good motivation to start writing down theory and experiments very early on. I am very pleased to have had such an experienced supervisor at ETH Zürich in the fields of atomic physics and quantum optics.

Contents

Abstract	i
Declaration of Originality	iii
Copyright Declaration	v
Acknowledgments	vii
List of Acronyms	xiii
List of Figures	xv
1 Introduction	1
1.1 Outline	1
1.2 Optical quantum memories	2
1.2.1 Applications of optical quantum memories	3
1.2.2 Metrics for optical quantum memories	4
1.2.3 Quantum memory platforms	5
1.3 ORCA	7
1.4 DRAGON	8
2 Theory of DRAGON	11
2.1 Coherences and optical Bloch equations	12
2.1.1 System Hamiltonian	12
2.1.2 Evolution of coherences	14
2.1.3 Photon propagation	16
2.1.4 Macroscopic coherences	18
2.1.5 Optical Bloch equations for ORCA	19
2.1.6 Doppler dephasing	21
2.1.7 Ground state mapping	22
2.1.8 Pulsed rephasing	23
2.1.9 Optical Bloch equations for DRAGON	24

2.2	Optical depth	26
2.3	Fluorescence noise in DRAGON	28
2.4	Reduced collective decay via Doppler dephasing	29
3	Hyperfine optical pumping	33
3.1	Theory of optical pumping	34
3.2	Atomic beam transit	36
3.3	Implementation of optical pumping	38
3.3.1	Spectrum calibration	39
3.3.2	Pulsed pumping	40
3.3.3	CW pumping	42
3.4	Simulation of optical pumping with <i>ElecSus</i>	42
3.4.1	Pulsed pumping	44
3.4.2	CW pumping	46
4	Implementation of DRAGON	49
4.1	Setup	50
4.1.1	ORCA	50
4.1.2	Pulse generation and synchronisation	51
4.1.3	DRAGON	52
4.1.4	EDFA	52
4.2	Operation of the memory	54
4.2.1	Pulse energy characterisation	54
4.2.2	CW background characterisation	55
4.2.3	CW leakage readout	56
4.2.4	Retrieval of stored signals	59
4.3	Simulation of optical Bloch equations	60
4.3.1	Control Rabi frequency	60
4.3.2	Optical depth	62
4.3.3	Frequency detuning	63
4.3.4	Simulation of storage and retrieval	63
	Conclusions	67
	A Appendix	69

B Additional Appendix	73
B.1 Time bin qubit	73
Bibliography	75

List of Acronyms

QM quantum memory

ORCA Off-Resonant Cascaded Absorption

DRAGON Dephased RApid GrOuNd state mapping

QR quantum repeater

EIT electromagnetically induced transparency

FWM four-wave-mixing

ORR off-resonant Raman

OBE optical Bloch equations

RWA rotating wave approximation

TLS two-level system

OD optical depth

AWG arbitrary waveform generator

EOM electro-optical modulator

EDFA erbium-doped fiber amplifier

SNSPD superconductor-nanowire single photon detector

RI read in

RO read out

CG Clebsch-Gordan

PQI Photonic Quantum Information Lab

GSM ground state mapping

FN fluorescence noise

List of Figures

1.1	Simplified level diagram for DRAGON for mapping from $F = 1$ to $F = 2$. The initial, intermediate, storage, mapping state and rephasing state are denoted $ g\rangle, e\rangle, s\rangle, b\rangle$ and $ d\rangle$, respectively. The symbols $\mathcal{E}_s, \Omega_c, M1, M2$ and Ω_d denote the signal and control fields, the mapping fields and rephasing field, respectively.	10
2.1	Unwanted read out \mathcal{E}_R of the coherence during the ground state mapping.	23
2.2	Schematic of phase accumulation in pulsed rephasing. The green lines represent the phase evolution of the coherence S_{gs} for different velocity classes, the violet lines the phase evolution of S_{gd} for the same velocity classes.	24
2.3	Schematic of pulse sequence in DRAGON with GSM and pulsed rephasing. The upper level diagrams indicate the established coherence in each step. The pulse sequence in the lower part shows the corresponding application of pulses.	25
2.4	Left: ORCA level diagram. The signal \mathcal{E}_s is at $\lambda_s = 780$ nm, the control Ω_c at $\lambda_c = 776$ nm. The detuning from resonance is denoted Δ_s and Δ_c . Right: DRAGON level diagram with rephasing state $ d\rangle$. This level diagram is similar to the ORCA diagram, but it uses $\lambda_c = 1529$ nm. Additionally, the mapping fields M1, M2 and Ω_d are introduced with their respective detunings Δ_{M1}, Δ_{M2} and Δ_d	27
2.5	Schematic of fluorescence noise in DRAGON for initial state $F = 1$ and mapping state $F = 2$	29
3.1	Simplified three level system for pumping of hyperfine level $F = 1$. See Sec. 3.1 for definition of symbols.	34
3.2	Evolution of atoms with $R = 100$ μm and $T = 350$ K. The atoms that are initially inside the pump beam are in blue, the atoms initially outside in orange. The left part shows the positions after initialisation, the right part shows the positions after evolution of t_{pump} . The black arrows indicate the time evolution.	37
3.3	Average exposure of atoms within the pump profile as function of time. The exposure time of atoms that were initialised inside the beam is shown in the blue graph, the exposure time of atoms that were initially outside the beam in orange. The green line shows the average exposure for both green and orange dots at a specific time.	38
3.4	Spectrum of reference cell containing Rubidium in natural abundance. The hyperfine states corresponding to each absorption dip are annotated.	39
3.5	Transmission spectra of the vapour cell with different pump powers taken from oscilloscope data. Note that due to data calibration the transmission is normalised differently.	40
3.6	Transmission spectrum for pumped region for $I = 2$ mW.	41
3.7	Transmission spectra for optically pumping a) $F = 1$ and b) $F = 2$	41
3.8	Transmission spectrum for optically pumping $F = 1$ with $I = 100$ mW and $T \approx 40$ $^\circ\text{C}$	42
3.9	Transmission spectrum for CW pumping of $F = 1$ with $I = 14$ mW and $T \approx 40$ $^\circ\text{C}$	43

3.10	Data for pulsed pumping of level $F = 1$ for $T \approx 40$ °C. In each sub-figure the upper graph is the fitted spectrum, the lower graph shows the fitting residuals.	45
3.11	Fit and data for pulsed pumping of level $F = 2$ for $T \approx 40$ °C with $I = 230$ mW. The extracted pumping efficiency is $\eta_{F=2} = 0.989$	46
3.12	Fit and data for CW pumping of level $F = 1$ for $T \approx 40$ °C with $I = 14$ mW. The extracted pumping efficiency is $\eta_{F=2} = 0.977$	47
3.13	Efficiency map for transmission spectrum. a) The spectrum around pumping transition with and without pumping is obtained. b) Using <i>ElecSus</i> , the distance from total absorption is mapped to pumping efficiency.	47
3.14	Data for CW pumping with $I = 15$ mW and $T \approx 40$ °C.	48
4.1	Installed ORCA setup	51
4.2	Installed DRAGON setup, no fields $M1$, $M2$	53
4.3	EDFA input intensity with (a) the amplified output and (b) the gain profile. The current is set to $A_{EDFA} = 500$ mA.	53
4.4	RI pulse energies for different pulse separations. The x-axis and y-axis show the RI and RO amplitudes, respectively, i.e., 10 denotes an amplitude of $1/\sqrt{10}$. The color bar denotes the pulse energies in pJ.	56
4.5	RO pulse energies for different pulse separations. The x-axis and y-axis show the RI and RO amplitudes, respectively, i.e., 10 denotes an amplitude of $1/\sqrt{10}$. The color bar denotes the pulse energies in pJ.	57
4.6	CW background intensity in mW for 50 ns separation. The x-axis and y-axis show the RI and RO amplitudes, respectively, i.e., 10 denotes an amplitude of $1/\sqrt{10}$. The color bar denotes the CW background power in mW.	58
4.7	Detection of signal for read in for different separations τ_{sep} . The inset shows a zoom of the right tail of the various traces.	59
4.8	Storage and retrieval detection for 1.5 ns storage time with pulse energies $\epsilon_{RI/RO}$ and read in (RI), total and read out (RO) efficiencies η_{RI} , η and η_{RO} , respectively. Vapour cell at $T \approx 66$ °C. The red shaded region indicates the integration region for the read out efficiency.	61
4.9	Simulation of signal and signal leakage for 1.5 ns storage time with pulse energies $\epsilon_{RI/RO}$ and RI, total and RO efficiencies η_{RI} , η and η_{RO} , respectively. Vapour cell at $T \approx 66$ °C. The red shaded region indicates the integration region for RI, the purple shaded region the RO region.	64
4.10	Simulation of the memory with RI and RO efficiencies as a function of RI and RO pulse energies. Red, light red, black, cyan and blue indicate an offset of $\delta\tau = 0.2$ ns, $\delta\tau = 0.1$ ns, $\delta\tau = 0$ ns, $\delta\tau = -0.1$ ns and $\delta\tau = -0.2$ ns, respectively.	65
A.1	Intensity of pulse sequence for different pulse separations.	70
A.2	RI control pulses (dashed, coloured) and signal pulse (solid). Red, light red, black, cyan and blue indicate an offset of $\delta\tau = 0.2$ ns, $\delta\tau = 0.1$ ns, $\delta\tau = 0$ ns, $\delta\tau = -0.1$ ns and $\delta\tau = -0.2$ ns, respectively.	71

B.1	Integration of photon counts for two full Piezo scans (2 ms). The upper graph shows the interference of the early and late pulse, the middle the transmission of the early pulse and the lower graph the transmission of the late pulse.	73
B.2	Sinusoidal fit to the oscillation in the interference peak. The extracted frequency is 99.53 Hz with a visibility of 0.7356.	74

1

Introduction

Contents

1.1 Outline	1
1.2 Optical quantum memories	2
1.2.1 Applications of optical quantum memories	3
1.2.2 Metrics for optical quantum memories	4
1.2.3 Quantum memory platforms	5
1.3 ORCA	7
1.4 DRAGON	8

1.1 Outline

In this thesis we present theoretical, numerical and experimental work regarding the quantum memory (QM) protocol Dephased RAPid GrOuNd state mapping (DRAGON). As we will show, the DRAGON memory is an architecture based on a closely related protocol, the Off-Resonant Cascaded Absorption (ORCA). Many sections of this work will therefore also outline concepts regarding the well established ORCA protocol.

The thesis is split into three thematic parts. After introducing the idea of QM and its applications in Chapter 1, we describe in Ch. 2 the theoretical framework that is necessary to understand DRAGON.

In Ch. 3 we present the concept of hyperfine optical pumping and its importance to the DRAGON protocol. Here we give a theoretical outline and experimental results. Furthermore, we provide numerical simulations, to put the experimental findings into context.

Finally, in Ch. 4 we present the experimental implementation of DRAGON. This includes various investigations concerning the operation of the memory. Again, to put the experimental results into context, we use the framework of optical Bloch equations (OBE)s given in Ch. 2 to simulate and reproduce the experimental results for the memory operation.

The thesis concludes with a summary of achievements, their relevance to ongoing research and open questions in the field.

Appendix A provides supplementary figures to certain experiments.

Note that during the course of this project a another project was started, the demonstration of storage of time bin qubits using ORCA memories. This thesis will not include this work as it is so far inconclusive and mainly a data analysis. However, in order to provide evidence of the work, Appendix B provides the main graphs of the conducted work.

1.2 Optical quantum memories

In the past decades, quantum technologies have been developed with ever increasing speed. This includes advances in the fields of quantum metrology, quantum computation and quantum communication. A very important factor to this rapid development is the advancement in (nano) fabrication of scientific devices and measurement technologies. This technological progress allows researchers to extend the control from large quantum systems to its smallest constituents. This can be electrons, quasi-particles such as excitons or polaritons, photons and many more.

However, besides the development of scientific technology, the demand for precise control over quantum systems has also increased. The reasons for that include the development of feasible business plans and the commercialisation of quantum mechanical concepts. Furthermore, the scientific progress in the domain of quantum technologies has also acquired a geopolitical dimension, as more and more nations realise the impact of such technologies.

Within the field of quantum technologies, the advance and interest in applications of quantum information have been especially strong, mainly driven by the fields of quantum computation and quantum communication.

The various existing proposals in applied quantum information not only differ in their domain of applications but also in the way they make use of quantum mechanics. While in quantum computa-

tion with superconducting circuits the tunneling properties of electrons across Josephson junctions [1] is the key concept, the non-classical features of squeezed light in Gaussian Boson Sampling [2] are the most important ingredients.

The area of quantum technologies that uses non-classical features of light is called quantum photonics. This area is especially interesting for quantum computation and communication, as light allows for the highest processing speeds and only a small interaction with the environment. Furthermore, the technology for propagation of photonic signals is well established and optical fibers with low transmission loss are available.

In quantum photonics, not only the spatial control of photons is important, but also their temporal control. This includes the ability to store photons and to have an on-demand access to photons. An optical QM seeks to establish this control.

Temporal control over photons and the information encoded in them enables a variety of applications. The following section will give a few instructive examples of such applications.

1.2.1 Applications of optical quantum memories

Optical quantum memories are devices that map photonic information to an atomic/matter coherence, and are critical in many aspects of photonic quantum information. Here we present a non-exhaustive list of possible applications of an optical QM. It is important to note that each application introduces different constraints on memory performance.

Local synchronisation of photon sources

Many photonic quantum technologies require synchronised on-demand access to single photons. This can be, for instance, photonic input states in quantum computation as recently demonstrated by the company *Quandela* on a photonic chip [3]. Synchronised on-demand photons are also required to perform Hong-Ou-Mandel type quantum interference, where the temporal control of incoming photons is crucial [4].

An example of an on-demand single photon emitter are quantum dots with Purcell-enhanced emission rates [5]. Creation of temporally synchronous photons is therefore possible without a QM. However, if photons arrive from previous non-synchronous probabilistic processes, a QM is the only option to synchronise these photons.

This process of synchronisation is called local synchronisation and refers to the storage and simultaneous release of temporally distributed incoming photons. Since the synchronisation remains

local, the requirements on the memory storage time are not very strong.

Therefore, by introducing an optical QM, temporal multiplexing of single photons is possible and the synchronous arrival of photons becomes a controllable and scalable process [6].

Quantum repeaters for quantum teleportation

A quantum repeater (QR) addresses the problem of sharing quantum information among spatially distributed nodes of a network. Classically, the loss in a channel can be mitigated by amplifying the signal along the path of transmission. This, however, is not possible for quantum information due to the non-cloning theorem.

A possible way to exchange quantum information is via quantum teleportation. Here the direct transmission of quantum information is substituted by a transmission of classical bits. This protocol, however, requires a shared entangled resource of the participating parties [7].

The distribution of entanglement over large distances can be achieved with optical QMs [8] by performing protocols like the Duan-Lukin-Cirac-Zoller protocol [9]. In this protocol, a photonic herald can establish an entanglement of coherences in atomic ensembles over large distances. These atomic ensembles perform the role of an optical QM.

Recently, a few experiments implemented such networks using optical QMs as QR. Most notably a network in Boston (US) with a distributed entanglement over up to 40 km [10] and in Hefei (China) with a multi-node entanglement over up to 12.5 km [11].

1.2.2 Metrics for optical quantum memories

Following [12], we can identify a number of measures to benchmark QMs. In this section we focus on a specific class of optical QMs, optically controlled ensemble-based QMs.

Although there are more metrics that apply to optical QMs, we will only introduce the metrics below, as they are sufficient to benchmark the presented memory protocols ORCA and DRAGON:

- **Efficiency:** the efficiency of an optical QM consists in the efficiency of the two main processes of a memory, the read in (RI) and read out (RO) efficiencies, η_{RI} and η_{RO} , respectively. The RI efficiency is determined by the ability of the memory to store any incoming photonic information, the RO efficiency refers to the ability to retrieve the stored information. The total efficiency of the memory η takes both of the processes into account, such that $\eta = \eta_{RI}\eta_{RO}$.

High efficiencies for storage of single photons in a QM are important to make the on-demand retrieval an approximately deterministic process. Low efficiencies for RI/RO also limit the scalability of processes that rely on QMs.

- **Bandwidth:** the memory bandwidth δ measures the ability of the memory to store the signal photon spectral intensity. The bandwidth can be used to assess the compatibility of a memory with a (pulsed) optical signal.

The bandwidth of a QM is important as it limits the spectral profile of storable photons. This is especially important when storing temporally short light pulses, as the bandwidth increases with decreasing temporal pulse width. A high memory bandwidth would therefore allow for high processing speed of photon pulses.

- **Memory lifetime:** the memory lifetime τ gives the storage time for the RO signal to reach $1/e$ of its maximum value. Often the lifetime determines for what application a memory can be used.

While for the purpose of local synchronisation a long lifetime is not necessary, it becomes important for quantum repeaters, when entanglement is generated over far distances.

- **Noise:** reading out the information stored in the memory should only produce the information from the signal photon. This will not be true if the memory protocol introduces optical noise photons.

The noise profile of different optical QM platforms varies. While some QM are inherently noise-free, others introduce noise that can be difficult to filter out.

1.2.3 Quantum memory platforms

In the past years a plethora of QM technologies has been developed to establish the properties listed in Sec. 1.2.2. As in the previous section, we focus on optically controlled memories based on atomic ensembles and specifically protocols that are similar to ORCA.

The presented platforms utilise a Λ -level structure of energy levels in the atomic ensemble.

For the Λ -level structure we use the notation where $|g\rangle$ and $|s\rangle$ are the two ground states and $|e\rangle$ is the excited state.

Electromagnetically Induced Transparency

An electromagnetically induced transparency (EIT) in atomic ensembles occurs when an optical signal, typically absorbed at wavelengths resonant with the $|g\rangle \rightarrow |e\rangle$ atomic transition, experiences no or reduced absorption by the ensemble and a reduction in group velocity. This effect is caused by the introduction of a second, strong optical control field, which couples the excited state $|e\rangle$ and $|s\rangle$ of the atoms. While the $|e\rangle \rightarrow |s\rangle$ transition is dipole-allowed, the $|s\rangle \rightarrow |g\rangle$ transition is dipole-forbidden, enabling the transparency and the slowing of the incident signal field.

A quantum memory based on EIT uses this transparency window of the atomic ensemble to "stop" the propagation of light.

A control field with a duration longer than that of the signal field is applied to the medium, arriving earlier than the signal. This creates a spectral transparency window at the signal frequency. As the signal field enters the medium, the transparency window is gradually closed by attenuating the control field adiabatically. This process compresses and traps the signal field within the medium, resulting in a superposition of the states $|s\rangle$ and $|e\rangle$.

Efficiencies in EIT memories can reach up to 92 % [13] and lifetimes of up to 1 min have been demonstrated [14]. An EIT memory can have bandwidths up to 660 MHz [15]. However, the Λ -structure of EIT memories introduces significant four-wave-mixing (FWM) [16].

Off-resonant Raman

The off-resonant Raman (ORR) memory protocol [17] is particularly effective for storing and retrieving broadband photons. In a typical Λ -level system, a strong control field, detuned from the excited state $|e\rangle$ by an offset Δ , facilitates a two-photon transition between the ground state $|g\rangle$ and the storage state $|s\rangle$ via stimulated emission. During storage, the signal photon, also detuned by Δ from the $|g\rangle \rightarrow |e\rangle$ transition, is spatio-temporally overlapped with the control field and mapped onto a collective spin wave excitation. For retrieval, a retrieval field (usually the same as the control field) is applied to the atomic ensemble, deterministically releasing the stored photon and completing the retrieval process

ORR can reach bandwidths up to 1 THz [18]. However, due to the large detuning, ORR suffers from FWM.

1.3 ORCA

ORCA is a memory platform that is based on an ensemble of atoms to store light pulses [19]. For the storage of single photons, a warm vapour of Alkali atoms is used.

In ORCA, the signal photon is stored in an atomic coherence between a ground state $|g\rangle$ and a storage state $|s\rangle$ within the low energy state manifold (using the excited state $|e\rangle$ of the D1 or D2 lines of the Alkali atom as intermediate state). The excitation to the storage state is achieved by temporally overlaying the signal field with a counter-propagating strong, classical control field (see Sec. 2 for details). This constitutes a two-photon transition.

The stored coherence is mapped to an optical field at signal wavelength immediately after a read out control pulse is applied. This makes ORCA an on-demand memory.

The name off-resonant cascaded absorption refers to two characteristic features of ORCA. First, the two-photon transition for storage of the input signal is off-resonant with the intermediate state $|e\rangle$. This guarantees that the atomic polarisation in the ensemble follows the pulse envelope, which allows for storage of high bandwidth photons. Second, cascaded absorption is a reference to the ladder structure of energy levels.

ORCA is a strong contender platform for QMs. Compared to other QMs based on atomic ensembles it is inherently protected against four-wave mixing [19]. This follows from the ladder structure of used energy levels: there is no scattering process that could populate the storage state, i.e., no noise in form of Stokes or anti-Stokes photons. Furthermore, since the storage state is a doubly-excited state, there will be no population due to thermal excitation. Therefore, the ensemble does not need to be optically pumped before initialising the memory protocol.

The ORCA memory is operated under ambient conditions, with required vapour temperatures of under 100 °C, i.e., no cryogenic systems are required.

Compared to Λ -type protocols, the bandwidth of ORCA is not fundamentally limited by the ground state splitting since storage and ground state are well separated in frequency. Since the ground states in e.g. ORR need to be addressed separately, the control field needs to have a smaller bandwidth than the frequency separation of the two ground states. In ORCA this does not apply since the ground and storage state are separated by hundreds of THz. However, there is still a limitation in bandwidth for ORCA: in the two-photon read in process, the intermediate state $|e\rangle$ should not be populated, as this reduces the read in efficiency. To avoid that, there should be no overlap of the atomic linewidth of the intermediate state and the spectral shape of the signal photon. This is

achieved by detuning the signal from resonance with the transition to the intermediate state. For a given detuning, the bandwidth of the signal photon is therefore limited.

In terms of compatibility, ORCA can be used for different wavelengths with different bandwidths. The bandwidth of ORCA is mostly determined by the bandwidth of the control pulse, but the detuning from the intermediate state is also a factor. For ^{87}Rb , using the states $|5S_{1/2}\rangle$ and $|5D_{5/2}\rangle$ for the ground and storage state, respectively, the signal light field can have a wavelength of $\lambda_s = 780$ nm or $\lambda_s = 776$ nm [20]. On the other hand, using the states $|g\rangle = |5S_{1/2}\rangle$ and $|s\rangle = |4D_{5/2}\rangle$, the signal can be $\lambda_s = 780$ nm or $\lambda_s = 1529$ nm. The last version of ORCA is referred to as telecom ORCA [21], which is especially interesting as the signal is in the low-loss telecommunication C-band.

ORCA is a memory that stores the temporal information of incoming signals. This can be information encoded in the spatio-temporal profile of the signal pulse, such as Hermite-Gaussian modes. It is important to point out that a single ORCA memory cannot store information carried in photonic polarisation. This is due to the nature of the atomic coherence.

Due its ladder structure however, ORCA has a limitation in lifetime. While Λ -type memories can use a different ground state for storage, the storage state of ORCA is a doubly-excited state. In ^{87}Rb , the lifetime of $|s\rangle = |5D_{5/2}\rangle$ is $\tau = 238$ ns and for $|s\rangle = |4D_{5/2}\rangle$ it is $\tau = 89$ ns. Even if no other channel of decoherence existed, the ORCA storage time could not exceed the lifetime of the storage state.

However, even if the limitation in lifetime was non-existent, the created atomic coherence between ground and storage state would lose its initial phase relation over time. This dephasing is a result of the movement of atoms in the atomic ensemble at non-zero temperatures and is referred to as Doppler dephasing (see Sec. 2.1.6).

1.4 DRAGON

The most obvious limitation of ORCA is the fundamental limit of storage time due to the low lifetimes of the storage state, as outlined in Sec. 1.3. In order to overcome this problem, a novel memory scheme has been developed in the Photonic Quantum Information Lab (PQI) at Imperial College London, the DRAGON memory.

Like the telecom ORCA, DRAGON utilises the D2 line of ^{87}Rb for ground and excited states, and the state $|4D_{5/2}\rangle$ as the storage state. However, this new protocol extends ORCA by adding

a ground state mapping (GSM). The GSM refers to the transfer of the coherence to a stable hyperfine ground state in $|5S_{1/2}\rangle$. Depending on the initial hyperfine state $|g\rangle = |5S_{1/2}, F\rangle$, the final state of the mapping procedure will be $|b\rangle = |5S_{1/2}, F'\rangle$ (see Fig. 1.1). Once the atoms that constitute the spin wave are mapped to this state, there is no allowed electric dipole transition for spontaneous decay. Dephasing of the spin wave can now only occur e.g. via spin exchange collisions (see Sec. 3.2).

Besides GSM, another novel technique is introduced in DRAGON, the pulsed rephasing of the ensemble. This technique is used to reverse dephasing of the ensemble due to the non-zero temperature of the atomic ensemble. In order to rephase the ensemble, an additional state is required, the rephasing state $|d\rangle$ (see Fig. 1.1).

The acronym stands for Dephased RApid GrOund state mapping and again refers to key characteristics of the protocol. The dephasing refers to the fact that during the ground state mapping we deliberately use a dephased ensemble to reduce noise in the process. This is explained in more detail in Sec. 2.1.9 and 2.4. Rapid ground state mapping refers to the fact that the GSM can be performed resonantly with moderate light field intensities and in short time.

While in ORCA there was no preparation necessary prior to memory operation, the GSM in DRAGON requires a depopulation of the mapping state $|b\rangle$. To depopulate this state, we need to optically empty the state using hyperfine pumping. This is done before the pulse sequence for the memory commences.

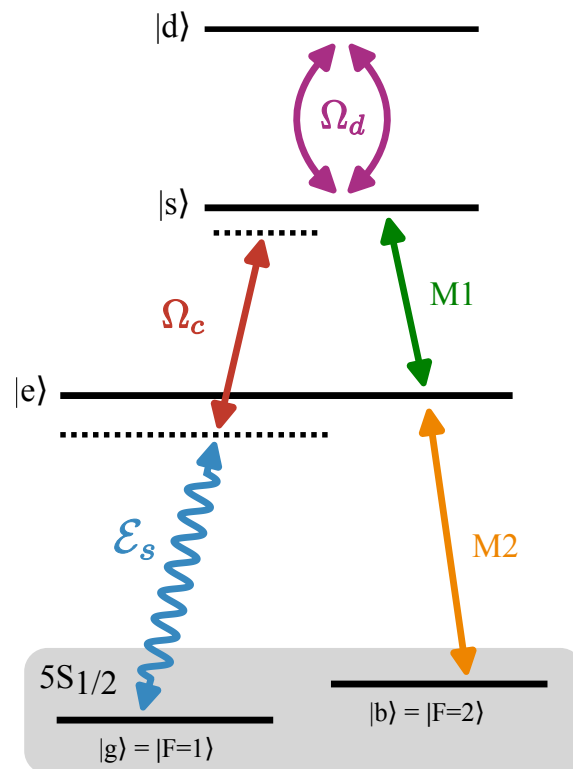


Figure 1.1: Simplified level diagram for DRAGON for mapping from $F = 1$ to $F = 2$. The initial, intermediate, storage, mapping state and rephasing state are denoted $|g\rangle$, $|e\rangle$, $|s\rangle$, $|b\rangle$ and $|d\rangle$, respectively. The symbols \mathcal{E}_s , Ω_c , M1, M2 and Ω_d denote the signal and control fields, the mapping fields and rephasing field, respectively.

2

Theory of DRAGON

Contents

2.1 Coherences and optical Bloch equations	12
2.1.1 System Hamiltonian	12
2.1.2 Evolution of coherences	14
2.1.3 Photon propagation	16
2.1.4 Macroscopic coherences	18
2.1.5 Optical Bloch equations for ORCA	19
2.1.6 Doppler dephasing	21
2.1.7 Ground state mapping	22
2.1.8 Pulsed rephasing	23
2.1.9 Optical Bloch equations for DRAGON	24
2.2 Optical depth	26
2.3 Fluorescence noise in DRAGON	28
2.4 Reduced collective decay via Doppler dephasing	29

This section provides the theoretical framework for the DRAGON memory protocol. This includes the equations of motion of the memory, as well as other important concepts for memory operation.

Section 2.1 of this chapter will define the coherences that are used for memory operation and derive the OBEs that govern the dynamics of these coherences. As DRAGON is largely based on the telecom version of an ORCA memory, large parts of this section also apply for the description of ORCA. The derivation of the OBEs in this section is taken from existing theoretical work ([17], [22], [23]) and ongoing research of the PQI group.

As outlined in Sec. 1.4, the DRAGON protocol was developed to overcome the lifetime limitation of ORCA via a mapping to a stable ground state. After introducing the basic equations of motion in Sec. 2.1.5, we describe the ground state mapping procedure and the incorporation of the mapping into a new set of OBEs. This follows unpublished work of the PQI group.

Furthermore, we introduce the idea of pulsed rephasing, which is used to counteract the Doppler dephasing of the ensemble. An additional coherence and a field will be added to the existing equations of motion, again following unpublished work of the PQI group.

Once all the unique concepts of DRAGON are outlined, the full set of OBEs is stated in Sec. 2.1.9.

The remaining part of this chapter will examine the concepts of optical depth, fluorescence noise and collective decay. These concepts will play an important role for the experimental performance of the DRAGON protocol.

2.1 Coherences and optical Bloch equations

2.1.1 System Hamiltonian

The dynamics of the light-matter system are described by the Hamiltonian

$$H = H_A + H_L + H_{ED}, \quad (2.1)$$

where H_A describes the purely atomic part, H_L the optical part and H_{ED} the light-matter interaction.

Atomic part

Denoting the ground, intermediate and storage state as $|g\rangle$, $|e\rangle$ and $|s\rangle$, respectively, the atomic Hamiltonian reads

$$H_A = \sum_{j \in \{g, e, s\}} \hbar \omega_j \hat{\sigma}_{jj}. \quad (2.2)$$

Here $\hat{\sigma}_{jj} = |j\rangle \langle j|$ is the level population and $\hbar \omega_j$ the energy of state $|j\rangle$.

Optical part

The total optical field \mathbf{E} consists of a strong classical control field \mathbf{E}_c and a weak quantum signal field \mathbf{E}_s , such that $\mathbf{E} = \mathbf{E}_c + \mathbf{E}_s$.

The classical control field with frequency ω_c is described by

$$\mathbf{E}_c = \mathbf{v}_c \frac{\mathcal{E}_c(z, t)}{2} e^{i\omega_c(t+z/c)} + c.c.. \quad (2.3)$$

Here, \mathbf{v}_c denotes the control polarisation vector and $\mathcal{E}_c(z, t)$ the slowly-varying spatio-temporal field amplitude of the control field.

The signal field however, assumed to be on single photon level, requires a quantum description:

$$\mathbf{E}_s = i\mathbf{v}_s \int d\omega g(\omega) \hat{a}(\omega) e^{-i\omega z/c} + h.c. \quad (2.4)$$

Again, \mathbf{v}_s is the polarisation vector of the signal field. The mode amplitude $g(\omega) = \sqrt{\hbar\omega/4\pi\epsilon_0 c}$ describes the amplitude (intensity) of the particular frequency. The mode amplitude weights the photon creation $\hat{a}^\dagger(\omega)$ and annihilation $\hat{a}(\omega)$ operators for a specific frequency.

By transforming $\hat{a}(\omega, t) = \hat{a}(\omega) e^{i\omega t}$ and assuming $\sqrt{2\pi}g(\omega) \approx \sqrt{2\pi}g(\omega_s) = g_s$, with ω_s the central frequency of the signal field, we obtain

$$\mathbf{E}_s = i\mathbf{v}_s g_s \frac{\mathcal{E}_s(z, t)}{2} e^{i\omega_s(t-z/c)} + h.c., \quad (2.5)$$

with

$$\mathcal{E}_s(z, t) = \frac{e^{-i\omega_s(t-z/c)}}{\sqrt{2\pi}} \int d\omega \hat{a}(\omega, t) e^{-i\omega z/c}. \quad (2.6)$$

In this framework, control and signal field are counter-propagating (as can be seen from the different signs of the exponential containing z/c). This fact is of particular importance when investigating dephasing mechanisms in ORCA and DRAGON memories.

The Hamiltonian for the combined optical fields is then

$$H_L = \frac{\epsilon_0}{2} \int dt (\mathbf{E}_c^2 + c^2 \mathbf{B}_c^2) + \int d\omega \hbar\omega (\hat{a}^\dagger(\omega) \hat{a}(\omega) + 1/2), \quad (2.7)$$

where first term describes the energy of the classical control, with \mathbf{B}_c the magnetic component of the electro-magnetic control field, and the second term describes the quantum signal field.

Light-matter interaction

2

The light matter interaction is given in the dipole approximation. This is justified, since the relevant wavelengths for the atomic transitions (focusing on the relevant transitions in DRAGON), $\lambda_s = 780$ nm and $\lambda_c = 1529$ nm for signal and control, respectively, are much larger than the dimension of the atom (≈ 0.1 nm).

Therefore we have

$$H_{ED} = -\hat{\boldsymbol{\mu}} \cdot \mathbf{E}, \quad (2.8)$$

with transition dipole operator $\hat{\boldsymbol{\mu}} = \boldsymbol{\mu}_{ge}\sigma_{ge} + \boldsymbol{\mu}_{se}\sigma_{se} + h.c.$ and the total electric field \mathbf{E} . Here $\boldsymbol{\mu}_{ij}$ is the transition dipole strength and $\sigma_{ij} = |i\rangle\langle j|$ the transition operator for transitions between states $|i\rangle$ and $|j\rangle$. The direct transition $|s\rangle \longleftrightarrow |g\rangle$ is dipole-forbidden, hence the corresponding operators are omitted in the light-matter interaction.

2.1.2 Evolution of coherences

To describe the dynamics of atomic coherences in an atomic ensemble, the Heisenberg equation for each coherence needs to be solved. The equation reads:

$$\hbar\partial_t\sigma_{ij} = i[\sigma_{ij}, H_A + H_{ED} + H_L]. \quad (2.9)$$

The optical part of the Hamiltonian acts on the optical field but not the atomic field. Hence H_L commutes with any σ_{ij} and we neglect H_L for the evolution of coherences.

The equations for the populations read

$$\hbar\partial_t\sigma_{gg} = -i\mathbf{E} \cdot (\boldsymbol{\mu}_{ge}\sigma_{ge} - h.c.) \quad (2.10)$$

$$\hbar\partial_t\sigma_{ss} = -i\mathbf{E} \cdot (\boldsymbol{\mu}_{es}\sigma_{es} - h.c.) \quad (2.11)$$

and

$$\hbar\partial_t\sigma_{ee} = -\partial_t(\sigma_{gg} + \sigma_{ss}). \quad (2.12)$$

For the coherences we obtain

$$\hbar\partial_t\sigma_{ge} = i\hbar\omega_{eg}\sigma_{ge} - i\mathbf{E} \cdot (\boldsymbol{\mu}_{ge}^*(\sigma_{gg} - \sigma_{ee}) + \boldsymbol{\mu}_{es}\sigma_{gs}) \quad (2.13)$$

$$\hbar\partial_t\sigma_{gs} = i\hbar\omega_{sg}\sigma_{gs} - i\mathbf{E} \cdot (\boldsymbol{\mu}_{es}^*\sigma_{gs} - \boldsymbol{\mu}_{ge}^*\sigma_{es}) \quad (2.14)$$

$$\hbar\partial_t\sigma_{es} = i\hbar\omega_{se}\sigma_{es} - i\mathbf{E} \cdot (\boldsymbol{\mu}_{es}^*(\sigma_{ee} - \sigma_{ss}) - \boldsymbol{\mu}_{ge}\sigma_{gs}), \quad (2.15)$$

where $\omega_{ij} = \omega_i - \omega_j$.

Since the signal field is a weak coherent field or at single photon level, we can assume that Beer's law for absorption holds and no significant population transfer between the atomic levels takes place. We therefore have $\partial_t\sigma_{gg} = \partial_t\sigma_{ee} = \partial_t\sigma_{ss} = 0$ and we neglect the population dynamics. Note that in the initial state of the memory only the ground state $|g\rangle$ is populated, i.e., $\langle\sigma_{ee/ss}\rangle(t=0) = 0$ and $\langle\sigma_{gg}\rangle(t=0) = 1$.

We can transform into the rotating frame of the transition $|i\rangle \leftrightarrow |j\rangle$ via $\tilde{\sigma}_{ij} = \sigma_{ij}e^{-i\omega_{ij}\tau}$ with the retarded time $\tau = (t - z/c)$. This gives:

$$\hbar\partial_\tau\tilde{\sigma}_{ge} = -i\mathbf{E} \cdot (\boldsymbol{\mu}_{ge}^*e^{-i\omega_{eg}\tau} + \boldsymbol{\mu}_{es}\tilde{\sigma}_{gs}e^{-i\omega_{es}\tau}) \quad (2.16)$$

$$\hbar\partial_\tau\tilde{\sigma}_{gs} = -i\mathbf{E} \cdot (\boldsymbol{\mu}_{es}^*\tilde{\sigma}_{ge}e^{+i\omega_{es}\tau} - \boldsymbol{\mu}_{ge}^*\tilde{\sigma}_{es}e^{-i\omega_{eg}\tau}) \quad (2.17)$$

$$\hbar\partial_\tau\tilde{\sigma}_{es} = +i\mathbf{E} \cdot (\boldsymbol{\mu}_{ge}\tilde{\sigma}_{gs}e^{+i\omega_{eg}\tau}). \quad (2.18)$$

In the presence of an interacting optical field, the rotating wave approximation (RWA) will simplify the above equations of motion. We see this by expanding the total optical field \mathbf{E} . The signal field with frequency ω_s couples only (off-resonantly) to the transition $|g\rangle \leftrightarrow |e\rangle$ and the control field with ω_c couples only to $|e\rangle \leftrightarrow |s\rangle$. The detuning for both fields is given by $\Delta_s = \omega_s - \omega_{eg}$ for the signal and $\Delta_c = \omega_c - \omega_{es}$ for the control field. The coupling of the light field \mathbf{E} to the atomic coherences leads to terms that evolve with either $\Delta_{s/c}$ or the sums $\omega_{s/c} + \omega_{ge/es}$. In the RWA we can neglect the terms evolving with the sum. This holds since in our framework we have that $|\Delta_{s/c}| \approx 6 \text{ GHz} \ll \omega_{s/c} + \omega_{ge/es}$. Hence the terms evolving with the sum of frequencies average out on the time scale given by the oscillations of terms evolving with $\Delta_{s/c}$.

With these approximations in place, we obtain a simplified set of equations:

$$\hbar\partial_\tau\tilde{\sigma}_{ge} = -i\boldsymbol{\mu}_{ge}^* \left(i\mathbf{v}_s g_s \frac{\mathcal{E}_s}{2} e^{+i\Delta_s\tau} \right) - i\boldsymbol{\mu}_{es} \tilde{\sigma}_{gs} \left(\mathbf{v}_c \frac{\mathcal{E}_c}{2} e^{+i\Delta_c\tau} e^{2ik_c z} \right) \quad (2.19)$$

$$\hbar\partial_\tau\tilde{\sigma}_{gs} = -i\boldsymbol{\mu}_{es}^* \tilde{\sigma}_{ge} \left(\mathbf{v}_c^* \frac{\mathcal{E}_c^*}{2} e^{-i\Delta_c\tau} e^{-2ik_c z} \right) + i\boldsymbol{\mu}_{ge}^* \tilde{\sigma}_{es} \left(i\mathbf{v}_s g_s \frac{\mathcal{E}_s}{2} e^{+i\Delta_s\tau} \right) \quad (2.20)$$

$$\hbar\partial_\tau\tilde{\sigma}_{es} = +i\boldsymbol{\mu}_{ge} \tilde{\sigma}_{gs} \left(-i\mathbf{v}_s^* g_s \frac{\mathcal{E}_s^\dagger}{2} e^{-i\Delta_s\tau} \right). \quad (2.21)$$

This set of equations contains terms that will be small since weakly excited operators are involved. Here we follow [17] and perturbatively eliminate those terms that contain both a coherence and an excitation of the weak signal field \mathcal{E}_s . This approximation leaves us with only two equations:

$$\hbar\partial_\tau\tilde{\sigma}_{ge} = \frac{\boldsymbol{\mu}_{ge}^* \cdot \mathbf{v}_s g_s \mathcal{E}_s}{2} e^{+i\Delta_s\tau} - \frac{i\boldsymbol{\mu}_{es} \cdot \mathbf{v}_c \mathcal{E}_c \tilde{\sigma}_{gs}}{2} e^{+i\Delta_c\tau} e^{2ik_c z} \quad (2.22)$$

$$\hbar\partial_\tau\tilde{\sigma}_{gs} = -\frac{i\boldsymbol{\mu}_{es}^* \cdot \mathbf{v}_c^* \mathcal{E}_c^* \tilde{\sigma}_{ge}}{2} e^{-i\Delta_c\tau} e^{-2ik_c z}. \quad (2.23)$$

Note that this set of equations does not contain the coherence $\tilde{\sigma}_{es}$ anymore. This follows from the above perturbative argument.

In this framework, the coherence $\tilde{\sigma}_{ge}$ describes the atomic polarisation and $\tilde{\sigma}_{gs}$ the atomic spin wave.

2.1.3 Photon propagation

The above derivation of atomic coherences describes how the atomic ensemble is affected by the counter-propagating signal and control light fields. The control field is a classical light field of high intensity. We assume that the propagation of the control field through the atomic ensemble leaves this field unchanged. However, the signal field is a weak quantum field and a careful analysis as to how the atomic field affects this optical field is in order.

The effects of the atomic ensemble on the signal field \mathbf{E}_s can best be understood if we model the ensemble as a dielectric medium through which the signal field passes.

Maxwell's equation in this scenario read:

$$\begin{aligned} \nabla \cdot \mathbf{D}_s &= 0, & \nabla \cdot \mathbf{B} &= 0, \\ \nabla \times \mathbf{E}_s &= -\partial_t \mathbf{B}, & \nabla \times \mathbf{H} &= \partial_t \mathbf{D}_s. \end{aligned}$$

In these equations we have the signal electric displacement field \mathbf{D}_s , the magnetic field \mathbf{H} , the signal electro-magnetic field \mathbf{E}_s and the magnetic induction \mathbf{B} . However, since the atomic ensemble

carries no magnetisation, we have that $\mathbf{B} = \mu_0 \mathbf{H}$, with the permeability of free space μ_0 .

Within the Coulomb gauge and by rearranging Maxwell's equations, we find for the electro-magnetic field of the signal

$$\nabla^2 \mathbf{E}_s = \mu_0 \partial_t^2 \mathbf{D}_s, \quad (2.24)$$

where the displacement field is formed by the electro-magnetic field and the material polarisation density \mathbf{P} , i.e.,

$$\mathbf{D}_s = \epsilon_0 \mathbf{E}_s + \mathbf{P}. \quad (2.25)$$

The polarisation density is defined as the dipole moment per unit volume. As only the signal field is influenced by the medium polarisation, we can focus on the polarisation \mathbf{P}_s that arises from dipoles oscillating at the signal frequency ω_s and therefore affect the signal field.

Reordering and using $\epsilon_0 \mu_0 = 1/c^2$ we obtain

$$\left[\nabla^2 - \frac{1}{c^2} \partial_t^2 \right] \mathbf{E}_s = \mu_0 \partial_t^2 \mathbf{P}_s. \quad (2.26)$$

The temporal profile of \mathbf{P}_s is determined by a slowly varying envelope $\tilde{\mathbf{P}}_s$ and a fast oscillation of the carrier wave:

$$\mathbf{P}_s = \tilde{\mathbf{P}}_s e^{i\omega_s \tau}. \quad (2.27)$$

By substituting the expression for both electro-magnetic field and polarisation into Eq. (2.26), we obtain

$$\left[\nabla^2 - \frac{1}{c^2} \partial_t^2 \right] (i\mathbf{v}_s g_s \frac{\mathcal{E}_s}{2} e^{i\omega_s \tau}) = \mu_0 \partial_t^2 \tilde{\mathbf{P}}_s e^{i\omega_s \tau}. \quad (2.28)$$

In order to simplify this expression, two approximations need to be applied.

1. **Paraxial approximation:** the beam divergence θ of a Gaussian beam is given by $\theta = \frac{\lambda_s}{\pi w_0}$, with w_0 the beam waist. The divergence of the signal field can be neglected if $\lambda_s \ll w_0$. This holds for our setup since $w_0 \approx 200 \mu\text{m}$ and $\lambda_s \leq 1529 \text{ nm}$.
2. **Slowly varying envelope approximation (SVE):** we can neglect the effect of changes in polarisation that occur on the timescales of the fast oscillating carrier frequency ω_s . This is valid if the temporal duration of the signal field is much longer than the oscillation period of the carrier wave $\frac{2\pi}{\omega_s} \approx 2.6 \times 10^{-15} \text{ s}$. This also holds since the signal pulse duration is about 300 ps.

The paraxial approximation allows us to simplify the Nabla operator, such that $\nabla^2 \approx \partial_z^2$, i.e., for an optical field propagating in z-direction we neglect propagation in x- and y-direction.

If the envelope of both the electric field and the polarisation vary slowly in time (as in the SVE approximation), we can assume that the second order derivatives of field and polarisation are much smaller than the first order derivatives. Hence we drop the second order derivatives $\partial_t^2 \mathcal{E}_s / \partial_z^2 \mathcal{E}_s$ and similar for $\tilde{\mathbf{P}}_s$ in Eq. (2.28) altogether.

By taking the inner product with the polarisation vector \mathbf{v}_s^* , we arrive at the expression

$$\left[\partial_z + \frac{1}{c} \partial_t \right] \mathcal{E}_s = -\frac{\mu_0 \omega_s^2}{g_s k_s} \mathbf{v}_s^* \cdot \tilde{\mathbf{P}}_s. \quad (2.29)$$

2.1.4 Macroscopic coherences

Now that the propagation of the signal field \mathcal{E}_s is expressed in an equation of motion, we also need to find an equation of motion for the two excitations of the atomic ensemble, the macroscopic spin wave and the macroscopic polarisation. These are referred to as macroscopic, since their description involves the entirety of the ensemble. This is not to be confused with the atomic coherence that was discussed before: an atomic coherence can be thought of as a superposition of two states, while the macroscopic coherence is a superposition of atomic excitations, a Werner state of single photon excitations to be precise.

We call the coherence between ground and excited state a spin wave, following literature [23].

For the analysis of the macroscopic coherences (see [22]), we slice the atomic ensemble (usually confined in a glass cylinder) into cylindrical volume elements δV , where the longitudinal extent δL (in propagation direction) is much smaller than the signal wavelength, i.e., we require $\delta L \ll \lambda_s$. This allows us to assume a constant phase within each volume element.

Denote n_V the number density of a volume element. Furthermore we assume that the transverse extent δA of the volume element satisfies $\delta A \gg \lambda_s^2$, such that we can ignore dipole-dipole interactions. This is a reasonable assumption since the atomic ensemble is a dilute gas.

For a cylindrical element δV at position z along the propagation axis, we define the macroscopic polarisation \mathbf{P}_s and spin wave \mathbf{S} as

$$\mathbf{P}_s = \frac{1}{\delta V} \sum_{a(z)} \boldsymbol{\mu}_{ge} \sigma_{ge}^a + h.c. \quad (2.30)$$

$$\mathbf{S} = \frac{1}{\delta V} \sum_{a(z)} \boldsymbol{\mu}_{gs} \sigma_{gs}^a + h.c., \quad (2.31)$$

where $a(z)$ is the index over the atoms within the element δV and σ_{ij}^a the corresponding atomic coherence for transition $|i\rangle \leftrightarrow |j\rangle$.

We can rewrite both equations to obtain an expression for the operators of both polarisation P_{ge} and spin wave S_{gs} :

$$P_{ge} = \frac{1}{\sqrt{n_V \delta V}} \sum_{a(z)} \tilde{\sigma}_{ge}^a e^{-i\Delta_s \tau} \quad (2.32)$$

$$S_{gs} = \frac{1}{\sqrt{n_V \delta V}} \sum_{a(z)} \tilde{\sigma}_{gs}^a e^{-i(\Delta_s + \Delta_c)\tau} e^{2ik_c z}. \quad (2.33)$$

Here we have identified P_{eg} , such that $\tilde{P}_s = \sqrt{n_V} \mu_{ge} P_{ge}$ and similar for S_{gs} .

The form of Eqs. 2.32 and 2.33 is chosen such that the operators satisfy the bosonic commutation relation

$$[P_{ge}(z, t), P_{ge}^\dagger(z', t)] = \delta(z - z'), \quad (2.34)$$

and similarly for S_{gs} . This is an instance of the Holstein-Primakoff transformation, where single particle (spin) excitations are mapped to bosonic excitations of a larger number of spin carrying particles in the ensemble [24].

2.1.5 Optical Bloch equations for ORCA

We determined the photon propagation and the macroscopic coherences of the system, such that we can now expand the result into a set of coupled differential equations that describe the basic version of an ORCA memory. The equations read

$$\left[\partial_z + \frac{1}{c} \partial_t \right] \mathcal{E}_s = -\frac{\kappa_{ge}^*}{2} P_{ge} \quad (2.35)$$

$$\partial_\tau P_{ge} = -(\gamma_e + i\Delta_s) P_{ge} + \frac{\kappa_{ge}}{2} \mathcal{E}_s - \frac{i}{2} \Omega_c S_{gs} \quad (2.36)$$

$$\partial_\tau S_{gs} = -(\gamma_s + i(\Delta_s + \Delta_c)) S_{gs} - \frac{i}{2} \Omega_c^* P_{ge}, \quad (2.37)$$

where

$$\kappa_{ge} = \frac{\mu_{ge}^* v_s}{\hbar} \sqrt{\frac{\hbar \omega_s n_v}{2 \epsilon_0 c}} \quad (2.38)$$

$$\Omega_c = \frac{\mu_{es} v_c \mathcal{E}_c}{\hbar}. \quad (2.39)$$

We call Ω_c the Rabi frequency of the control field. Note that in the equations of motion we have included decoherence via spontaneous emission of states $|e\rangle$ and $|s\rangle$, denoted γ_e and γ_s , respectively. This set of equations can be simplified by rotating into the frame co-propagating with the photon field. This allows us to write the evolution of signal and control as a function of τ . We then modify the derivative:

$$\partial_{z|t} + \frac{1}{c}\partial_{t|z} \rightarrow \partial_{z|\tau}. \quad (2.40)$$

We also normalise the time τ by γ_e and the length z by the cell length L . This results in a rescaling (following [22]):

$$\tau\gamma_e \rightarrow \tau, \quad \frac{z}{L} \rightarrow z \quad (2.41)$$

$$\frac{\partial}{\partial \tau} \rightarrow \partial_\tau, \quad \partial_z L \rightarrow \partial_z \quad (2.42)$$

$$\frac{\Delta_j^e}{\gamma_e} \rightarrow \Delta_j, \quad \frac{\Omega_c}{\gamma_e} \rightarrow \Omega_c \quad (2.43)$$

$$\frac{|\kappa_{ge}|^2 L}{\gamma_e} \rightarrow d, \quad \frac{\mathcal{E}_s}{\sqrt{\gamma_e L}} \rightarrow \mathcal{E}_s. \quad (2.44)$$

This leaves us with a simpler version of the equations of motion for the ORCA memory, the OBEs:

$$\partial_z \mathcal{E}_s = -\sqrt{\frac{d}{2}} P_{ge} \quad (2.45)$$

$$\partial_\tau P_{ge} = -(\gamma_e + i\Delta_s) P_{ge} + \sqrt{\frac{d}{2}} \mathcal{E}_s - \frac{i}{2} \Omega_c(\tau, z) S_{gs} \quad (2.46)$$

$$\partial_\tau S_{gs} = -(\gamma_s + i(\Delta_s + \Delta_c)) S_{gs} - \frac{i}{2} \Omega_c^*(\tau, z) P_{ge} \quad (2.47)$$

Note that in these equations the Rabi frequency Ω_c has an explicit time dependence. This is important since the Rabi frequency is dependent on the spatio-temporal profile of the control field.

Another crucial simplification of the OBEs arises from the detuning in the two-photon transition described by the signal and control field. Both these fields are detuned by Δ_s and Δ_c from their respective transitions. That means that the intermediate transition $|g\rangle \rightarrow |e\rangle$ is only weakly excited by the signal field. More specifically we have that $|\Delta_{s/c}| \gg \Gamma_e$, where Γ_e is the linewidth of the intermediate state.

With this approximation the coherence P_{ge} is never really established and we assume $\partial_\tau P_{ge} \approx 0$.

Applying the above arguments to our set of OBEs we obtain

$$\partial_z \mathcal{E}_s = \frac{i\sqrt{\frac{d}{2}}\Omega_c S_{gs} - d\mathcal{E}_s}{2(\gamma_e + i\Delta_s)} \quad (2.48)$$

$$\partial_\tau S_{gs} = - \left[\gamma_s + i(\Delta_s + \Delta_c) + \frac{|\Omega_c|^2}{4(\gamma_e + i\Delta_s)} \right] S_{gs} - \frac{i\Omega_c^* \sqrt{d}\mathcal{E}_s}{\sqrt{8}(\gamma_e + i\Delta_s)}. \quad (2.49)$$

In this form the equations express important dynamics of the ORCA memory. The term with $|\Omega_c|^2$ for the spin wave S_{gs} represents a phase that is due to the ac-Stark shift of the control field. For the equation of the signal field \mathcal{E}_s , the imaginary and real part of the term $(d\mathcal{E}_s)/(2(\gamma_e + i\Delta_s))$ express the dispersion and absorption, respectively. A diagram for these equations, including the detunings and energy levels, is given in Fig. 2.4.

2.1.6 Doppler dephasing

ORCA and DRAGON use a warm atomic ensemble for the storage of optical fields. The velocity of each atom v in the ensemble is sampled from a Maxwell-Boltzmann distribution

$$f(v) = \sqrt{\frac{m}{2\pi k_B T}} e^{-\frac{mv^2}{2k_B T}}, \quad (2.50)$$

where m is the mass of the atom species and T the ensemble temperature.

Each atom can therefore be associated with a velocity class, with each velocity class v experiencing a Doppler shift from the detuning of the optical fields $\Delta_s^{(v)} = \Delta_s - k_s v$ and $\Delta_c^{(v)} = \Delta_c + k_c v$ (with a different sign since control and signal are counter-propagating). The number density of an infinitesimal velocity class $v + dv$ is $n_V^{(v)} \approx f(v)n_V$. Substituting this into the expression of d in Eq. 2.44 yields $d^{(v)}$. We call $d^{(v)}$ the OD for velocity class v (see Sec. 2.2 for detailed definition). Summing over all velocities gives a full set of equations:

$$\partial_z \mathcal{E}_s^{(\tau,z)} = \sum_v \left(\frac{+i\sqrt{\frac{d^{(v)}}{2}}\Omega_c S_{gs}^{(\tau,z,v)} - d^{(v)}\mathcal{E}_s^{(\tau,z)}}{2(\gamma_e + i\Delta_s^{(v)})} \right) \quad (2.51)$$

$$\partial_\tau S_{gs}^{(\tau,z)} = - \sum_v \left(\gamma_s + i(\Delta_s^{(v)} + \Delta_c^{(v)}) + \frac{|\Omega_c|^2}{4(\gamma_e + i\Delta_s^{(v)})} \right) S_{gs}^{(\tau,z,v)} - \sum_v \frac{i\sqrt{d^{(v)}}\Omega_c^* \mathcal{E}_s^{(\tau,z)}}{\sqrt{8}(\gamma_e + i\Delta_s^{(v)})}. \quad (2.52)$$

When the RI sequence is concluded, the control field is inactive and we have $\Omega_c = 0$. Assuming two-photon resonance, i.e., $\Delta_s = -\Delta_c$, we have $\Delta_s^{(v)} + \Delta_c^{(v)} = -(k_s - k_c)v = -\delta k v$. Here we introduced the mode mismatch $\delta k = k_s - k_c$.

The coherence right after the two-photon transition for read in is $S_{gs}^{(0,z)}$. Note that the initial state

is independent of the velocity as the spin wave has not evolved yet. The spin wave for velocity v then evolves as

$$\partial_\tau S_{gs}^{(\tau,z,v)} = - \left(\gamma_s + i(\Delta_s^{(v)} + \Delta_c^{(v)}) \right) S_{gs}^{(0,z)}, \quad (2.53)$$

which is solved by

$$S_{gs}^{(\tau,z,v)} = S_{gs}^{(0,z)} e^{-\gamma_s \tau} e^{i\delta k v \tau}. \quad (2.54)$$

This however only gives the solution for one velocity class. In order to obtain the solution for the ensemble, we need to weight every velocity class with the Maxwell-Boltzmann distribution, which yields

$$S_{gs}^{(\tau,z)} = e^{-\frac{\gamma_s}{2} \tau} e^{-\frac{(\delta k \tau)^2 k_B T}{2m}} S_{gs}^{(0,z)}. \quad (2.55)$$

From this expression we can derive a useful metric: the characteristic time scale of Doppler dephasing

$$\tau_D = \sqrt{\frac{m}{(\delta k)^2 k_B T}}. \quad (2.56)$$

This gives the times scale for the Gaussian decay of the observed coherence $|S_{gs}^{(\tau,z)}|^2$. The time τ_D limits the storage time for large mode mismatch significantly since the coherence is decreased over time. For the telecom ORCA the Doppler-limited storage time is estimated with $\tau_D \approx 1.1$ ns [21].

2.1.7 Ground state mapping

The ground state mapping is one of the two fundamentally new details in DRAGON (the other being the pulsed rephasing in Sec. 2.1.8). The idea is to use two additional optical fields $M1$ and $M2$, which map the coherence to a stable ground state and thereby create a new coherence S_{gb} between the two hyperfine ground states.

In order to use ground state mapping as a mechanism to increase the lifetime, we need to make sure that the mapping procedure itself is not introducing any decoherence channel. The mapping fields will be classical light fields of moderate intensity, with the $M1$ and $M2$ pulse separated by a certain time τ_{sep} . The light fields are chosen to be on resonance with the atomic transitions, such that less optical power is required for the mapping. This resonantly populates the intermediate level (no adiabatic elimination of the intermediate state). First simulations show that the highest mapping efficiency is achieved for a pulse separation of about $\tau_{sep} \approx 400 - 500$ ps.

At these separations we can lose coherence via collective decay. We denote the emission of light via collective decay as \mathcal{E}_R . A schematic of the atomic structure with the leakage channel is shown in Fig. 2.1. This decoherence mechanism is mitigated if the atomic ensemble is dephased via

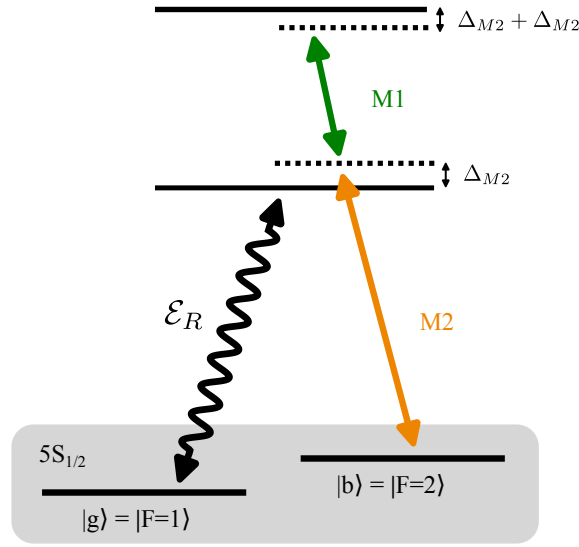


Figure 2.1: Unwanted read out \mathcal{E}_R of the coherence during the ground state mapping.

Doppler dephasing, i.e., the collective decay is reduced due to Doppler dephasing (see Sec. 2.4). The characteristic time scale of dephasing is $\tau_D = \sqrt{\frac{m}{(\delta k)^2 k_B T}}$ (derived below in Sec. 2.4), just as the time scale for Doppler dephasing in Sec. 2.1.6. Therefore, by mapping down a dephased ensemble, we reduce the leakage \mathcal{E}_R and use Doppler dephasing to our advantage.

Experimentally, the ground state mapping will not have perfect mapping efficiency, i.e., a part of the coherence is not mapped down and effectively lost.

2.1.8 Pulsed rephasing

As outlined in the introduction, DRAGON also introduces a novel scheme to rephase the atomic ensemble. Such a rephasing is required since the mode mismatch δk in DRAGON is large and the effect on the coherence correspondingly strong. With the signal wavelength at $\lambda_s = 780$ nm and the control field at $\lambda_c = 1529$ nm, we have $\delta k > 0$.

The idea of pulsed rephasing is to invert the direction of phase accumulation due to Doppler dephasing and thereby to rephase the ensemble.

After GSM, the coherence is mapped back to the initial spin wave S_{gs} . By sending a π -pulse resonant with the $|s\rangle \rightarrow |d\rangle$ transition, the ensemble coherence is changed to S_{gd} and the mode mismatch is $\delta k' = k_s - k_c - k_d$. Here we implicitly assume that the π -pulse is co-propagating with the control field.

The state $|d\rangle$ should be chosen in way to give $\delta k' < 0$, which is necessary to invert a previous phase accumulation with $\delta k > 0$. A suitable, optically accessible state for DRAGON in ^{87}Rb is therefore $|d\rangle = |8F_{7/2}\rangle$ with $\lambda_c = 793$ nm.

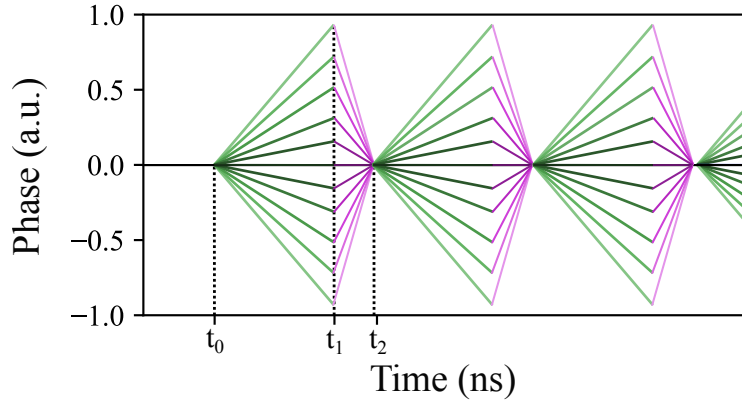


Figure 2.2: Schematic of phase accumulation in pulsed rephasing. The green lines represent the phase evolution of the coherence S_{gs} for different velocity classes, the violet lines the phase evolution of S_{gd} for the same velocity classes.

After the coherence is mapped up again at a time t_0 , the coherence S_{gs} accumulates phase at a rate $\delta k > 0$. At time t_1 we apply the π -pulse to state $|d\rangle$, such that now the coherence S_{gd} accumulates phase with a rate $\delta k' < 0$. Depending on the ratio $s := |\delta k' / \delta k|$, the coherence S_{gd} is mapped back to S_{gs} with another resonant π -pulse at time t_2 . After that, the memory can be read out.

The effect of the rephasing is determined by the ratio s , the previous phase accumulation and the time spent in state $|d\rangle$. The optimal rephasing time $t_d := t_2 - t_1$ is proportional to t_{store}/s , where t_{store} is the total evolution time between read in process and time t_0 .

An idealised schematic of the phase evolution with pulsed rephasing can be seen in Fig. 2.2.

The technique of pulsed rephasing can in theory reverse previous phase accumulation. However, for optimal reversal of Doppler dephasing a certain time t_d is required. With this requirement on time the memory is no longer on-demand.

With pulsed rephasing, the last novel element of DRAGON has been introduced. The full operational sequence is depicted in Fig. 2.3

2.1.9 Optical Bloch equations for DRAGON

We can describe the DRAGON protocol with the same type of OBEs as derived for ORCA. The difference arises from additional fields and sublevels that need to be considered.

Without the additional fields, the equations with Doppler dephasing from ORCA read (see Eq.

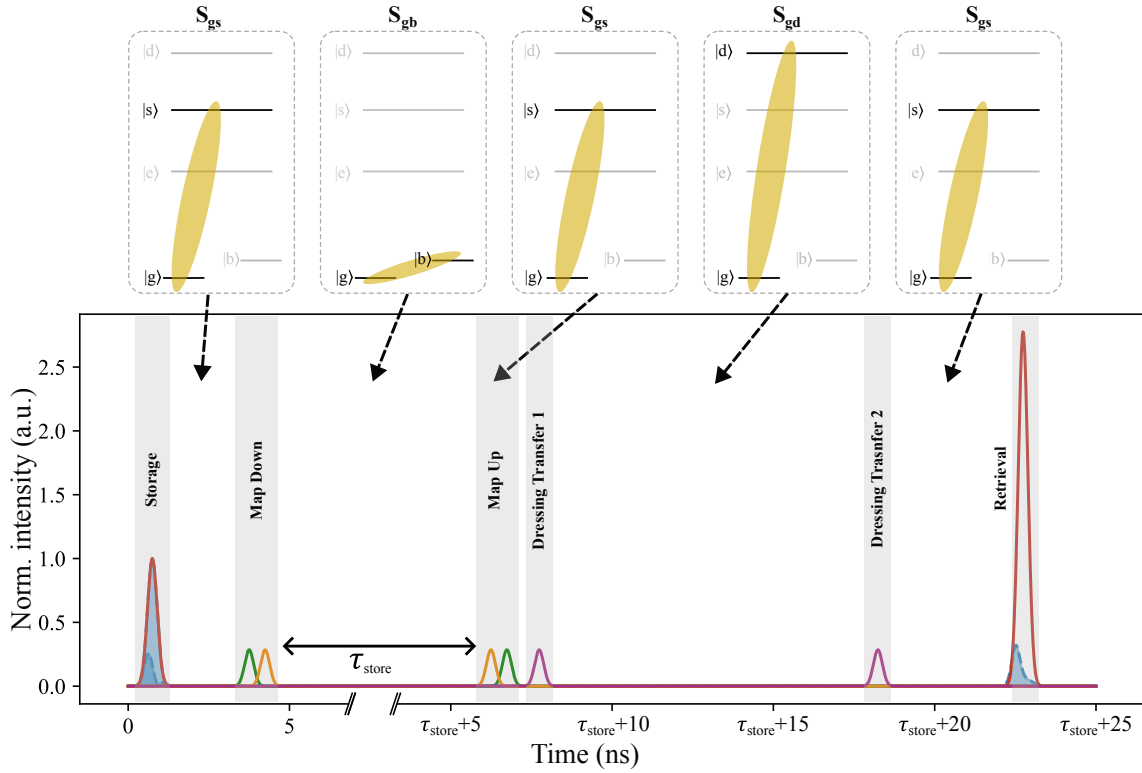


Figure 2.3: Schematic of pulse sequence in DRAGON with GSM and pulsed rephasing. The upper level diagrams indicate the established coherence in each step. The pulse sequence in the lower part shows the corresponding application of pulses.

2.51 and 2.52)

$$\partial_z \mathcal{E}_s^{(\tau,z)} = \sum_v \left(\frac{+i\sqrt{\frac{d^{(v)}}{2}} \Omega_c S_{gs}^{(\tau,z,v)} - d^{(v)} \mathcal{E}_s^{(\tau,z)}}{2(\gamma_e + i\Delta_s^{(v)})} \right) \quad (2.57)$$

$$\partial_\tau S_{gs}^{(\tau,z)} = - \sum_v \left(\gamma_s + i(\Delta_s^{(v)} + \Delta_c^{(v)}) + \frac{|\Omega_c|^2}{4(\gamma_e + i\Delta_s^{(v)})} \right) S_{gs}^{(\tau,z,v)} - \frac{i\sqrt{d^{(v)}} \Omega_c^* \mathcal{E}_s^{(\tau,z)}}{\sqrt{8}(\gamma_e + i\Delta_s^{(v)})}. \quad (2.58)$$

One additional aspect of DRAGON in comparison to ORCA is the ground state mapping, that is introduced in Section 2.1.7. As outlined, this procedure introduces the two additional light fields $M1$ and $M2$ at resonant frequencies $\nu_{M1} = 196.0240$ THz and $\nu_{M2} = 384.2277$ THz (in ^{87}Rb). By choosing the value ν_{M2} , we choose the ground state sublevel $F = 2$ to be the ground mapping state. However, in principle also the state $F = 1$ could have been chosen.

The other novelty in DRAGON is the pulse rephasing, which introduces the new coherence S_{gd} with the rephasing state $|d\rangle$ and the Rabi frequency of the rephasing field Ω_d . The rephasing field is resonant with the transition $|4D_{5/2}\rangle \rightarrow |8F_{7/2}\rangle$, so we have $\nu_d = 378.1705$ THz. The rephasing state $|8F_{7/2}\rangle$ has a decay rate γ_d .

Considering the two additional coherences S_{gb} and S_{gd} , plus the fields $M1$, $M2$ and Ω_d , the adjusted

OBEs for the full DRAGON protocol read:

$$\partial_z \mathcal{E}_s^{(\tau,z,v)} = \frac{+i\sqrt{\frac{d^{(v)}}{2}} \Omega_c S_{gs}^{(\tau,z,v)} - d^{(v)} \mathcal{E}_s^{(\tau,z,v)}}{2(\gamma_e + i\Delta_s^{(v)})} \quad (2.59)$$

$$\partial_z \mathcal{E}_R^{(\tau,z,v)} = \sqrt{d^{(v)}} P_{ge}^{(\tau,z,v)} \quad (2.60)$$

$$\partial_\tau S_{gs}^{(\tau,z,v)} = - \left(\gamma_s + i\Delta_{\text{II}}^{(v)} + \frac{|\Omega_c|^2}{4(\gamma_e + i\Delta_s^{(v)})} \right) S_{gs}^{(\tau,z,v)} - \frac{i\sqrt{d^{(v)}} \Omega_c^* \mathcal{E}_s^{(\tau,z,v)}}{\sqrt{8}(\gamma_e + i\Delta_s^{(v)})} - iM_1^* P_{ge}^{(\tau,z,v)} - i\Omega_d^{(\tau,z)} S_{gd}^{(\tau,z,v)} \quad (2.61)$$

$$\partial_\tau P_{ge}^{(\tau,z,v)} = - \left(\gamma_e + i\Delta_{\text{III}}^{(v)} \right) P_{ge}^{(\tau,z,v)} - \sqrt{d^{(v)}} \mathcal{E}_R^{(\tau,z,v)} - iM_1 S_{gs}^{(\tau,z,v)} - iM_2 S_{gb}^{(\tau,z,v)} \quad (2.62)$$

$$\partial_\tau S_{gb}^{(\tau,z,v)} = - \left(\gamma_d + i\Delta_{\text{IV}}^{(v)} \right) S_{gb}^{(\tau,z,v)} - iM_2^* P_{ge}^{(\tau,z,v)} \quad (2.63)$$

$$\partial_\tau S_{gd}^{(\tau,z,v)} = - \left(\gamma_d + i\Delta_{\text{D}}^{(v)} \right) S_{gd}^{(\tau,z,v)} - i \left(\Omega_d^{(\tau,z)} \right)^* S_{gs}^{(\tau,z,v)}, \quad (2.64)$$

where we have defined

- $\Delta_{\text{II}}^{(v)} = \Delta_s^{(v)} + \Delta_c^{(v)}$,
- $\Delta_{\text{III}}^{(v)} = \Delta_s^{(v)} + \Delta_c^{(v)} - \Delta_{M1}^{(v)}$,
- $\Delta_{\text{IV}}^{(v)} = \Delta_s^{(v)} + \Delta_c^{(v)} - \Delta_{M1}^{(v)} - \Delta_{M2}^{(v)}$,
- $\Delta_{\text{D}}^{(v)} = \Delta_s^{(v)} + \Delta_c^{(v)} + \Delta_d^{(v)}$,

with $\Delta_{M1}^{(v)} = \omega_{M1} - \omega_{se} - k_{M1}v$, $\Delta_{M2}^{(v)} = \omega_{M2} - \omega_{eb} - k_{M2}v$ and $\Delta_{\text{D}}^{(v)} = \omega_d - \omega_{ds} - k_d v$.

2.2 Optical depth

In the derivation of the equations of motion of the ORCA memory (Eq. 2.44) we have introduced the dimensionless quantity d , the optical depth (OD) of the atomic ensemble. It is defined as

$$d = \frac{|\mu_{ge}|^2 \omega_s n_V L}{2\gamma_e \hbar \epsilon_0 c}, \quad (2.65)$$

where we used that for the polarisation vector we have $\mathbf{v}_s^2 = 1$. The optical depth d quantifies the strength of the light-matter interaction in an ensemble-based optical quantum memory.

For a transition with transition frequency ω_0 and natural linewidth Γ_N of the final state, the optical

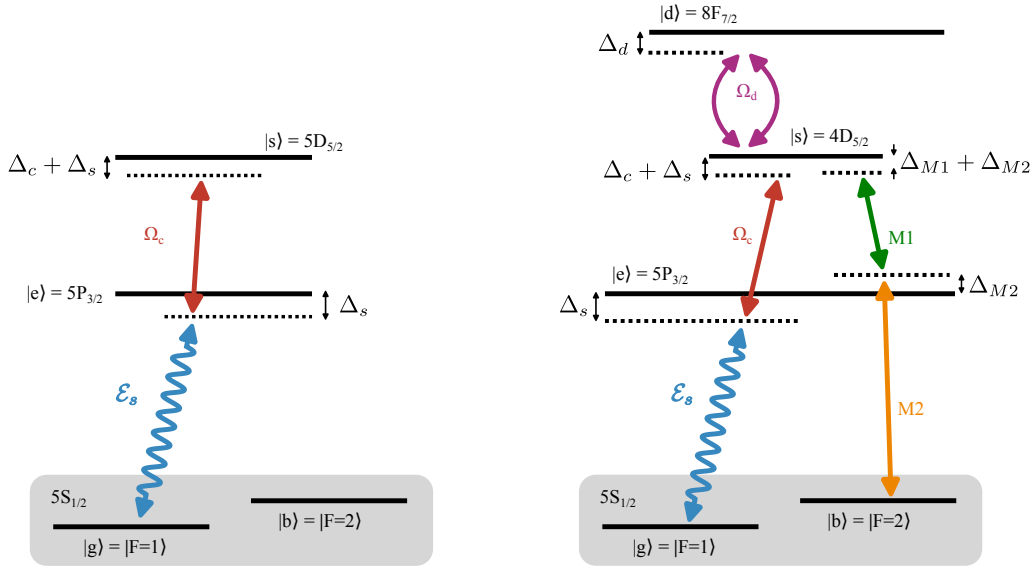


Figure 2.4: Left: ORCA level diagram. The signal \mathcal{E}_s is at $\lambda_s = 780$ nm, the control Ω_c at $\lambda_c = 776$ nm. The detuning from resonance is denoted Δ_s and Δ_c . Right: DRAGON level diagram with rephasing state $|d\rangle$. This level diagram is similar to the ORCA diagram, but it uses $\lambda_c = 1529$ nm. Additionally, the mapping fields M1, M2 and Ω_d are introduced with their respective detunings Δ_{M1} , Δ_{M2} and Δ_d .

depth influences the natural absorption coefficient α_N . We have:

$$\alpha_N = 2d \left(\frac{(\Gamma_N/2)^2}{(\omega - \omega_0)^2 + (\Gamma_N/2)^2} \right). \quad (2.66)$$

The resonance for $\omega = \omega_0$ has Lorentzian shape and the absorption scales linearly with the optical depth. Therefore, in ORCA/DRAGON protocols, the RI/RO processes are also affected linearly by the optical depth.

However, in warm atomic vapors, a Lorentzian profile cannot be directly observed, since the atoms experience individual Doppler shifts in frequency. This leads to a Doppler broadening, which follows a Gaussian shape. The convolution of Lorentzian and Gaussian yields the correct absorption profile and is referred to as Voigt profile (see also Sec. 3.4).

The Doppler-broadened absorption α_D is then given as [25]

$$\alpha_D = 2\tilde{d} \exp \left[-\frac{1}{2} \left(\frac{\omega - \omega_0}{\sigma_D} \right)^2 \right], \quad (2.67)$$

where $\sigma_D = \omega_0 \sqrt{k_B T / mc^2}$ is the width of the Doppler broadening and \tilde{d} is the effective optical depth with

$$\frac{\tilde{d}}{d} = \sqrt{\pi \ln(2)} \left(\frac{\Gamma_N}{\Gamma_D} \right). \quad (2.68)$$

The FWHM of the Doppler profile is $\Gamma_D = 2\sqrt{2\ln 2}\sigma_D$.

The cylindrical cell in the experimental setup contains a dilute Rubidium vapour, such that we can assume the gas to behave like an ideal gas.

The total number density is given by

$$n_V(T) = \frac{133.323}{k_B T} \times 10^{P_L(T)}, \quad (2.69)$$

where $P_L(T)$ the temperature-dependent pressure for liquid Rubidium. We use the formula for liquid Rubidium since the operation temperature of the memory is above the melting point of Rubidium of 39.3 °C.

We have [26]

$$P_L(T) = 15.88253 - \frac{4529.535}{T} + 0.00058663 \times T - 2.99138 \ln(T) \quad (2.70)$$

This shows an exponential increase of the number density of the Rubidium vapour in the liquid phase (see [26]) with temperature, and similarly the optical depth scales exponentially with temperature. This behaviour motivates the warm operating temperatures of the memory.

2.3 Fluorescence noise in DRAGON

DRAGON is essentially a connection between a ladder and a Λ -structure memory. Since DRAGON has certain features of a Λ -structure memory it is also susceptible to fluorescence noise (FN). When mapping down, the $M2$ field (resonant with the transition $|5S_{1/2}, F=2\rangle \rightarrow |5P_{3/2}\rangle$) can couple unintentionally to the $F=1$ ground state. This is denoted by Ω in Fig. 2.5, which is approx. 6 GHz detuned from the transition $|5S_{1/2}, F=1\rangle \rightarrow |5P_{3/2}\rangle$. This can emit a Stokes photon α , which populates the $F=2$ state. When mapping up again, the $M2$ can pick up this Stokes excitation and populate the $5P_{3/2}$ state resonantly (denoted with Ω'). From there we can have a decay α' into the state $F=1$.

In DRAGON the FN can be filtered out: the photon α' would be 6 GHz detuned from the signal photon. Using a frequency filter we can filter out this unwanted signal. As the noise photon α' emerges right after the map up pulse $M2$, we could also temporally filter out the signal.

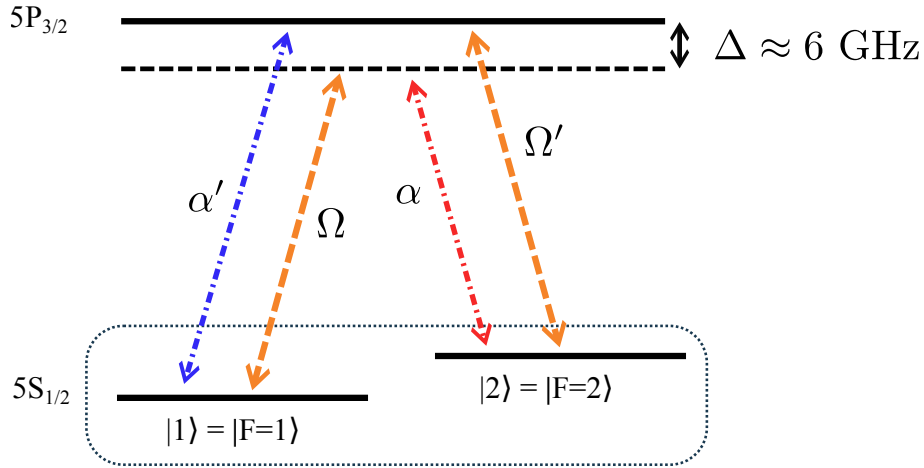


Figure 2.5: Schematic of fluorescence noise in DRAGON for initial state $F = 1$ and mapping state $F = 2$

2.4 Reduced collective decay via Doppler dephasing

As outlined in Section 2.1.9, a channel of decoherence is introduced in the the GSM procedure by resonantly populating the intermediate state $|5P_{3/2}\rangle$, which results in a leakage field \mathcal{E}_R . To avoid this leakage, we can use the Doppler dephasing to our advantage.

Although we can understand the protection of the coherence by consulting Eq. 2.55, the effect of dephasing on the coherence can also be understood in terms of collective decay of the ensemble.

We imagine a two-level system (TLS) consisting of $|s\rangle = 5P_{3/2}$ and $|g\rangle = 5S_{1/2}$ as excited and ground state, respectively. Let γ be the atomic rate of spontaneous emission from the excited state and λ the transition wavelength of the TLS.

The wave function of the coherence, i.e., the atomic wave function of the ensemble with N atoms immediately after the read in process, has the form of a W-state [27]

$$|\psi\rangle = \frac{1}{\sqrt{N}} \sum_{j=1}^N e^{i\delta k r_j} e^{i\delta k \cdot v_j t} |j\rangle, \quad (2.71)$$

where $|j\rangle = |g_1, \dots, s_j, \dots, g_N\rangle$ is the state of a single photon excitation of atom j from ground state $|g\rangle$ to the excited state $|s\rangle$. Again, δk is the mode mismatch, i.e., the net momentum of the coherence, r_j is the position of atom j and v_j the velocity of atom j . Note that the ensemble is described by an entangled W-state. This only applies if the individual emitters in the ensemble are indistinguishable. This indistinguishability can be achieved if the ensemble emission is detected in the far-field, i.e., the mean inter-atomic distance d is smaller than the wavelength λ .

It is important to note that the expectation of the excitation number operator $\hat{n} = \sum_i |i\rangle \langle i|$ is

always $\langle \psi | \hat{n} | \psi \rangle = 1$, i.e., we only have one single photon excitation in total. This assumption breaks down if the signal field is a multi-photon pulse.

Following the analysis of super- and subradiant states in [28], we can investigate the collective decay of the above state.

The entangled state of the ensemble at $t = 0$ is identical to the superradiant state that is introduced in [28]. It reads:

$$|\psi_{Dicke}\rangle = \frac{1}{\sqrt{N}} \sum_{j=1}^N e^{i\delta k r_j} |j\rangle. \quad (2.72)$$

We will use this non-dephased state to understand and compare the effect of dephasing on the collective decay rate.

For an ensemble of N TLS emitters, the collective rate of decay reads [29]

$$\Gamma = \sum_{i,j} \Gamma^{i,j} \langle \psi | \sigma_i^+ \sigma_j^- | \psi \rangle, \quad (2.73)$$

where $\Gamma^{i,j}$ captures correlated decay of atoms i, j and σ_i^+ / σ_i^- are the creation/annihilation operators of photonic excitations for atom i .

The velocities of the atoms in the ensemble are sampled from a Maxwell-Boltzmann distribution. That means that the velocities are symmetrically distributed around zero, i.e., equal number of velocities classes with opposite sign.

Then, without loss of generality and assuming N is even, we can relabel the indices of the atoms such that

$$v_j = \begin{cases} > 0, & j \in [1, N/2] \\ < 0, & j \in [N/2 + 1, N] \end{cases} \quad (2.74)$$

and then rename $\bar{j} = j + N/2$. We also sort the labels such that $v_j = -v_{\bar{j}}$. For the sake of simplicity we will limit the analysis to one dimension.

The wave function of the thermal ensemble then reads:

$$|\psi\rangle = \frac{1}{\sqrt{N}} \sum_{j=1}^{N/2} [e^{i\delta k r_j} e^{i\delta k v_j t} |j\rangle + e^{i\delta k r_{\bar{j}}} e^{i\delta k v_{\bar{j}} t} |\bar{j}\rangle] \quad (2.75)$$

$$= \frac{1}{\sqrt{N}} \sum_{j=1}^{N/2} [e^{i\delta k r_j} e^{i\delta k v_j t} |j\rangle + e^{i\delta k r_{j+N/2}} e^{i\delta k v_{j+N/2} t} |j + N/2\rangle]. \quad (2.76)$$

The transition element for spontaneous emission of atom i reads:

$$\langle g | \sigma_i^- | \psi \rangle = \frac{1}{\sqrt{N}} \sum_{j=1}^{N/2} [e^{i\delta k r_j} e^{i\delta k v_j t} \delta_{i,j} + e^{i\delta k r_{j+N/2}} e^{i v_{j+N/2} t} \delta_{i,j+N/2}] \quad (2.77)$$

$$= \frac{2}{\sqrt{N}} [e^{i\delta k r_i} e^{i\delta k v_i t}]. \quad (2.78)$$

Since each velocity class is populated differently, we have to weigh each velocity with the Maxwell-Boltzmann dist. $f(v) = \sqrt{\frac{m}{2\pi k_B T}} e^{-\frac{mv^2}{2k_B T}}$.

We get:

$$\langle g | \sigma_i^- | \psi \rangle = \frac{1}{\sqrt{N}} \int_{\mathbb{R}} dv_i f(v_i) [e^{i\delta k r_i} e^{i\delta k v_i t}] \quad (2.79)$$

$$\approx \frac{1}{\sqrt{N}} \int_{\mathbb{R}} dv f(v) [e^{i\delta k r_i} e^{i\delta k v t}] \quad (2.80)$$

$$= \frac{1}{\sqrt{N}} e^{i\delta k r_i} \left[\exp \left[-\frac{(\delta k t)^2 k_B T}{2m} \right] \sqrt{\frac{2\pi k_B T}{m}} \sqrt{\frac{m}{2\pi k_B T}} \right] \quad (2.81)$$

$$= \frac{1}{\sqrt{N}} e^{i\delta k r_i} \exp \left[-\frac{(\delta k t)^2 k_B T}{2m} \right], \quad (2.82)$$

where in the approximation we take the average Doppler phase factor.

The rate of spontaneous emission is then

$$\Gamma = \sum_{i,j} \Gamma^{i,j} \langle \psi | \sigma_i^+ \sigma_j^- | \psi \rangle \quad (2.83)$$

$$= \sum_{i,j} \Gamma^{i,j} \langle \psi_{Dicke} | \sigma_i^+ \sigma_j^- | \psi_{Dicke} \rangle \times \exp \left[-\frac{(\delta k t)^2 k_B T}{2m} \right]. \quad (2.84)$$

The characteristic time scale of this rate reduction is $\tau_D = \sqrt{\frac{m}{\delta k^2 k_B T}}$, just as derived for the Doppler dephasing in Eq. 2.56.

We see that for high temperatures and long evolution times the rate reduces.

3

Hyperfine optical pumping

Contents

3.1 Theory of optical pumping	34
3.2 Atomic beam transit	36
3.3 Implementation of optical pumping	38
3.3.1 Spectrum calibration	39
3.3.2 Pulsed pumping	40
3.3.3 CW pumping	42
3.4 Simulation of optical pumping with <i>ElecSus</i>	42
3.4.1 Pulsed pumping	44
3.4.2 CW pumping	46

The GSM in DRAGON is a crucial feature to overcome the lifetime limitation in ORCA memories. However, creating a coherence between the hyperfine ground states requires that the mapping state $|b\rangle$ is empty before mapping to it. Otherwise the remaining atoms in $|b\rangle$ would mix with the atoms of the initial coherence S_{gs} . This would lead to noise photons in the read out process. Therefore, in order to depopulate the state $|b\rangle$, we need to apply optical pumping of the hyperfine state.

This section introduces the theoretical framework and the idea behind optical pumping. Furthermore, we investigate how the transit of atoms in and out of the pumping beam affects optical pumping. After presenting the experimental results obtained, we conclude the section with numerical investigations using the software package *ElecSus*.

It is important to note that another effect of pumping is the increase of optical depth. By transferring population from the mapping state $|b\rangle$ to the initial state $|g\rangle$, we effectively increase the

optical depth via an increase in the number density of state $|g\rangle$. This can lead to an improvement of memory efficiencies.

3

3.1 Theory of optical pumping

The method of optical pumping can be used in atomic ensembles to change the population of energy levels. We outline this method for our purposes by using a simplified three level system.

In optical pumping, an additional light field, the pump beam, is focused on the atomic ensemble. Atoms within the pump beam have a chance of being excited to higher energy levels. The probability of this process is proportional to the Rabi frequency of the addressed transition and therefore also directly proportional to the applied laser intensity.

The dynamics for a three level system as in Fig. 3.1 are captured by a rate equation model (follow-

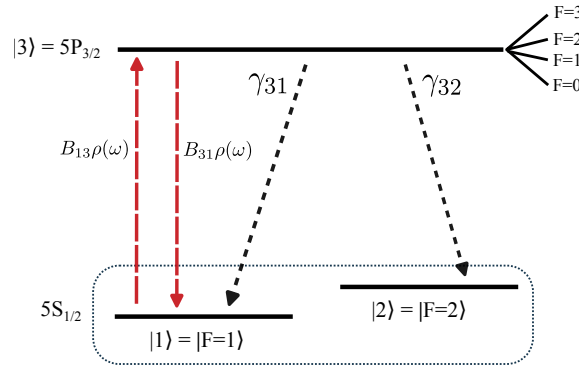


Figure 3.1: Simplified three level system for pumping of hyperfine level $F = 1$. See Sec. 3.1 for definition of symbols.

ing [30]). The excited state decay rates γ_{31}, γ_{32} are determined from the ratio of Clebsch-Gordan coefficients C_{ik} , with i, k the initial and final state index. The total decay rate of the excited state $|3\rangle$ is $\gamma_3 = 1/\tau = \gamma_{31} + \gamma_{32}$, e.g., for the ^{87}Rb D2 line $\tau = 26.25$ ns. We then have [30]

$$\gamma_{31} = \frac{C_{31}^2}{C_{31}^2 + C_{32}^2} \gamma_3, \quad \gamma_{32} = \frac{C_{32}^2}{C_{31}^2 + C_{32}^2} \gamma_3. \quad (3.1)$$

The idea of optical pumping is to excite atoms in an initial state, i.e., $|1\rangle$ or $|2\rangle$, to the excited state $|3\rangle$ and then let the atoms de-excite according to the branching ratio of spontaneous emission. For many repetitions of this process, the initial state will be depopulated, as long as there is a finite probability to decay into the other ground state.

For DRAGON we want to pump the ^{87}Rb D2 line. It is important to realise that in the state $|3\rangle = |5P_{3/2}\rangle$ there are several hyperfine sublevels $F = 0, 1, 2, 3$ that can be addressed.

For allowed electric dipole transitions we must have $\Delta F = 0, \pm 1$. That implies that pumping the transition $|1\rangle = |5S_{1/2}, F = 1\rangle \rightarrow |5P_{3/2}\rangle$ resonantly can only populate the states $|5P_{3/2}, F = 0, 1, 2\rangle$. Similarly, pumping the transition $|2\rangle = |5S_{1/2}, F = 2\rangle \rightarrow |5P_{3/2}\rangle$ will only lead to population in $|5P_{3/2}, F = 1, 2, 3\rangle$. The state $|5P_{3/2}, F = 0\rangle$ can only be populated from $|5S_{1/2}, F = 1\rangle$, the state $|5P_{3/2}, F = 3\rangle$ only from $|5S_{1/2}, F = 2\rangle$. These states we can therefore exclude from our analysis as they do not result in population transfer.

For the other states however, we find from tabulated values in [30] a branching ratio of $\gamma_{31}/\gamma_{32} = 2$. It is therefore more likely for $|3\rangle$ to decay into $|1\rangle$ via spontaneous emission.

We can now formalise the rate equation model for the three level system.

Let n_i be the fractional number density of atoms in state $|i\rangle$ of the optically pumped population distribution, such that $\sum_i n_i = 1$. Similarly, let N_i be the fractional number density of the equilibrium distribution, i.e., $N_i = g_i n_V / (g_1 + g_2)$, with g_i the hyperfine degeneracy of state $|i\rangle$. Again, n_V is the number density of a volume element as defined in Sec. 2.2.

The rate equation for the optically pumped atoms also depends on the rate Γ_0 , which is the rate by which atoms leave and enter the pump beam. This rate depends on the temperature of the atomic ensemble and is given as $\Gamma_0 = 2\bar{v}\sqrt{\ln 2}/R$, with pump beam radius R and Maxwell-Boltzmann mean velocity \bar{v} . If the transition $|1\rangle \rightarrow |3\rangle$ is pumped, the equations read:

$$\frac{dn_1}{dt} = -n_1(B_{13}\rho(\omega) + \Gamma_0) + n_3(B_{31}\rho(\omega) + \gamma_{31}) + N_1\Gamma_0 \quad (3.2)$$

$$\frac{dn_2}{dt} = \Gamma_0(-n_2 + N_2) + n_3\gamma_{32} \quad (3.3)$$

$$\frac{dn_3}{dt} = n_1B_{13}\rho(\omega) - n_3(B_{31}\rho(\omega) + \gamma_3 + \Gamma_0). \quad (3.4)$$

Here $B_{ik} = \frac{\pi e^2}{\epsilon_0 \hbar^2 g_i} \sum_{m_F} |\mu_{ik}|^2$ is the Einstein coefficient for a transition $|i\rangle \rightarrow |k\rangle$ with corresponding electric dipole element $|\mu_{ik}|^2$. The spectral energy density for a monochromatic beam is denoted $\rho(\omega)$.

In the steady-state ($\dot{n}_i = 0$) we find

$$n_1 = \frac{1}{1 + \frac{g_3}{g_1}\beta\alpha}, \quad (3.5)$$

with saturation and pumping parameters

$$\alpha = \frac{B_{31}\rho}{B_{31}\rho + \gamma_3 + \Gamma_0}, \quad \beta = 1 + \frac{\gamma_{32}}{\Gamma_0}, \quad (3.6)$$

respectively.

We see how the number density of $|1\rangle$ depends on the experimental parameters B_{31} and Γ_0 .

3.2 Atomic beam transit

As outlined in the rate equations in Sec. 3.1, the efficiency of optical pumping is also limited by the movement of atoms in and out of the beam. We can simulate these dynamics and make predictions as to how they will affect optical pumping.

The main question we want to answer is: what is the mean pumping efficiency at a random time for atoms within the beam profile?

In the final DRAGON protocol (see Fig. 2.3), before the memory operation is started the atomic ensemble is optically pumped. It is the population distribution immediately after the pumping sequence that is key for the (noise) performance of the whole protocol. We therefore need to know what the mean pumping efficiency will be after a certain pumping time.

We will answer this question in a simplified model, by relating the pumping efficiency to the mean exposure time of atoms to the pump beam.

Using the three level system in Fig. 3.1, we discretise the pumping procedure: a pumping cycle refers to the excitation of an atom to $|3\rangle$ and, after $\tau \approx 26.5$ ns, its de-excitation into levels $|1\rangle$ or $|2\rangle$ with probabilities p_{31} or p_{32} , respectively. We assume that the excitation from the ground state is instantaneous (compared to the time scales of de-excitation).

Focusing on pumping the $F = 1$ level, we define that the ensemble is pumped, if only 1% of the initial population remains in $F = 1$. To reach this level of depopulation, a certain number of pumping cycles n_p is required. We find that

$$p_{31}^{n_p} \leq 0.01 \rightarrow n_p = \frac{\log(0.01)}{\log(p_{31})}. \quad (3.7)$$

The probability p_{31} of an excited atom to decay to the state $|1\rangle$ within the lifetime τ is given by the ratio of decay rates from spontaneous emission. From Sec. 3.1 we can conclude that $p_{31} = 0.66$.

Assuming that initially the number densities of $|1\rangle$ and $|2\rangle$ are distributed as $N_i = g_i/(g_1 + g_2)$, we require that a sufficiently high fraction of atoms stays within the pump beam. With this we can assure that the atomic ensemble, with which the probe is then interacting, has encountered the required amount of pumping cycles n_p for pumping level $|1\rangle$.

If we only consider spontaneous decay, i.e., a static atomic ensemble, we estimate $n_p \approx 11$. Since a de-excitation of the ensemble can only occur every $\tau \approx 26.5$ ns, we need to let the pump interact with the ensemble for $t_{pump} = \tau n \approx 293$ ns.

Taking into account the effect of temperature, radius of the pump beam and atom movement

changes the situation. This can best be seen by simulating the movement of atoms in and out of the pump beam. For this we sample a number of N atoms, initialise them with random positions within and without a circle of radius R and velocities drawn from a Maxwell-Boltzmann distribution at temperature T .

A schematic of how the atoms evolve w.r.t. the pump beam is shown in Fig. 3.2. Any random

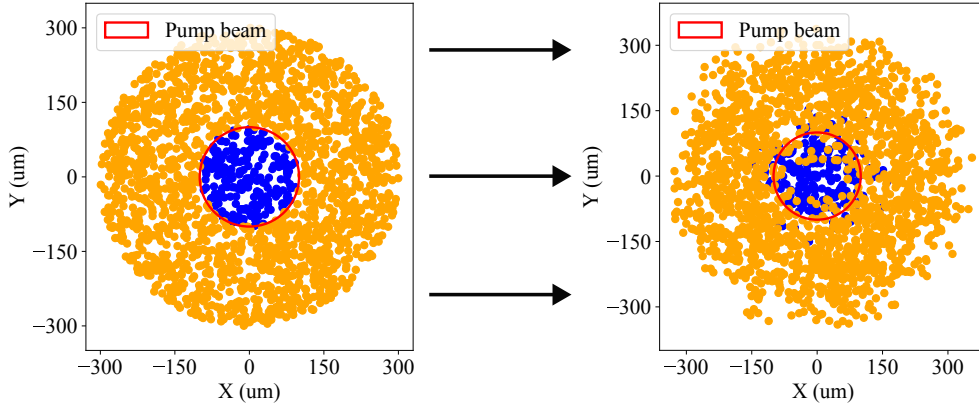


Figure 3.2: Evolution of atoms with $R = 100 \mu\text{m}$ and $T = 350 \text{ K}$. The atoms that are initially inside the pump beam are in blue, the atoms initially outside in orange. The left part shows the positions after initialisation, the right part shows the positions after evolution of t_{pump} . The black arrows indicate the time evolution.

atom has to be exposed to the pump beam for at least t_{pump} in order to depopulate the hyperfine state $F = 1$. By tracking the motion of the simulated particles and their exposure to the beam, we can obtain an exposure time for each atom and hence a mean exposure time of all atoms in the beam profile at a given time.

If we let the system evolve for exactly t_{pump} with $R = 100 \mu\text{m}$ and $T = 350 \text{ K}$, we find an average exposure to the pump beam of $\tau_{exp} \approx 250 \text{ ns}$. From this we can conclude that the average pumping efficiency of the ensemble is $\eta \approx 0.85$. The evolution of average exposure corresponding to Fig. 3.2 is shown in Fig. 3.3.

This simple analysis gives us an idea of the time scales of pumping and the effects of temperature and pump beam radius. The obtained time scale t_{pump} has to be compared to the time scale of re-thermalisation of the hyperfine ground states. Since the transition between the hyperfine states $F = 1$ and $F = 2$ is dipole-forbidden and the excited state is energetically separated by hundreds of THz, the only relaxation mechanism is spin relaxation via collisions. As the vapour cell contains only a dilute ^{87}Rb gas, we assume to be in the ballistic collision regime. The rate of collisions is given as

$$\gamma_{coll} = n_V(T)\sigma\bar{v}, \quad (3.8)$$

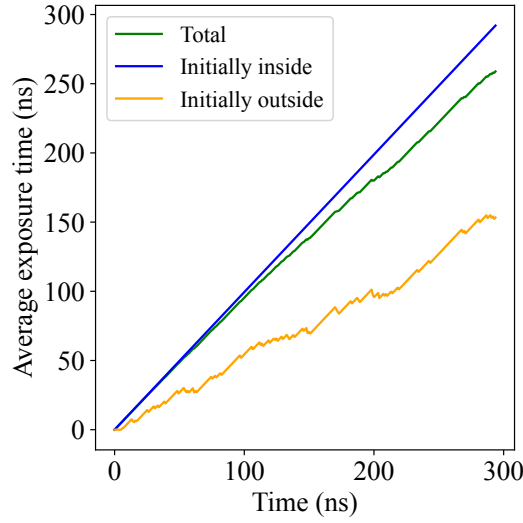


Figure 3.3: Average exposure of atoms within the pump profile as function of time. The exposure time of atoms that were initialised inside the beam is shown in the blue graph, the exposure time of atoms that were initially outside the beam in orange. The green line shows the average exposure for both green and orange dots at a specific time.

where $n_V(T)$ is the number density at temperature T , σ is the scattering cross-section and \bar{v} is the average relative velocity of the atoms in the ensemble. Using the vapour pressure for the liquid phase, $\sigma = 8 \times 10^{-19} \text{ m}^2$ and $\bar{v} \approx 300 \text{ m s}^{-1}$ (for $T = 60 \text{ }^\circ\text{C}$) we get $\gamma_{coll} \approx 200 \text{ Hz}$. Conservatively we can therefore assume a relaxation time for optical pumping of $\approx 1 \text{ ms}$. Note that this time scale is much larger than any other dynamics of the memory. We can therefore ignore the relaxation for a memory with short storage time.

3.3 Implementation of optical pumping

In the particular case of DRAGON in ^{87}Rb , we need to empty the hyperfine state $F = 2$ or $F = 1$ of $|5S_{1/2}\rangle$. This requires a light field on resonance with the relevant transition, i.e., $\nu_{F=2} = 384.2278 \text{ THz}$ or $\nu_{F=1} = 384.2346 \text{ THz}$. The source of the pumping field can either be a pulsed or CW laser, each leading to a different effect of pumping.

Pumping is performed on an atomic ensemble in a cylindrical vapour cell containing ^{87}Rb with traces of ^{85}Rb (around 2%). Furthermore, we install a reference cell, which contains the natural abundance composition of the two Rubidium isotopes ^{87}Rb and ^{85}Rb . The reference cell will be used for spectrum calibration only, no memory operation is performed here.

The experimental setups of ORCA and DRAGON are discussed in Sec. 4.1.1 and 4.1.3, respectively. Here we present the experimental results of optical pumping.

3.3.1 Spectrum calibration

The effect of optical pumping is investigated by performing non-Doppler-resolved spectroscopy for ^{87}Rb . However, to benchmark any effects of pumping and especially to calibrate the frequency axis of the obtained spectrum, a reference spectrum is required.

Such a reference spectrum was obtained by installing a reference vapour cell, which contains the natural abundance composition of Rubidium, i.e., ^{87}Rb (27.8%) and ^{85}Rb (72.2%), and is kept at room temperature.

The advantage of the reference spectrum is that it remains constant and four absorption dips for the ground states are clearly visible. The reference spectrum obtained from measurements on a photo diode and processed on an oscilloscope (*Keysight InfiniiVision DSOX6004A*) can be seen in Fig. 3.4. The frequency axis has been normalised to be relative to the ^{87}Rb D2 line transition at

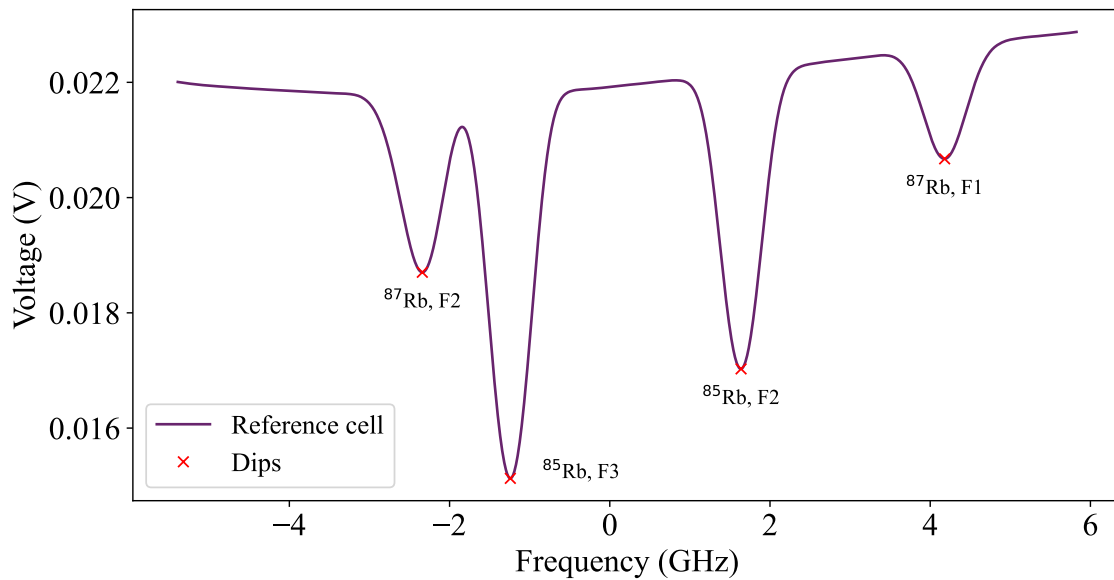


Figure 3.4: Spectrum of reference cell containing Rubidium in natural abundance. The hyperfine states corresponding to each absorption dip are annotated.

$\nu = 384.2304$ THz, i.e., the transition of $F = 2$ in ^{87}Rb is set to -2.563 GHz.

All reference spectra are obtained by scanning a CW source (*Toptica DL pro*) around the D2 transition at $\nu = 384.2304$ THz over a certain frequency range. Optimally, the laser sweep is linear in frequency, meaning that there is a fixed conversion between time and frequency. However, we find this not to be the case. A calibration of the frequency axis using the spectrum of a reference cell is therefore necessary. The well known frequencies of the absorption profile in the natural abundance reference cell are used to fit a relation between time of the laser sweep and frequency. More details on the method are given in Section 3.4.

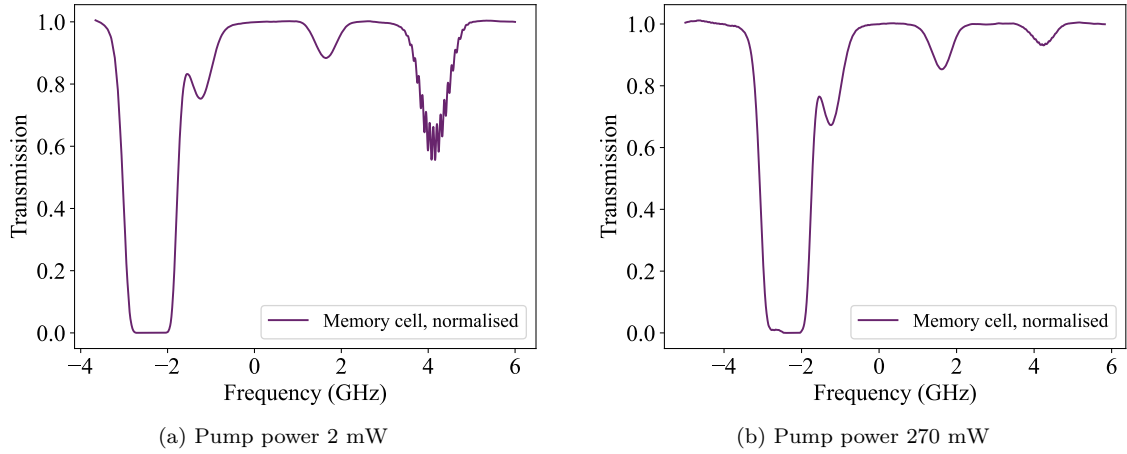


Figure 3.5: Transmission spectra of the vapour cell with different pump powers taken from oscilloscope data. Note that due to data calibration the transmission is normalised differently.

3.3.2 Pulsed pumping

Optical pumping can be performed using a pulsed Ti:Sapph laser. Here we pump the state $F = 1$, i.e., the laser is tuned to $\nu_p = \nu_{F=1} = 384.2346$ THz. As

Fig. 3.5 shows results for temperature $T = 39$ °C, a pump frequency $\nu_p = 384.2344$ THz, a diameter at pump beam waist of $d_p = 300$ μm and different intensities of the pump beam. The signal light field is centered around $\nu = 384.2304$ THz and sweeps ± 10 GHz. The signal beam intensity was attenuated to $4\mu\text{W}$ with a diameter at beam waist of $d_s = 250$ μm .

An interesting feature of pulsed pumping is the spectral decomposition of the pumping beam. This can already be seen in Fig. 3.5a and is enhanced for better visibility in Fig. 3.6. Due to the short temporal profile of the pulses, the light contains various spectral components. The visible frequency comb in Fig. 3.6 shows the spectrum composition of the pulse. This is clearly visible for low intensities as in Fig. 3.5a but can also be observed for other intensities.

As outlined before, another important factor for the pumping efficiency is the temperature of the vapour. While Fig. 3.5 shows spectra for $T \approx 40$ °C, Fig. 3.7a shows the normalised transmission spectrum for $T \approx 75$ °C. The pump beam diameter is still $d_p = 300$ μm and the signal $d_s = 250$ μm . With the vapour at higher temperatures, higher velocity classes are populated and the detrimental effect of Doppler shifts to optical pumping is enhanced. The effect of pumping is visibly smaller. By switching to frequencies close to $\nu_p = \nu_{F=2} = 384.2278$ THz we can also perform optical pumping on $F = 2$ and depopulate this level. The effect of pumping for $F = 2$ can be seen in Fig. 3.7b.

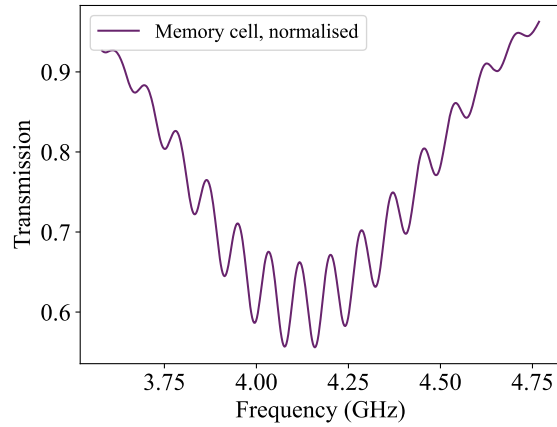
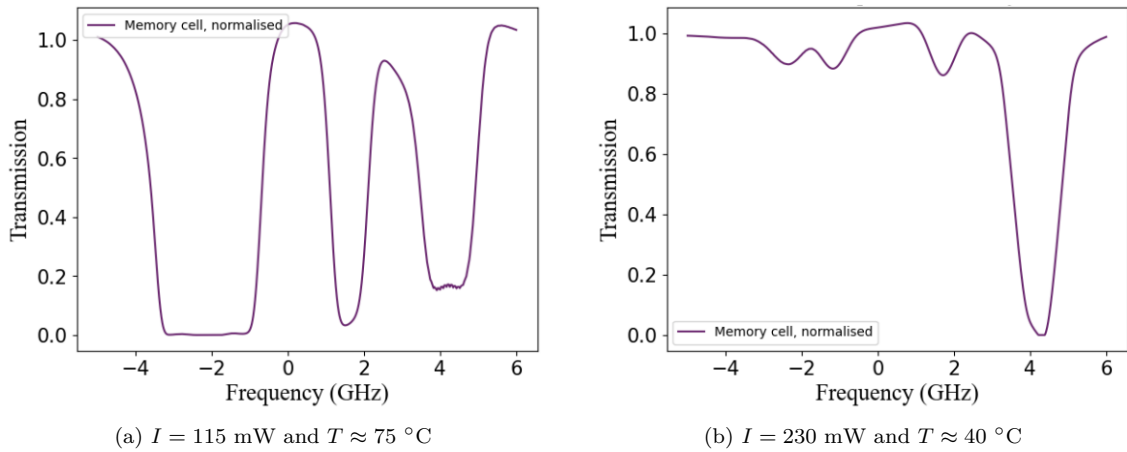


Figure 3.6: Transmission spectrum for pumped region for $I = 2$ mW.



(a) $I = 115$ mW and $T \approx 75$ °C

(b) $I = 230$ mW and $T \approx 40$ °C

Figure 3.7: Transmission spectra for optically pumping a) $F = 1$ and b) $F = 2$.

In order to reduce the required power of the pump beam, we can adjust the relative sizes of pump and signal beams. By exchanging the lenses of the pump telescope (see Sec. 4.1.3 for more detail), the pump diameter was increased to $d_p = 400$ μm , while the signal was maintained at $d_s = 250$ μm . The effect of this change can be seen in Fig. 3.8. Comparing Fig. 3.5b with Fig. 3.8 the effect of adjusted beam size is evident: we can achieve higher efficiency with less power. We can understand this effect in the context of atom transit as introduced in Sec. 3.2. As we increase the size of the pump beam, the average exposure to pumping of atoms within the signal beam increases.

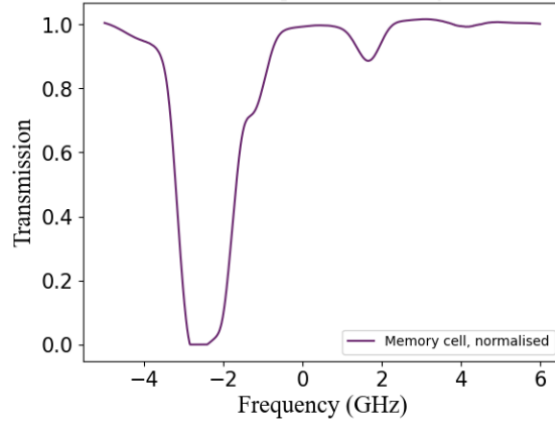


Figure 3.8: Transmission spectrum for optically pumping $F = 1$ with $I = 100$ mW and $T \approx 40$ °C

3.3.3 CW pumping

Optical pumping can also be achieved using a CW light source for pumping. Here we used a *Toptica DFB pro* at $\nu_p = 384.2344$ THz. A characteristic spectrum with CW pumping is given in Fig. 3.9. This also clearly demonstrates the difference between pulsed and CW light: due to the reduced linewidth of the CW light, the pumping efficiency is strongly reduced for frequencies further away from the pumping frequency. This is an effect of the Doppler shift of the atoms and is the disadvantage of CW pumping. The advantage is that the pumping efficiency at the pumping transition is much larger since the power spectral density is focused more strongly around the pumping transition.

For CW pumping, the pumping efficiency is vastly different for atoms in different velocity classes and gives a characteristic W-shape in the pumping region. This will be a problem when estimating the pumping efficiency of the whole ensemble, which is addressed in more detail in Sec. 3.4.2.

3.4 Simulation of optical pumping with *ElecSus*

The *ElecSus* software package [31] aims to extract various parameters from absorption spectra of weakly probed Alkali vapours.

This is achieved by fitting the complex electric susceptibility χ_i for different transitions i of the atomic species at hand:

$$\chi_i(\Delta) = \frac{c_i^2 d^2 N_a}{\epsilon_0 \hbar} V(\Delta). \quad (3.9)$$

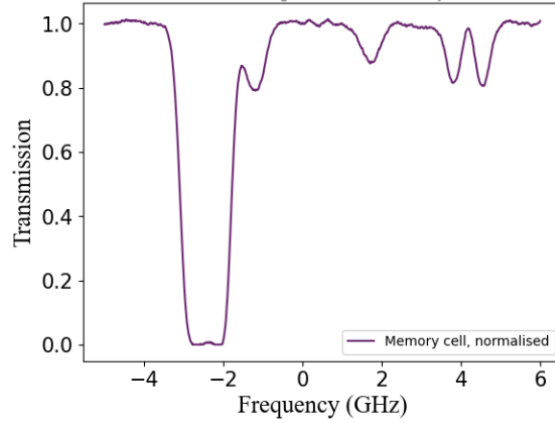


Figure 3.9: Transmission spectrum for CW pumping of $F = 1$ with $I = 14$ mW and $T \approx 40$ °C

The frequency detuning axis is Δ (detuning w.r.t. the D2 transition $\nu = 384.2304$ THz), the number density N_a (for one magnetic hyperfine sublevel), the relative line strength of a transition is included in the Clebsch-Gordan coefficients c_i and d is the reduced dipole matrix element. The functional form of the susceptibility is given by the Voigt function $V(\Delta)$. The Voigt function results from the convolution of a Gaussian and Lorentzian function. It takes into account the forms of homogeneous (Lorentzian) and inhomogeneous (Gaussian, Doppler) broadening.

The number density of a hyperfine m_F sublevel is given by

$$N_a = \frac{F_i n_V}{2(2I + 1)}, \quad (3.10)$$

where F is the isotopic fraction and the denominator denotes the hyperfine degeneracy of the ground state, with I the nuclear spin of the isotopic species. Hence every m_F level in the ground state has equal number density associated. The total number density n_V can be obtained via $n_V = P_V V / RT$.

In its original form the *ElecSus* package hinges upon the assumption that the probe laser intensity is in the weak probe regime, i.e., no substantial population transfer of the hyperfine states. This assumption is systematically violated when optical pumping is performed.

Therefore, it is essential to extend the *ElecSus* code such that population shift is taken into account.

We can model a population shift by adjusting the relative line strength of the transitions. The idea is to add a parameter p that modulates the Clebsch-Gordan (CG) coefficients c_i for different hyperfine states selectively.

Before any population transfer via optical pumping occurs, we initialise $p = 0$, i.e., each hyperfine state is weighted equally with no population shift.

In this framework we can interpret the pumping of a hyperfine state, e.g. $F = 1$, as a change of the transition strength of the possible transitions in the D2 line via the parameter p .

Mathematically this is equivalent to a shift in hyperfine populations N_1 and N_2 , for $F = 1$ and $F = 2$, respectively. We can then write the susceptibility in the presence of population transfer as:

$$\chi^{87}(\Delta) = \sum_{i,F=1}^{g_1} \frac{c_i^2(1+p/g_1)d^2N_a}{\epsilon_0\hbar} V(\Delta) + \sum_{i,F=2}^{g_2} \frac{c_i^2(1-p/g_2)d^2N_a}{\epsilon_0\hbar} V(\Delta) \quad (3.11)$$

$$= \sum_{i,F=1}^{g_1} \frac{c_i^2 d^2 N_1}{\epsilon_0 \hbar} V(\Delta) + \sum_{i,F=2}^{g_2} \frac{c_i^2 d^2 N_2}{\epsilon_0 \hbar} V(\Delta). \quad (3.12)$$

As the total number of atoms in the ensemble is assumed to remain constant, we must have $g_1 N_1 + g_2 N_2 = g_1 N_a + g_2 N_a = n_V$, with $N_1 = (1 + p/g_1)N_a$, $N_2 = (1 - p/g_2)N_a$ and n_V the total number density of atoms.

The fraction of atoms in the hyperfine state $F = 1$ of the ground state manifold of ^{87}Rb after a population transfer via pumping has occurred is given by

$$r_1(p) = \frac{g_1 N_1}{g_1 N_1 + g_2 N_2} = \frac{g_1(1+p/g_1)}{g_1(1+p/g_1) + g_2(1+p/g_2)}, \quad (3.13)$$

such that for $p = 0$ we obtain the initial equilibrium ratio of $r_1 = 3/8 = 0.38$. Note that the initial ratio is not 0.5. This follows from the assumption of uniform population of the m_F states (see Eq. 3.10). The fraction is experimentally accessible by measuring the absorption dips in the atomic spectrum. More precisely, in the adjusted *ElecSus* code we can directly fit the parameter p , which determines the ratio $r(p)$.

The pumping efficiency for optical pumping of the transition $|5S_{1/2}, F = 1\rangle \rightarrow |5P_{3/2}\rangle$ is then defined as $\eta_p(p) = 1 - r_1(p)/r_1(0)$.

3.4.1 Pulsed pumping

The performance of *ElecSus* for extraction of pumping efficiencies works best for pulsed pumping. The reason for that is the broad spectral range of the pulse that results in almost uniform pumping efficiency among the velocity classes. A more detailed investigation into pulsed pumping is given in Sec. 3.3.2.

The effect of pumping is most prominent for low temperatures. This follows from the movement of atoms and the limited extent of the pumping beam (see Sec. 3.2).

Figs. 3.10a to 3.10d show the absorption spectra for different pumping intensities at $F = 1$ together with the fitting residuals of the *ElecSus* fit and the achieved pumping efficiency $\eta_{F=1}$.

An important observation in this context is the saturation intensity for the pump beam: the difference in pumping efficiencies for $I = 270$ mW and $I = 2$ mW is less than 10%, whereas the applied intensities are vastly different.

The deviations of the fit are lower than 5% for high intensities but can reach up to 10% for $I = 2$ mW. The main reason for that is the calibration of the frequency axis: a slight offset of the fitted spectrum to the data results in large deviations.

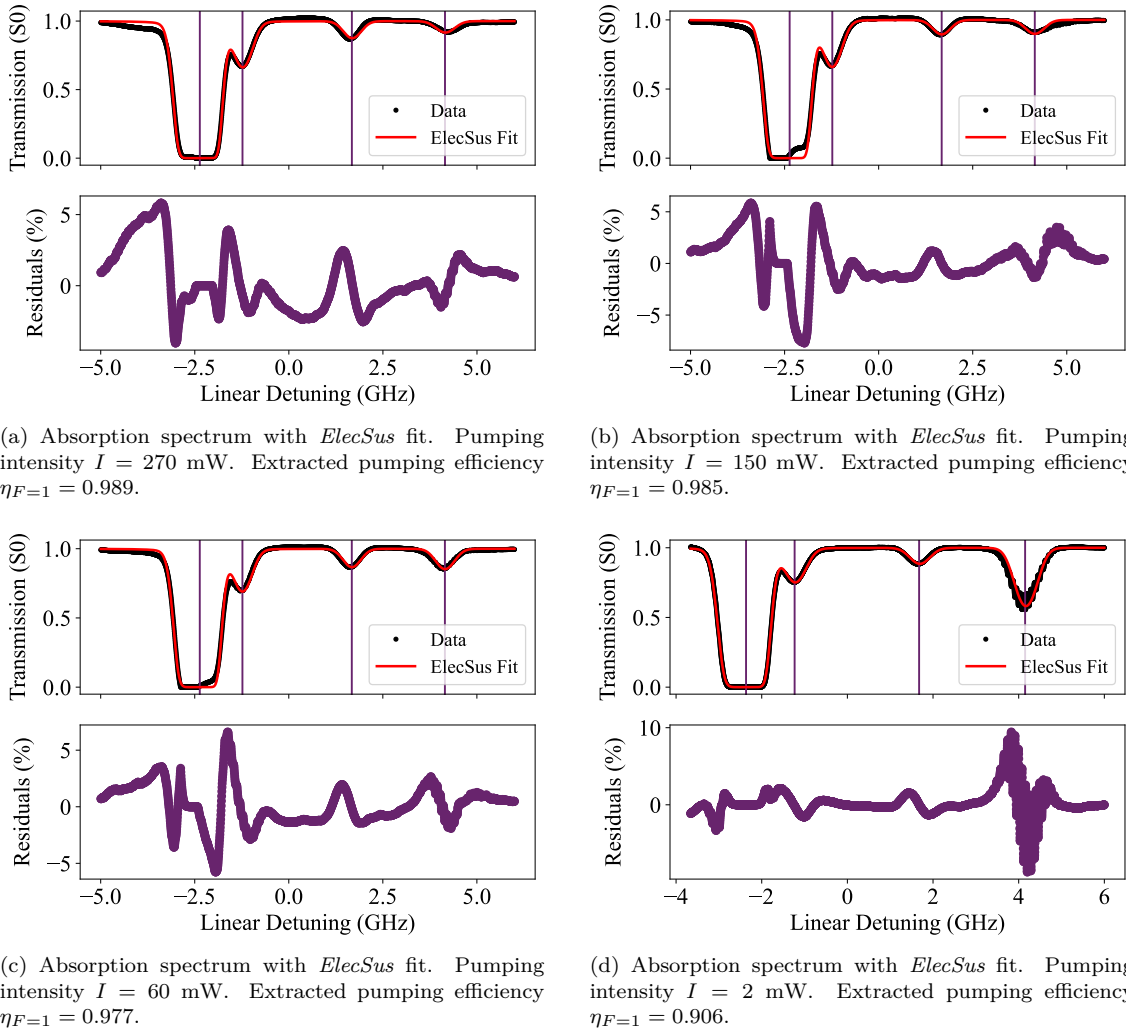


Figure 3.10: Data for pulsed pumping of level $F = 1$ for $T \approx 40$ °C. In each sub-figure the upper graph is the fitted spectrum, the lower graph shows the fitting residuals.

Switching the pumping transition to $|5S_{1/2}, F = 2\rangle \rightarrow |5P_{3/2}\rangle$ should not give different estimations for the pumping efficiencies since the reduced dipole element d is the same as for $|5S_{1/2}, F = 1\rangle \rightarrow |5P_{3/2}\rangle$. The efficiency should depend on the pumping intensity in the same way as for the

transition $|5S_{1/2}, F = 1\rangle \rightarrow |5P_{3/2}\rangle$. We can see that this indeed holds in Fig. 3.11.

In fact, we can expect better pumping performance for pumping the $F = 2$ state. This follows from Sec. 3.2: there is a higher chance to decay into $F = 1$ from the excited state and therefore depopulating $F = 2$ should be faster and more efficient.

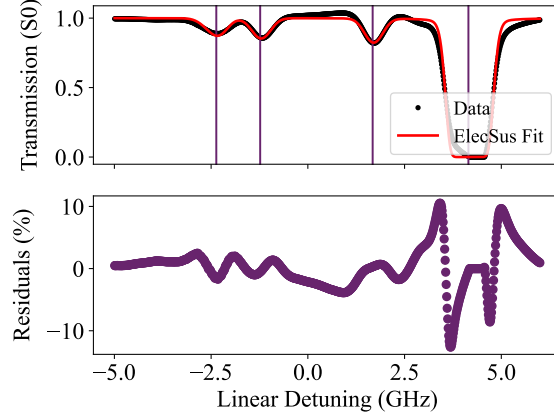


Figure 3.11: Fit and data for pulsed pumping of level $F = 2$ for $T \approx 40$ °C with $I = 230$ mW. The extracted pumping efficiency is $\eta_{F=2} = 0.989$.

3.4.2 CW pumping

If we pump the atomic ensemble with a CW source of limited linewidth, the different velocity classes are not as broadly addressed as for a pulsed source. That means that the pumping intensity is focused on only a small number of velocity classes with small Doppler shift.

This leads to a characteristic shape of the pumped spectrum (see Sec. 3.3.3 for more examples). As the modified version of *ElecSus* assumes equal pumping of each atom in the ensemble, the fit must necessarily deviate from the real picture. This can best be seen in Fig. 3.12. We can clearly see how in this case the *ElecSus* fit does not capture the qualitative shape in the pumping region. This is also captured in the large relative residuals between spectrum and fit.

However, we can overcome this issue by creating a mapping, which relates the normalised transmission to pumping efficiency. The necessary assumption here is that at zero transmission, i.e., total absorption, the pumping efficiency is negligible. This approximation is valid for low temperatures ($T \approx 40$ °C), but fails for higher temperatures. The reason for that is the increased optical depth for high temperatures, which results in total absorption even for non-negligible pumping.

Assuming that at full absorption there is no deviation from the equilibrium population, the distance of the pumped absorption profile to the non-pumped absorption profile is proportional to pumping efficiency. Using *ElecSus*, we can generate a mapping, which relates this distance in

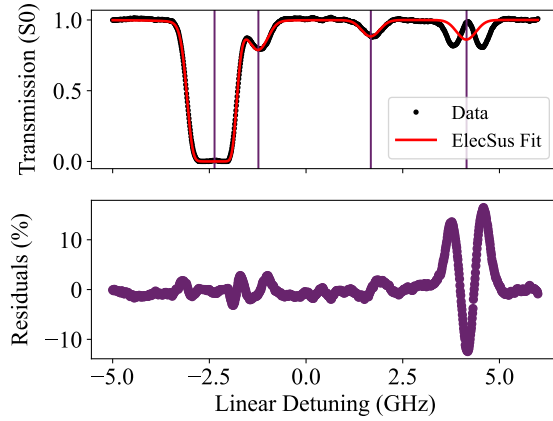
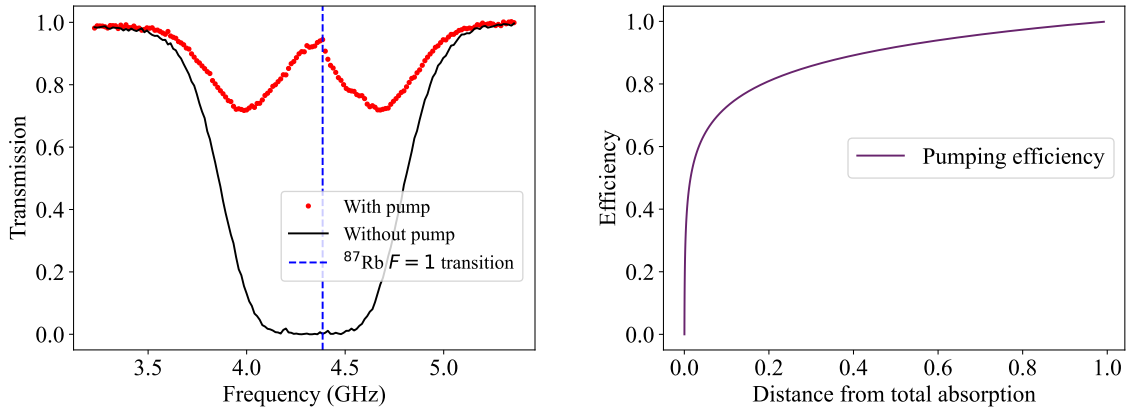


Figure 3.12: Fit and data for CW pumping of level $F = 1$ for $T \approx 40$ °C with $I = 14$ mW. The extracted pumping efficiency is $\eta_{F=2} = 0.977$.



(a) Pumping region for CW pumping with $I = 15$ mW and $T \approx 40$ °C

(b) Pumping efficiency map as a function of distance from total absorption

Figure 3.13: Efficiency map for transmission spectrum. a) The spectrum around pumping transition with and without pumping is obtained. b) Using *ElecSus*, the distance from total absorption is mapped to pumping efficiency.

transmission to pumping efficiencies. This is shown in Fig. 3.13b. By using such a map we can convert the transmission spectrum in Fig. 3.13a into corresponding pumping efficiencies.

The x-axis in Fig. 3.13a is in frequency, but by deconstructing the Doppler shift from the $F = 1$ transition frequency (dotted blue line in Fig. 3.13a) into velocity classes, we obtain Fig. 3.14a. The obtained shape of the pumping efficiency as a function of velocity resembles as Gaussian distribution centered around the pumping frequency. This is to be expected, since the velocity distribution parallel to the beam (transversal movement does not lead to a Doppler shift) is a Maxwell-Boltzmann distribution mirrored at $v = 0$. This Gaussian distribution is centered around $v = 0$ with a standard deviation of $\sigma = \sqrt{k_B T / m}$.

As expected, we find the highest pumping efficiencies for velocities around $v = 0$, because for static atoms the laser is closest to resonance with the pumping transition. However, one impor-

tant information is not included in Fig. 3.14a: the pumping efficiencies are not weighted with the velocity distribution. This information is crucial to determine the effective pumping efficiency in the ensemble since the velocity classes are not uniformly populated. By multiplying the efficiencies of the velocity classes with their corresponding probabilities, we obtain the cumulative pumping efficiency. This is shown in Fig. 3.14b. Here the x-axis shows the minimum pumping efficiency η_p and the y-axis the number density, i.e., the fraction of atoms that are pumped with at least η_p . For example (see red cross in Fig. 3.14b), roughly 35% of the atoms are pumped with at least $\eta_p = 0.99$. We can also extract the mean pumping efficiency $\bar{\eta}_p$ of the atoms from Fig. 3.14b. For the shown parameters we have $\bar{\eta}_{F=1} = 0.98244$, i.e., the average atom in the ensemble is pumped with more than 98.2%.

This will be useful information to determine e.g. the extent of fluorescence noise in DRAGON (Sec. 2.3) due to residual ground state population of state $|b\rangle$.

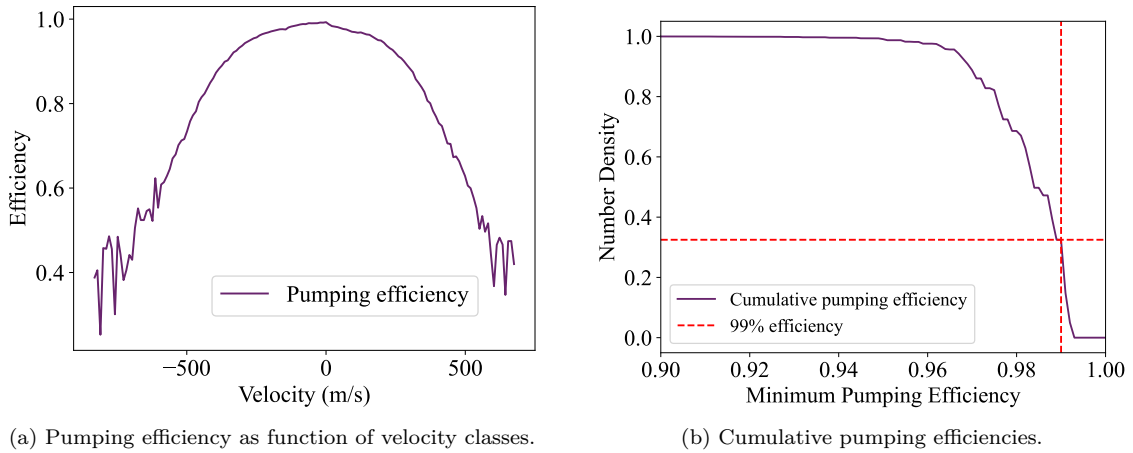


Figure 3.14: Data for CW pumping with $I = 15$ mW and $T \approx 40$ °C.

Implementation of DRAGON

Contents

4.1 Setup	50
4.1.1 ORCA	50
4.1.2 Pulse generation and synchronisation	51
4.1.3 DRAGON	52
4.1.4 EDFA	52
4.2 Operation of the memory	54
4.2.1 Pulse energy characterisation	54
4.2.2 CW background characterisation	55
4.2.3 CW leakage readout	56
4.2.4 Retrieval of stored signals	59
4.3 Simulation of optical Bloch equations	60
4.3.1 Control Rabi frequency	60
4.3.2 Optical depth	62
4.3.3 Frequency detuning	63
4.3.4 Simulation of storage and retrieval	63

The experimental path to establish the DRAGON protocol entails various different investigations. Before any of the characteristic functions of DRAGON can be implemented, we need to establish ORCA.

In order to be used for DRAGON later, we use a version of ORCA, where the signal is at $\lambda_s \simeq 780$ nm and the control at $\lambda_c \simeq 1529$ nm. This configuration of light fields is the reverse of the telecom ORCA presented in [21].

As discussed in Sec. 2.1.7 and 2.1.8, to extend ORCA to DRAGON we need to add light fields for GSM and rephasing. Unfortunately, these lasers have not been delivered within the time frame of the project to conclude the experimental implementation of GSM and rephasing.

Therefore, this section only outlines the experimental steps that have been taken to realise the full DRAGON protocol.

4.1 Setup

Both ORCA and DRAGON require setups that can be installed on an optical table. As we operate the memory in a warm state, no cryogenics are required. Therefore, beside the light field generation, all required parts fit onto a medium size area on a stabilised optical table.

This section introduces the experimental setups for both ORCA and DRAGON.

4.1.1 ORCA

The experimental setup for the base function of ORCA is depicted in Fig. 4.1.

The signal light field is generated in a Ti:Sapph laser (*Spectra-Physics Tsunami*), which outputs a Gaussian pulse with FWHM of approx. 300 ps every $\tau_s \approx 12.5$ ns at $\nu_s = 384.2223$ THz. On the other end, the control field is generated by a CW laser at $\nu_c = 196.0286$ THz (*santec TSL-510*). Note that with this combination of frequencies we excite the two-photon transition $|5S_{1/2}, F = 2\rangle \rightarrow |4D_{5/2}\rangle$.

Using an electro-optical modulator (EOM) (*iXblue MXER-LN-10*), we modulate the control light such that we obtain Gaussian pulses of approx. 300 ps FWHM. In order to reach sufficient pulse energies for the two-photon absorption in the read-in process, the control pulses after the EOM are amplified by an erbium-doped fiber amplifier (EDFA) (*PriTel LNHP-33*) (see Sec. 4.1.4 for more details).

The memory cell is a transparent glass cylinder of length $L = 13$ cm filled with ^{87}Rb ($\geq 98\%$) and ^{85}Rb ($\leq 2\%$). The cell windows are AR-coated (anti-reflective), i.e. high transmittivity for the signal frequency. We can determine the exact isotopic composition of the gas in the cell by referring to *ElecSus* simulations (see Sec. 3.4). The temperature of the cell is controlled via heating coils around the cylinder. Similar to the Rubidium fraction, the exact temperature of the gas can be extracted from *ElecSus* simulations and fitting to the absorption spectrum.

In order to fine-tune the polarisation and intensities at the optical table, we introduce a set of $\lambda/2$ - and $\lambda/4$ -waveplates (see Fig. 4.1).

Both signal and control light fields are focused by suitable lenses to the centre of the cell. For the signal we introduce two B-coated convex lenses with a focal length of $f_s = 250$ mm. This results

in a beam diameter at the centre of the cell of $d_s \approx 250 \mu\text{m}$. The lenses for the signal beam are also chosen in a way to produce a Rayleigh length z_R that is larger than the length of the cell L . This guarantees small change of the beam diameter in the interaction region of the memory. Since the signal is later detected, the second lens is required to convert the signal beam again into a collimated beam for coupling into optical fiber.

In order to maximise the read-in efficiency both control and signal beams should overlap at the centre of the cell. The control beam is focused to a diameter of $d_c \approx 300 \mu\text{m}$ by using a single C-coated lens with $f_c = 400 \text{ mm}$.

Any read-out signal is coupled into a fibre and detected by an array of superconductor-nanowire single photon detector (SNSPD)s (*Photon Spot Cryospot 4*). The detectors are cooled to about 700 mK and are located in a separate room.

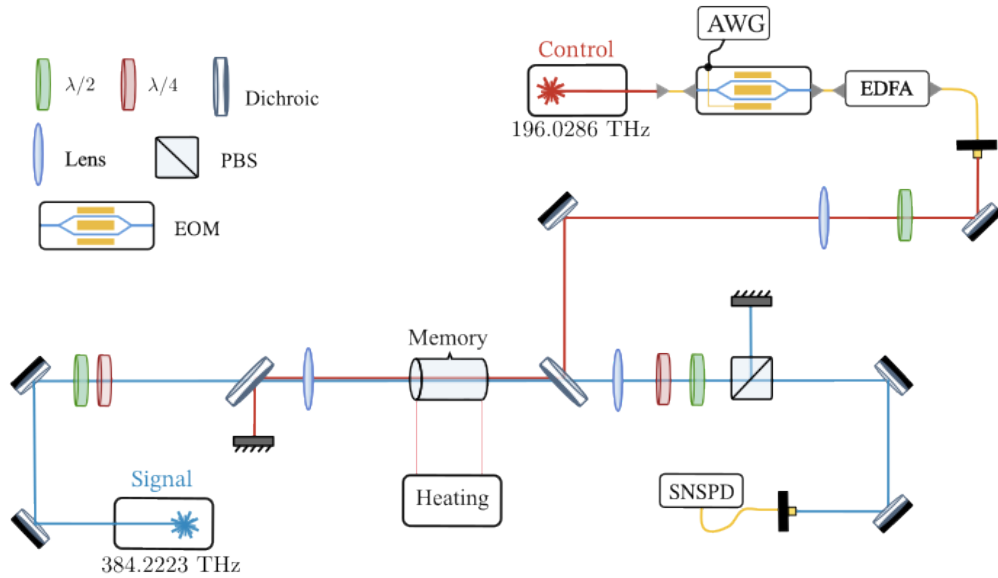


Figure 4.1: Installed ORCA setup

4.1.2 Pulse generation and synchronisation

An important factor of the read-in efficiency is the temporal overlap of control and signal pulses. In order to achieve this, the pulse repetition of the signal and the pulse generation of control pulses by the arbitrary waveform generator (AWG) (*Tektronix AWG70001A*) are linked.

The separation of signal pulses τ_s is controlled via a function generator (*Keysight 33600A*), which generates sinusoidal wave at a frequency $\nu_{ref} = 1/\tau_s \approx 80 \text{ MHz}$ and serves as a reference sig-

nal for the Ti:Sapph laser. At the same time, the same function generator creates a signal at $\tilde{\nu}_{ref} = \nu_{ref}/8$ with a rectangular shape. This signal is fed as a reference signal to the AWG.

The input to the AWG is a computer-generated waveform, i.e., a 1D array of values, that is generated and sent to the AWG via Ethernet. The length of each waveform is set to 1950 ns. Without the reception of a reference signal from the waveform generator, the AWG outputs waveform after waveform. However, for our purposes, the pulses of control and signal need to temporally overlap. A precise timing of the begin of each waveform is therefore necessary.

Furthermore, the initialisation of pulses needs to be reproducible, i.e., the relative position of a control pulse w.r.t. a signal pulse should not change. The Ti:Sapph is synchronised to the repetition rate provided by the function generator using an internal lock-to-clock module. The AWG observes a tenth of this frequency from the secondary output of the function generator, about 10 MHz. We set the AWG, such that upon reception of the rising edge of the rectangular reference function the waveform is played. The waveform is then played until the next reference event appears. This also justifies the choice of rectangular pulses for the reference: the rising edge of the rectangular pulse has infinite slope at the voltage trigger level, compared to a finite slope of a sinusoidal rising edge. If there is a fluctuation in the trigger level of the AWG, an experimental imprecision that we suspect, the sinusoidal reference signal will lead to fluctuation in the initialisation of a waveform. Setting up the generation of control pulses in the outlined way, we are able to initialise pulses in a reproducible way and can guarantee temporal overlap with the signal pulses.

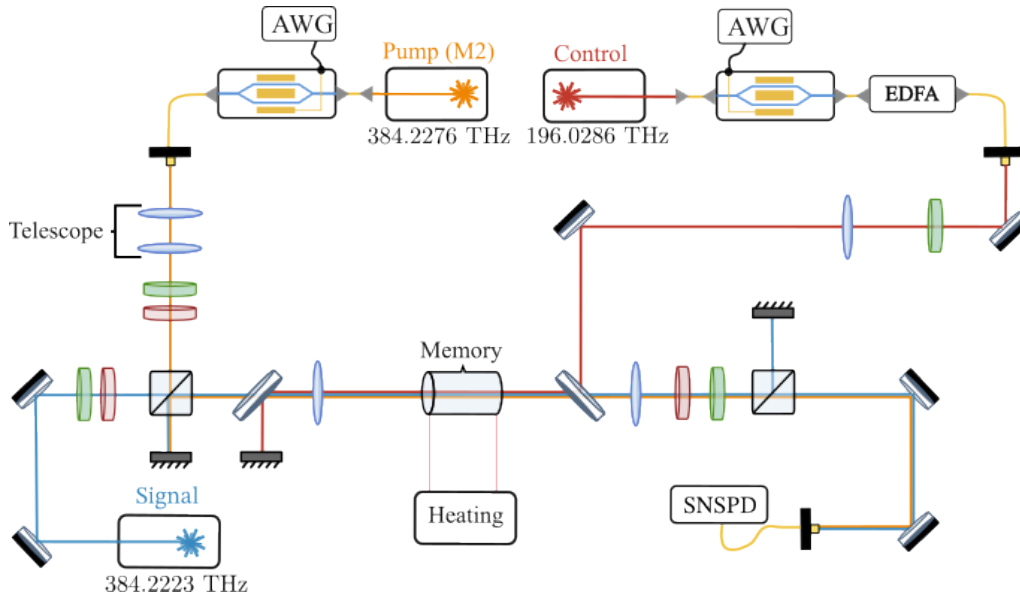
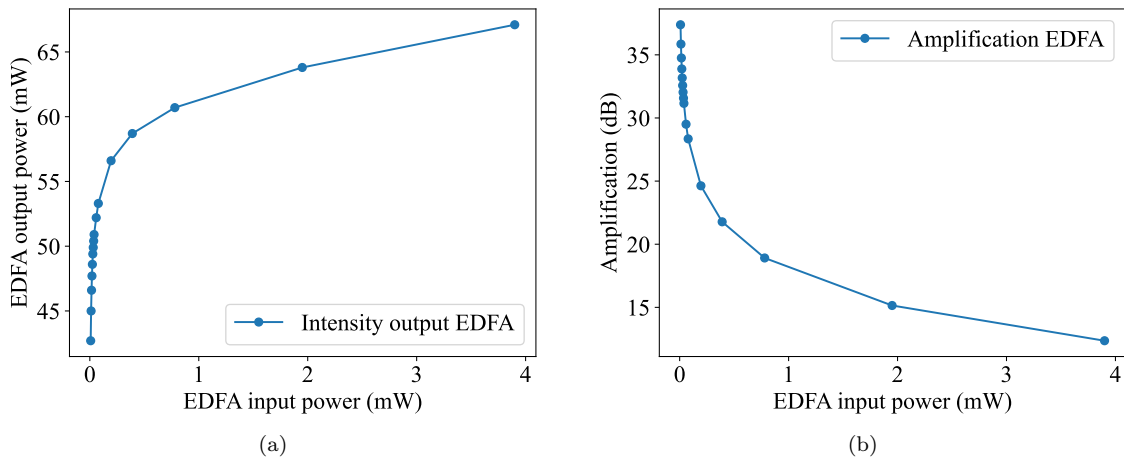
4.1.3 DRAGON

As already pointed out, a full implementation of DRAGON during this project was not possible due to delayed arrival of crucial components. Therefore, the setup presented here only shows the installed preliminary version of DRAGON.

Compared to ORCA (as shown in Fig. 4.1), the addition for DRAGON mainly consist in the installation for optical pumping.

4.1.4 EDFA

A crucial experimental instrument for both ORCA and DRAGON is the EDFA. The EDFA can amplify signals by pumping Erbium dopants in a fiber. Amplification is achieved via stimulated emission of light at the signal frequency. Due to the energy level structure of Erbium, most EDFAs

Figure 4.2: Installed DRAGON setup, no fields $M1$, $M2$.Figure 4.3: EDFA input intensity with (a) the amplified output and (b) the gain profile. The current is set to $A_{EDFA} = 500$ mA.

amplify in the telecom C-band.

In the setup depicted in Fig. 4.1 and 4.2, the EDFA is used to amplify the pulsed control light coming from the EOM. This is necessary to achieve high pulse powers, which are required for RI/RO efficiencies in the memory. The amplification is controlled via the EDFA current I_{EDFA} . An important feature of fiber-doped amplification is the gain saturation for high input intensities. A characterisation of the gain profile and saturation for the EDFA in use is shown in Fig. 4.3a and 4.3b. As we can see, the amplification drops quickly with input intensity.

Amplification of the CW background

The EDFA is interfaced with the EOM, which outputs the pulse sequence of the control light. The EOM carves pulses from the control CW light by alternating between high and low transmission, reaching maximum and minimum intensities EOM_{\max} and EOM_{\min} , respectively. Due to technical limitations, every EOM has a finite extinction ratio, defined by the ratio $r_{\text{EOM}} = EOM_{\max}/EOM_{\min}$. In this setup, we measured $r_{\text{EOM}} \approx 2500$. The main factor for a finite extinction ratio is a non-zero value of EOM_{\min} .

This implies that in between pulses there will still be transmission through the EOM. For a perfect EOM the transmission in between pulses would be zero.

This leakage is referred to as the CW background. Since the EDFA is ignorant about the pulse sequence, this CW background is also amplified. This leads to unwanted CW background light in the memory and is characterised in Section 4.2.2.

4.2 Operation of the memory

After the experimental setup has been introduced in the previous section, we here present the performance of memory operations.

This includes a characterisation of pulse energies, an estimation of the effect of CW background on memory efficiencies and the full operation of the memory, i.e., read-in and read-out processes.

4.2.1 Pulse energy characterisation

When it comes to the efficiency of the memory, the pulse energies for RI and RO control pulses play a key role. Higher pulse energies for the RI/RO pulses will increase RI/RO efficiencies, respectively. However, the efficiencies saturate at some point and effects of the ac-Stark shift become important [21] (see Sec. 4.3).

For DRAGON/ORCA, the control pulse powers are determined by a set of parameters.

1. **EDFA current I_{EDFA}** : the EDFA current determines the general amplification of pulses, but also of the CW background (see Sec. 4.1.4). As we show in Sec. 4.2.2, a current of 500 mA shows the best trade-off between CW amplification and pulse energies. All following measurements use $I_{\text{EDFA}} = 500$ mA.

2. **RI/RO amplitudes on AWG** $c_{\text{RI/RO}}$: the amplitudes of both pulses control their relative pulse energies and are determined on the AWG. The amplitudes are normalised s.t. an amplitude of $c_{\text{RI/RO}} = 1$ corresponds to the maximum voltage output of the AWG (at ± 0.25 V). We therefore choose $c_{\text{RI/RO}} \in [0, 1]$.
3. **Pulse separation** τ_{sep} : the separation between each pulse pair. This separation also influences the pulse power via the non-linear amplification behaviour of the EDFA. We choose $\tau_{\text{sep}} \in [50, 200]$ ns.

Due to the non-linear amplification of the EDFA, the choice of parameters can not be considered independently, i.e., the choice of amplitudes will affect the effective pulse power. For example, increasing c_{RO} while maintaining c_{RI} results in a reduction of RI pulse power, although the RI amplitude has not been changed.

In order to take these interdependencies into account, we present a heatmap of pulse energies for a range of separations $\tau_{\text{sep}} \in \{50, 100, 150, 200\}$ ns and amplitudes $c_{\text{RI/RO}} \in \{1/\sqrt{10}, \dots, 1\}$. The data is obtained by detecting the control pulses before entering the memory cell. The pulse energies for RI are shown in Fig. 4.4, the pulse energies for RO in 4.5.

We can clearly see how the the pulse energies of RI/RO depend on each other. As expected, an increase in RI pulse energy comes at a cost of reduced RO pulse energy.

From the presented mapping of pulse energies we cannot conclude a systematic amplification principle of the EDFA. In order to understand how the EDFA amplifies a certain sequence of pulses, we need to take into account the transient state of the Erbium dopants in the fiber. The amplification of the EDFA is based on stimulated emission, which requires population inversion beforehand. In the amplification of pulses we therefore need to take into account the time to repump.

These considerations are beyond the scope of this work. However, we can treat the EDFA as a black box and use the phenomenological behaviour of the amplification that is shown in the heatmaps in Fig. 4.4 and 4.5.

4.2.2 CW background characterisation

For the estimation of the CW background it is necessary to do a similar analysis as in Sec. 4.2.1. Since the gain of the EDFA changes with input power, the CW background will be different for different configurations of the pulse energies.

We show the CW background in mW for $\tau_{\text{sep}} = 50$ ns in Fig. 4.6. The highest background intensity

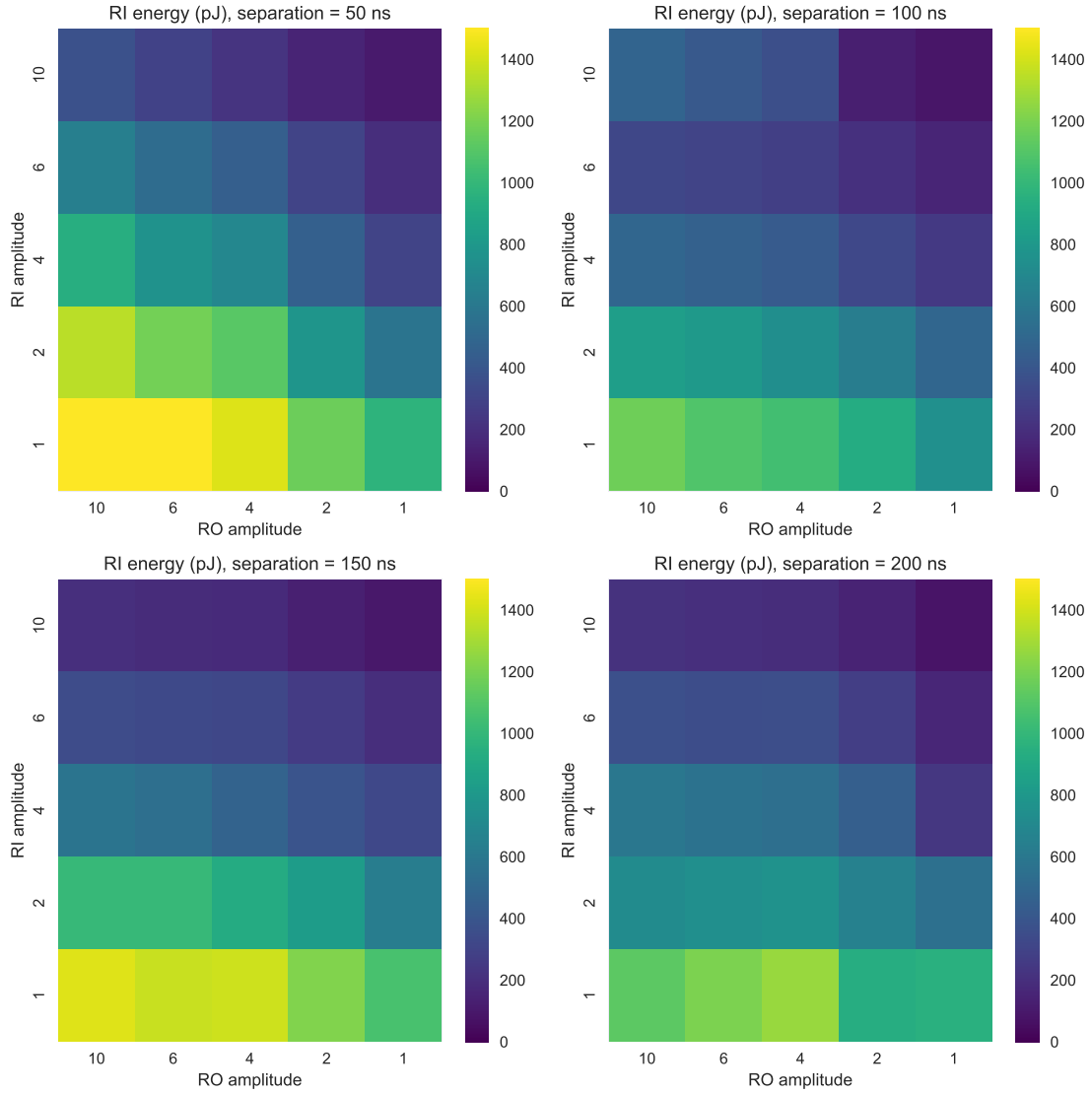


Figure 4.4: RI pulse energies for different pulse separations. The x-axis and y-axis show the RI and RO amplitudes, respectively, i.e., 10 denotes an amplitude of $1/\sqrt{10}$. The color bar denotes the pulse energies in pJ.

is measured for $c_{\text{RI/RO}} = 1/\sqrt{10}$. This is as expected, as for this configuration the input power into the EDFA is lowest and the amplification of the static background therefore is highest.

The CW background for other longer separations is higher for every configuration of amplitudes again because of the above mechanism.

4.2.3 CW leakage readout

In the discussion about memory operation in Section 4.2 the underlying assumption was that in the absence of light pulses no other light field was present. This is an assumption that no longer

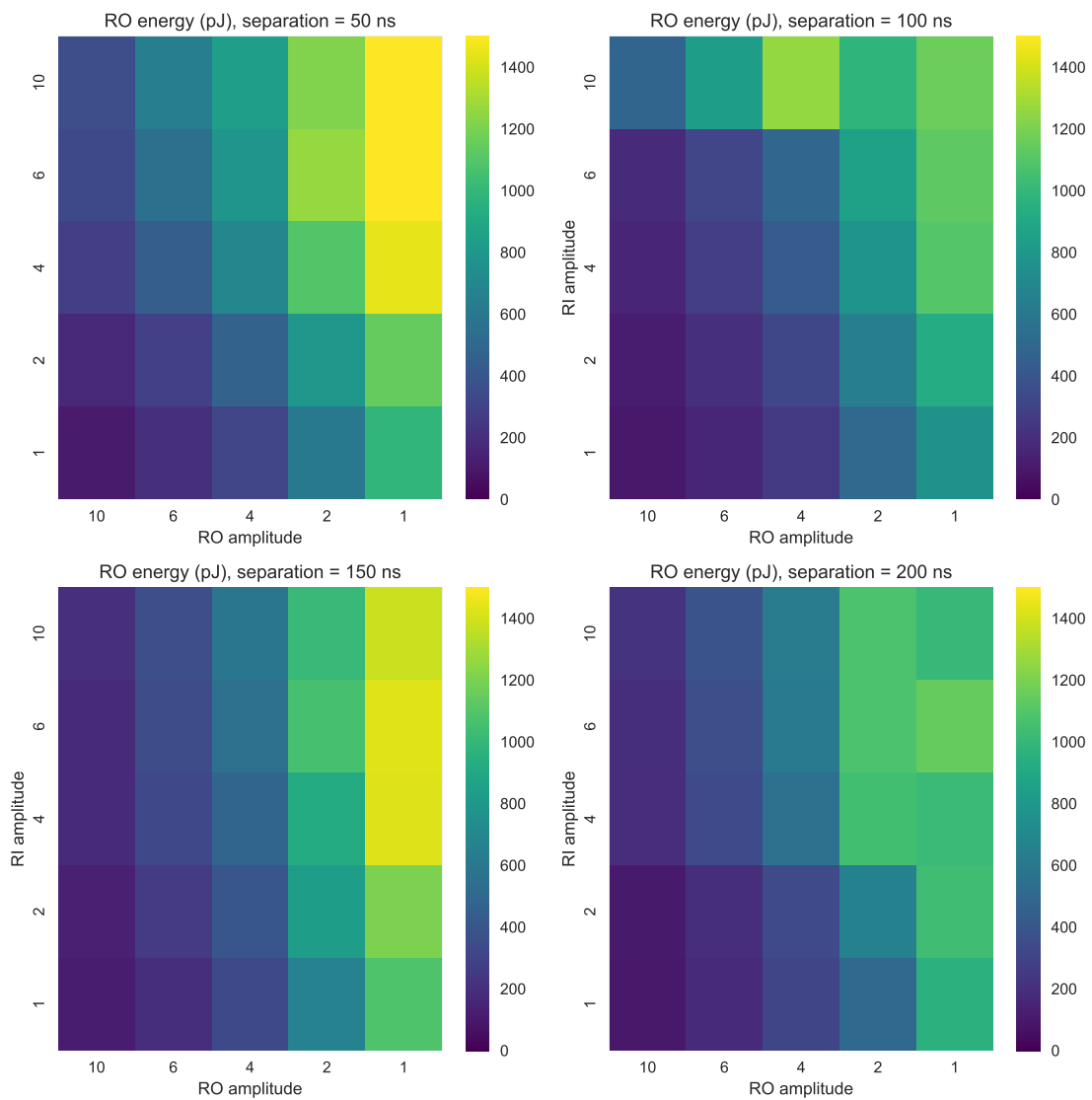


Figure 4.5: RO pulse energies for different pulse separations. The x-axis and y-axis show the RI and RO amplitudes, respectively, i.e., 10 denotes an amplitude of $1/\sqrt{10}$. The color bar denotes the pulse energies in pJ.

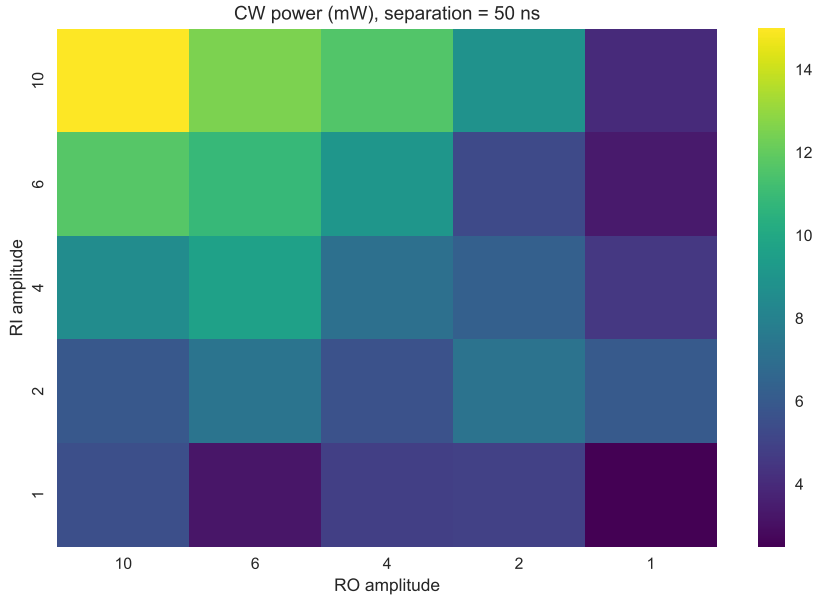


Figure 4.6: CW background intensity in mW for 50 ns separation. The x-axis and y-axis show the RI and RO amplitudes, respectively, i.e., 10 denotes an amplitude of $1/\sqrt{10}$. The color bar denotes the CW background power in mW.

holds if there is a CW background. This will change the dynamics of the memory.

As explained in Sec. 4.1.4, the amplification of the control pulses introduces unwanted CW light in between the pulses. This CW background couples the spin wave S_{gs} again to the signal light field \mathcal{E}_s and hence leads to read out of the memory.

In order to investigate the effect of such CW background on the readout, we engineer the waveform and the EDFA to vary the CW background while keeping all other parameters for read out approx. identical.

In the measurements we present in Tab. 4.1, we generated only the RI pulse with approx. constant pulse energy. The idea is to create a comparable spin wave while varying the CW background. The CW background is measured via the CW power P_{CW} .

τ_{sep} (ns)	I_{EDFA} (mA)	ϵ_{pulse} (pJ)	P_{CW}	η_{RI}
50	180	150.0	4.11	0.4771
100	140	152.0	2.71	0.5473
150	120	156.0	2.14	0.5511
200	110	152.0	1.72	0.5524

Table 4.1: Measurements for CW leakage investigation. τ_{sep} is the separation between RI pulses, I_{EDFA} is the EDFA current, ϵ_{pulse} is the estimated energy per pulse, P_{CW} the CW power and η_{RI} the RI efficiency.

As Tab. 4.1 shows, for a separation of $\tau_{sep} = 50$ ns we get more than twice the intensity for the CW background compared to a separation $\tau_{sep} = 200$ ns, while the RI efficiency and RI power

stay approximately constant.

To determine the read out from CW background qualitatively, we investigate the shape of the detected signal for the measurements in Tab. 4.1.

In Fig. 4.7 we see the detection events on the SNSPDs when signal and control pulses overlap, i.e., when signal is read in. The obvious difference in the displayed graphs is the height, which corresponds to the different read in pulse power. A high read in power results in high read in efficiency and hence a lower peak due to stronger absorption in the RI process.

If after read in there is no read out pulse sent into the cell, as it is in this case, no further signal should be detected. However, if there is a strong CW background we expect detection events after the read in. More precisely, we expect that the tail (see enlarged detail in Fig. 4.7) looks different for different CW background powers.

Investigating the tail we conclude that on the timescales accessible in these measurements no discernible effect of readout via CW leakage occurs. The different traces converge to the dark count detection level within a time of approx. 200 ps. We conclude that read out through CW leakage

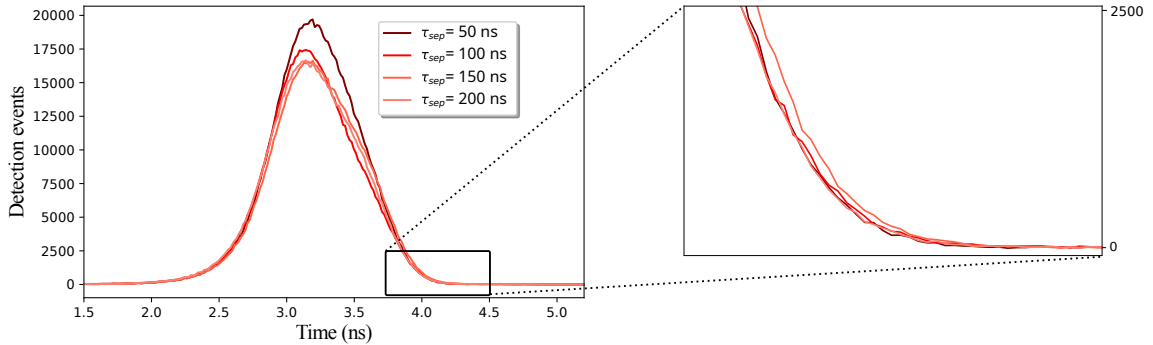


Figure 4.7: Detection of signal for read in for different separations τ_{sep} . The inlay shows a zoom of the right tail of the various traces.

of the control field poses no threat to read out efficiency for storage times on the order of few ns. From the conducted experiments we can not infer how this changes for larger storage times.

4.2.4 Retrieval of stored signals

The previous section dealt with experimental details in preparation for the actual memory operation. Here we will present first results of RI and RO and discuss the performance of the memory. Again, the presented results are not yet results for the full DRAGON protocol. What we show here is rather the telecom ORCA memory, onto which further functionalities of DRAGON will be added. As no rephasing is installed in the setup, the phase mismatch δk will not be reverted and

we expect only short lifetimes of the memory.

Measuring the memory performance requires the temporal overlay of the RI control pulse and the weak signal pulse, and the later RO control pulse to retrieve signal. The interplay of the optical fields with the atomic field of the memory is described in Sec. 2.1.5 and 2.1.9.

The signal field is detected with a SNSPD, as detailed in Sec. 4.1.1. In Fig. 4.8 we present the detected signal (blue curves) together with the input signal (orange curves) for different RI/RO pulse energies.

Fig. 4.8 illustrates how the efficiencies depend on pulse energies: as we decrease the RI pulse energy we observe a decrease in RI efficiency. However, we do not observe a similar behaviour for the RO. Although the RO pulse energy is increased, we do not observe an increase in η_{RO} . As we will explain and show in Sec. 4.3, due to energy dependent terms in the OBEs, the relation between pulse energy and efficiencies is not linear.

4

4.3 Simulation of optical Bloch equations

Using the OBEs that are described in some extent in Sec. 2.1.5 for ORCA, we can simulate the operation of the memory. The simulations serve as a sanity check of the experimental results from detection events at the SNSPDs, but also allow us to make predictions and choose parameters. If both the shape of the detected signal and the estimated efficiencies of experiment and simulation are close, the outlined theory describes the experimental reality well and no conceptual aspect of the memory is omitted. This is important if we want to use the theoretical framework to expand the experimental implementation and explore different parameter regimes. In the following we use and extend the simulation package *MEVeS*, which has been developed in the PQI group.

Inspecting Eqs. 2.51 and 2.52, we identify a few variables that can be tuned experimentally and are key parameters for the simulations. A detailed explanation of how these parameters are estimated and used in the simulations is provided in the following subsections.

4.3.1 Control Rabi frequency

The Rabi frequency Ω_c of the control field is defined in Eq. 2.39. For the RI pulse it directly affects the two-photon absorption in the read in process, for the RO pulse it influences the RO efficiency.

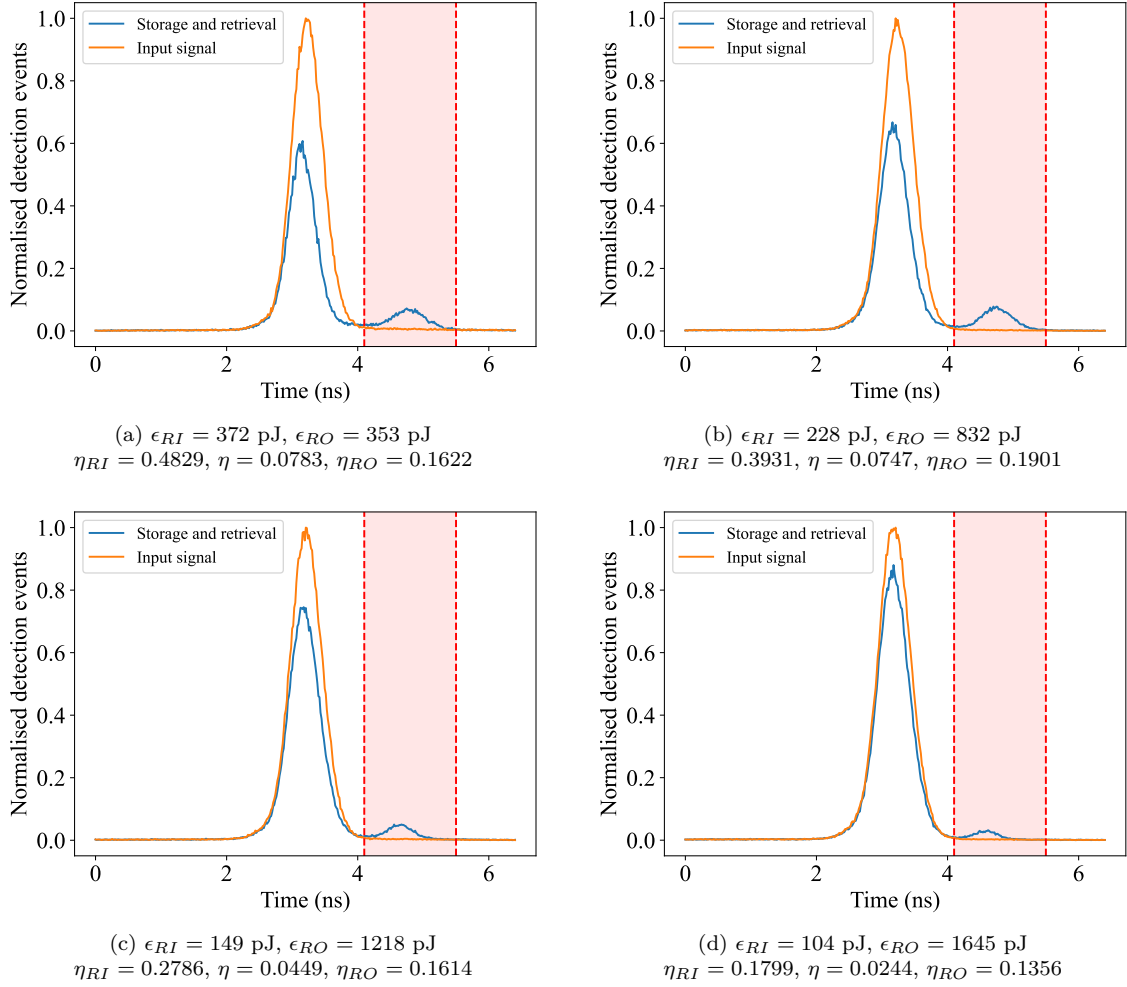


Figure 4.8: Storage and retrieval detection for 1.5 ns storage time with pulse energies $\epsilon_{RI/RO}$ and RI, total and RO efficiencies η_{RI} , η and η_{RO} , respectively. Vapour cell at $T \approx 66$ °C. The red shaded region indicates the integration region for the read out efficiency.

Experimentally we control the Ω_c via the pulse amplitude $c_{RI/RO}$ in the AWG waveform for the RI/RO control pulses, respectively.

We are not able to directly extract Ω_c . Instead we have to calculate the frequency from experimental values for the control pulse energies $\epsilon_{RI/RO}$ and the radius R of the control beam in the cell.

The Rabi frequency Ω_c for pulse energy ϵ , control beam radius R and temporal control profile $E_c(t)$ is derived from

$$\epsilon_0 = \left[\int dt 2c\epsilon_0 \hbar^2 \left(\frac{E_c(t)}{d_{es}} \right)^2 \right] \pi R^2 \quad (4.1)$$

$$\tilde{E}_c(t) = E_c(t) \sqrt{\epsilon/\epsilon_0} \quad (4.2)$$

$$\Omega_c = \max_t \tilde{E}_c(t). \quad (4.3)$$

Here $d_{es} = 4.604 \times 10^{-29}$ C m [32] is the reduced dipole element for the telecom transition of the control field, i.e., for the transition $|5P_{3/2}\rangle \rightarrow |4D_{5/2}\rangle$. It is important to point out that in the current implementation of DRAGON the control field is at a telecom wavelength and not the signal, as it is for the telecom ORCA. The reduced dipole element for the control field in telecom ORCA for ^{87}Rb is $d_{ge} = 3.583 \times 10^{-29}$ C m [26] for the transition $|5S_{1/2}\rangle \rightarrow |5P_{3/2}\rangle$. In DRAGON we therefore need less control field pulse energies to achieve the same Rabi frequencies.

From the above equations we also see that the Rabi frequency is inversely proportional to the radius and proportional to the pulse energy.

4

4.3.2 Optical depth

The OD determines the strength of light-matter interaction and affects both RI/RO efficiencies. This is evident in the OBEs for ORCA and DRAGON, where we see that the OD is an important parameter to couple the spin wave to the signal light field (see Eqs. 2.51 and 2.52).

The ensemble temperature is the experimental parameter that determines the optical depth d (see Sec. 2.2). However, since only temperature measurements on the cylindrical surface are possible, the effective temperature of the vapour will be different. A more precise estimation of the ensemble temperature can be obtained from spectrum fitting using *ElecSus* (see Sec. 3.4).

For the simulations, only the number density for atoms that are addressed by the signal field makes up the optical depth. Therefore, the numerical value for the optical depth as obtained from Eq. 2.65 only takes a fraction of the full number density in thermal equilibrium $N_i(T)$ into account, where i indicates the hyperfine state $F = 1, 2$. The population of the magnetic substates m_F is uniformly distributed, such that we have

$$N_i(T) = \frac{g_i}{g_1 + g_2} n_V(T), \quad (4.4)$$

where g_i is the degeneracy of the hyperfine state $|5S_{1/2}, F = i\rangle$ and $n_V(T)$ the total number density of a volume element at temperature T (following Sec. 2.2).

The ratio of atoms that participate in the signal transition therefore depends on the transition that is chosen for the signal field. Focusing on a signal field driving the transition $|5S_{1/2}, F = 2\rangle \rightarrow |5P_{3/2}\rangle$, we have $N_2(T) = \frac{5}{8} n_V(T)$. This reduction of the OD, which is due to a reduced participation of atoms in the ensemble, needs to be taken into account in the simulations.

4.3.3 Frequency detuning

The detuning of signal and control field $\Delta_{s,c}$ from the intermediate state reduce the transition strength of read in and read out processes. In particular, one can show that if the linewidth Γ_e (including homogeneous and inhomogeneous broadening) of the intermediate state is much smaller than the detuning Δ from the transition frequency, i.e., $\Delta \gg \Gamma_e$, the effective reduced dipole element reads [26]

$$|d_{eff}|^2 = \frac{1}{3} |\langle J || e\mathbf{r} || J' \rangle|^2 \quad (4.5)$$

In experiments and simulations we keep the detuning fixed to approximately 6 GHz by choosing the signal and control field frequencies accordingly.

4.3.4 Simulation of storage and retrieval

Using the same values for R , the optical depth d and the pulse energies $\epsilon_{RI/RO}$ as in the experiments in Fig. 4.8, we are able to reproduce the experimental findings using the simulation of the Bloch equations of the memory. This is shown in Fig. 4.9.

A direct comparison of the efficiencies and signal field leakage shows high consistency between simulation and experiment. However, there are some notable deviations.

First, we can observe an increased width of the intensity shapes in the experiment in Fig. 4.8. This increased width can be attributed to the limited time resolution of the photon detection device (*Swabian TimeTagger*). More precisely it is due to a time jitter of about ± 100 ps in the data acquisition device of the SNSPDs. This washes out features on small time scales and the general shape appears more like a Gaussian.

Second, the RO efficiency in the simulation deviates from the experimental estimate by a few percent. This can be explained by the temporal overlap of control and signal for the read in process and the resulting spatial shape of the created coherence S_{gs} .

The shape of the coherence, which is determined by the energy of the RI control pulse and its temporal overlay with the signal pulse, is the main factor for the RO efficiency.

We illustrate this relation by simulating the memory for different temporal offsets $\delta\tau$ between the signal and control pulses for RI. Varying the offset will change the shape of the coherence and thereby also the retrieval of light from the coherence. This can be seen in Fig. 4.10. The corresponding depiction of the pulse overlays can be found in Fig. A.2 in Appendix A.

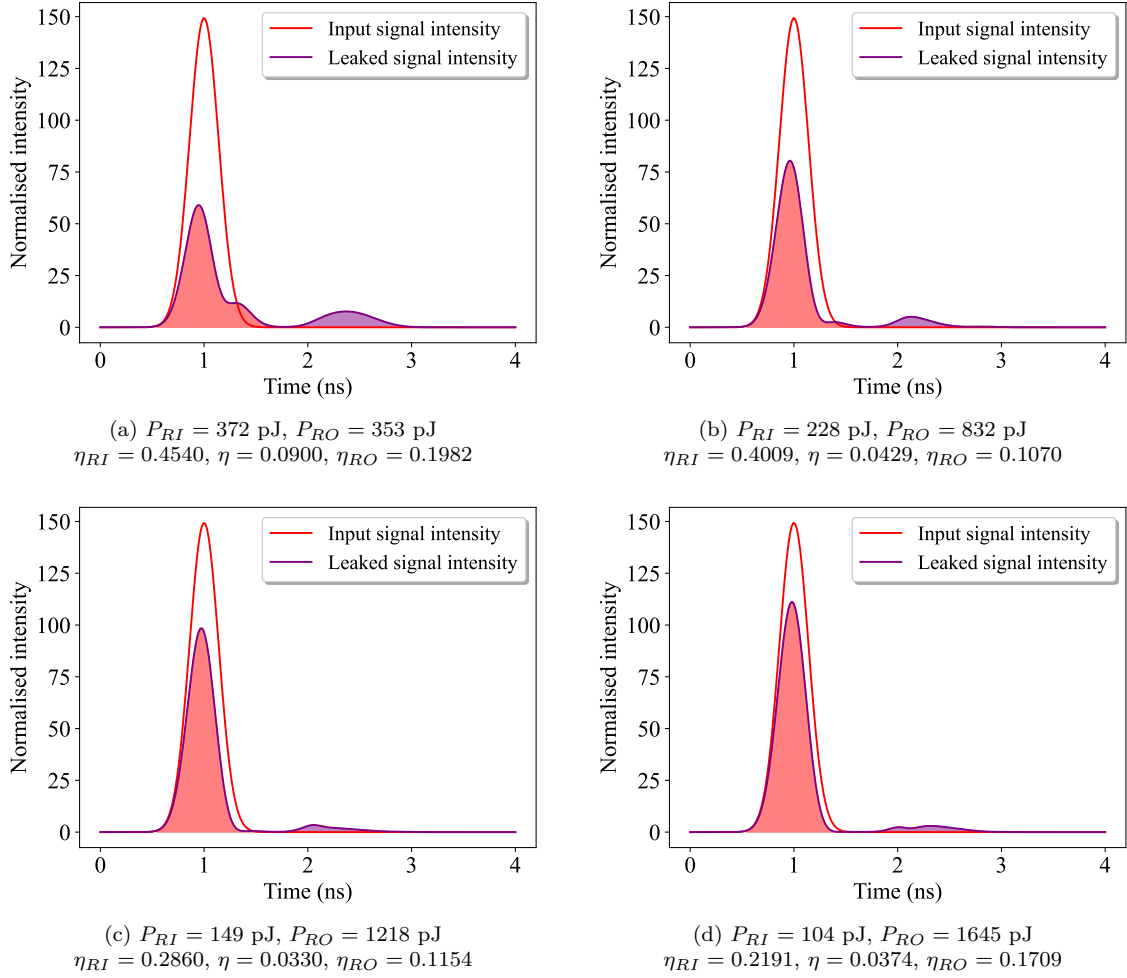


Figure 4.9: Simulation of signal and signal leakage for 1.5 ns storage time with pulse energies $\epsilon_{RI/RO}$ and RI, total and RO efficiencies η_{RI} , η and η_{RO} , respectively. Vapour cell at $T \approx 66$ °C. The red shaded region indicates the integration region for RI, the purple shaded region the RO region.

We see that the highest RO efficiencies are achieved for a delayed control pulse (red and light red traces). However, for these offsets the RI efficiency is also consistently smaller.

Focusing on the RO efficiencies, we see that there is an oscillation with increasing RO pulse power. This oscillation is similar for the different offsets $\delta\tau$. One explanation for the oscillation is that the read out pulse generates light that is read in again. Depending on the energy of the RO pulse, the retrieved light from the coherence can interfere more constructively or destructively.

A reason for the difference in RO efficiencies between experiment and simulation might be due to these oscillations. If the parameters are slightly different, a different RO efficiency is obtained due to the oscillations.

Another remarkable feature is the saturation in the RI efficiency with increasing RI pulse en-

ergy. As the energy increases, the frequency detuning due to the ac-Stark shift becomes stronger. At some point, the effect of a detuning from the transition is stronger than the effect of higher pulse energy. Hence we observe an optimum for the RI pulse energies.

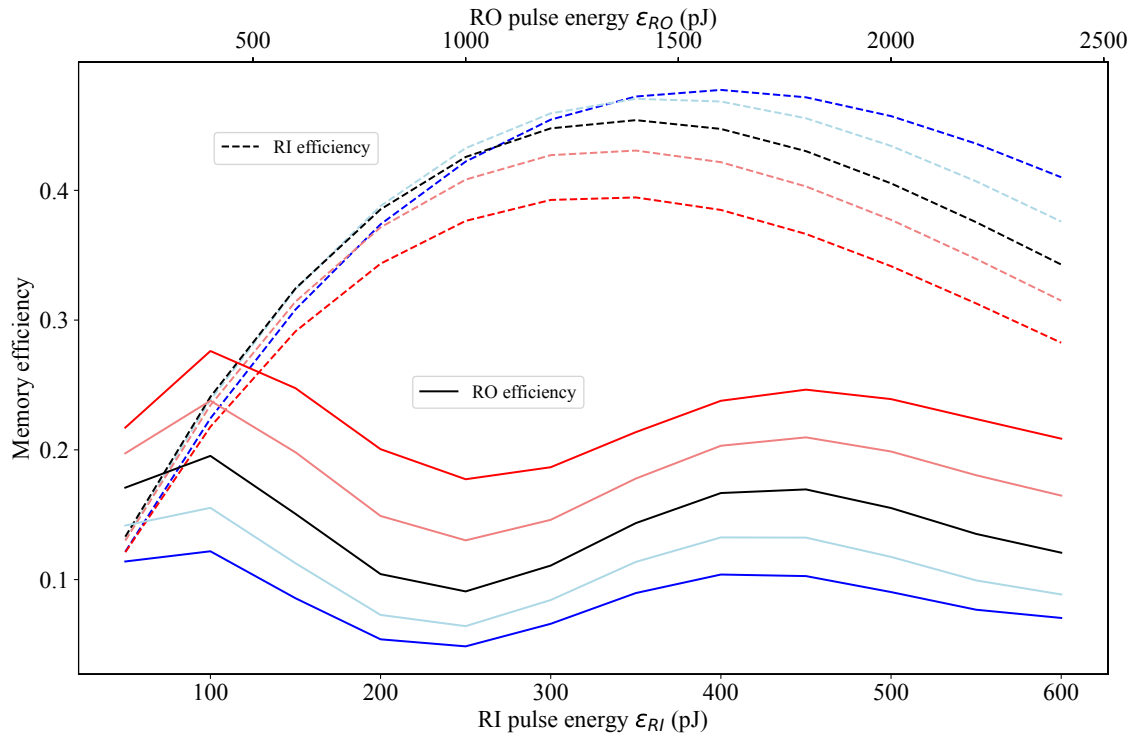


Figure 4.10: Simulation of the memory with RI and RO efficiencies as a function of RI and RO pulse energies. Red, light red, black, cyan and blue indicate an offset of $\delta\tau = 0.2$ ns, $\delta\tau = 0.1$ ns, $\delta\tau = 0$ ns, $\delta\tau = -0.1$ ns and $\delta\tau = -0.2$ ns, respectively.

Conclusions

This thesis introduced and discussed the various aspects of a novel ORCA-based memory platform, the DRAGON protocol. To this end, different experimental, numerical and theoretical questions have been introduced and addressed.

DRAGON has the ability to increase the lifetime of ORCA protocols by order of magnitudes by mapping the coherence to a stable ground state. Furthermore, we can control the Doppler dephasing with a pulsed rephasing mechanism.

However, the rephasing section also makes on-demand retrieval more complicated. A compromise regarding the advantages and disadvantages of DRAGON has to be made for each specific application.

Nonetheless, DRAGON allows us to explore the long lifetime performance of ORCA protocols.

In the future it will be interesting to explore how precise shaping of the control pulses affects the efficiencies. So far the analysis was limited to Gaussian pulses.

This project succeeded in implementing the basic function of DRAGON and to progress the theoretical and numerical understanding of the platform. However, due to the temporal limitation of the project and the lack of crucial components, no final operation of DRAGON could be presented.

A

Appendix

A

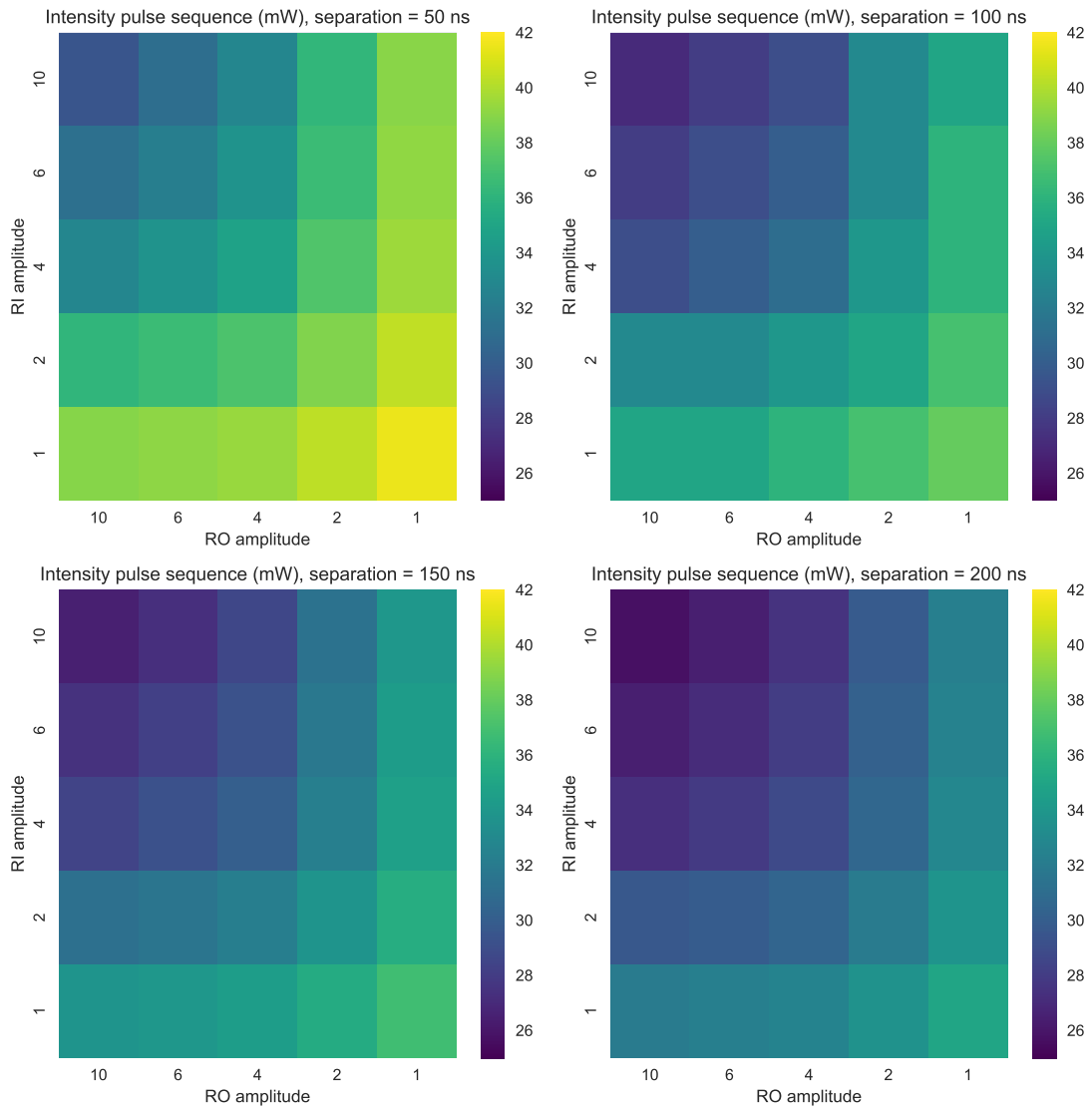


Figure A.1: Intensity of pulse sequence for different pulse separations.

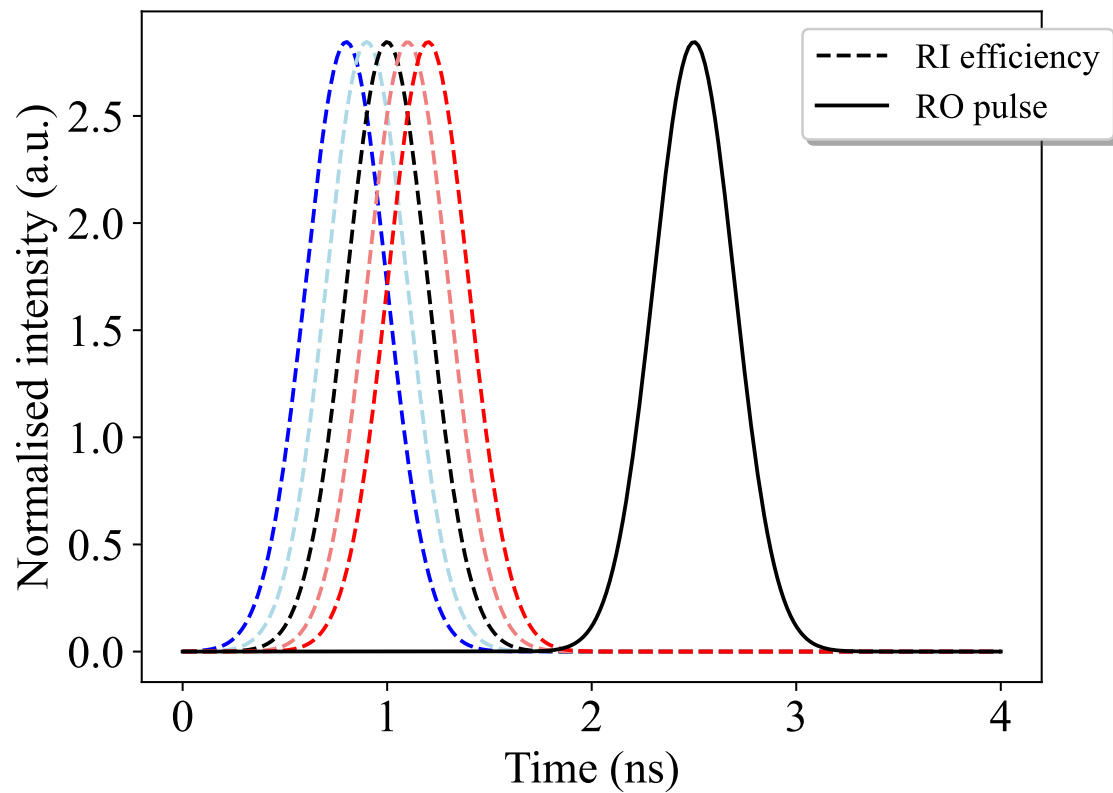


Figure A.2: RI control pulses (dashed, coloured) and signal pulse (solid). Red, light red, black, cyan and blue indicate an offset of $\delta\tau = 0.2$ ns, $\delta\tau = 0.1$ ns, $\delta\tau = 0$ ns, $\delta\tau = -0.1$ ns and $\delta\tau = -0.2$ ns, respectively.

A

B

Additional Appendix

B

B.1 Time bin qubit

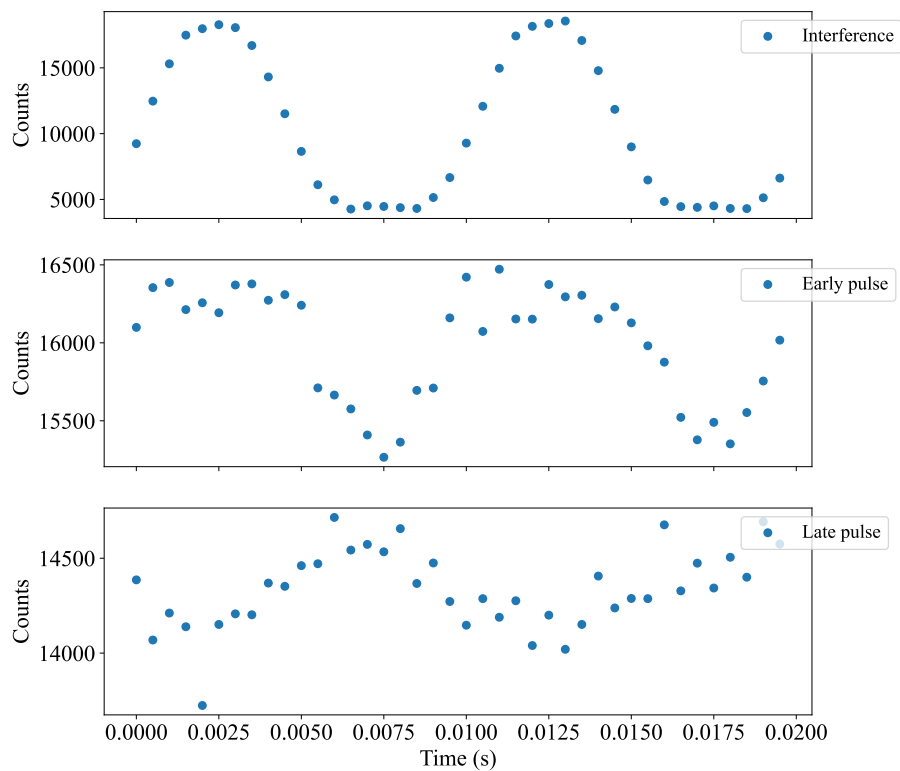


Figure B.1: Integration of photon counts for two full Piezo scans (2 ms). The upper graph shows the interference of the early and late pulse, the middle the transmission of the early pulse and the lower graph the transmission of the late pulse.

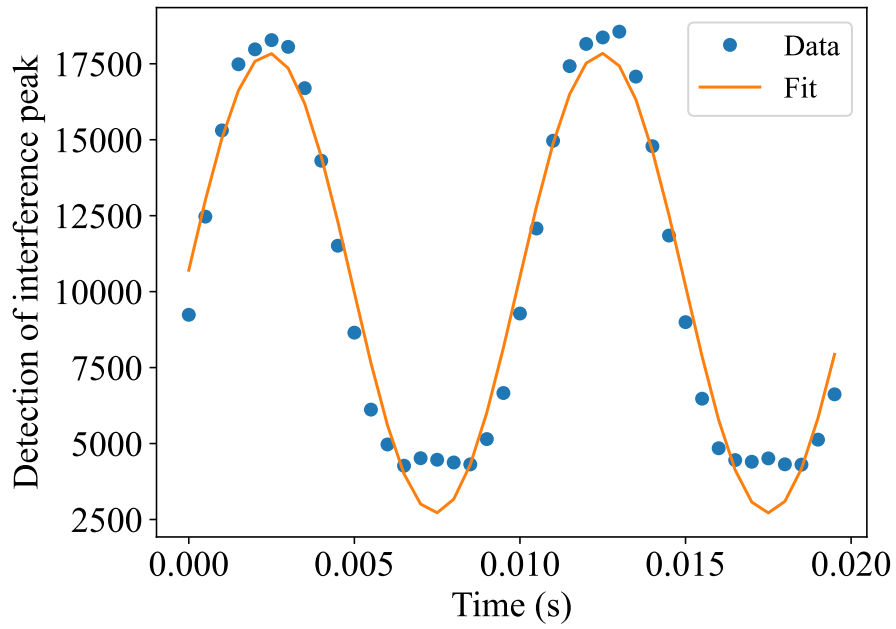


Figure B.2: Sinusoidal fit to the oscillation in the interference peak. The extracted frequency is 99.53 Hz with a visibility of 0.7356.

Bibliography

- [1] M. H. Devoret, M. H. Devoret, and R. J. Schoelkopf, “Superconducting circuits for quantum information: An outlook,” *Science*, vol. 339, pp. 1169–1174, 2013. [Online]. Available: <https://api.semanticscholar.org/CorpusID:10123022>.
- [2] H.-S. Zhong, Y.-H. Deng, J. Qin, *et al.*, “Phase-programmable gaussian boson sampling using stimulated squeezed light,” in *Optica Advanced Photonics Congress 2022*, Optica Publishing Group, 2022, ITu3B.1. DOI: 10.1364/IPRSN.2022.ITu3B.1. [Online]. Available: <https://opg.optica.org/abstract.cfm?URI=IPRSN-2022-ITu3B.1>.
- [3] N. Maring, A. Fyrrillas, M. Pont, *et al.*, “A versatile single-photon-based quantum computing platform,” *Nature Photonics*, vol. 18, no. 6, pp. 603–609, Jun. 2024. DOI: 10.1038/s41566-024-01403-4. arXiv: 2306.00874 [quant-ph].
- [4] K. Makino, Y. Hashimoto, J.-i. Yoshikawa, *et al.*, “Synchronization of optical photons for quantum information processing,” *Science Advances*, vol. 2, no. 5, e1501772, 2016. DOI: 10.1126/sciadv.1501772. eprint: <https://www.science.org/doi/pdf/10.1126/sciadv.1501772>. [Online]. Available: <https://www.science.org/doi/abs/10.1126/sciadv.1501772>.
- [5] C. L. Phillips, A. J. Brash, M. Godsland, *et al.*, *Purcell-enhanced single photons at telecom wavelengths from a quantum dot in a photonic crystal cavity*, 2023. arXiv: 2310.19701 [quant-ph]. [Online]. Available: <https://arxiv.org/abs/2310.19701>.
- [6] J. Nunn, N. K. Langford, W. S. Kolthammer, *et al.*, “Enhancing multiphoton rates with quantum memories,” *Phys. Rev. Lett.*, vol. 110, p. 133601, 13 Mar. 2013. DOI: 10.1103/PhysRevLett.110.133601. [Online]. Available: <https://link.aps.org/doi/10.1103/PhysRevLett.110.133601>.
- [7] D. Bouwmeester, J.-W. Pan, K. Mattle, M. Eibl, H. Weinfurter, and A. Zeilinger, “Experimental quantum teleportation,” *Nature*, vol. 390, no. 6660, pp. 575–579, Dec. 1997, ISSN: 1476-4687. DOI: 10.1038/37539. [Online]. Available: <http://dx.doi.org/10.1038/37539>.

-
- [8] N. Sangouard, C. Simon, H. de Riedmatten, and N. Gisin, “Quantum repeaters based on atomic ensembles and linear optics,” *Rev. Mod. Phys.*, vol. 83, pp. 33–80, 1 Mar. 2011. DOI: 10.1103/RevModPhys.83.33. [Online]. Available: <https://link.aps.org/doi/10.1103/RevModPhys.83.33>.
- [9] L.-M. Duan, M. D. Lukin, J. I. Cirac, and P. Zoller, “Long-distance quantum communication with atomic ensembles and linear optics,” *Nature*, vol. 414, no. 6862, pp. 413–418, Nov. 2001, ISSN: 1476-4687. DOI: 10.1038/35106500. [Online]. Available: <http://dx.doi.org/10.1038/35106500>.
- [10] C. M. Knaut, A. Suleymanzade, Y.-C. Wei, *et al.*, “Entanglement of nanophotonic quantum memory nodes in a telecom network,” *Nature*, vol. 629, no. 8012, pp. 573–578, May 2024, ISSN: 1476-4687. DOI: 10.1038/s41586-024-07252-z. [Online]. Available: <https://doi.org/10.1038/s41586-024-07252-z>.
- [11] J.-L. Liu, X.-Y. Luo, Y. Yu, *et al.*, “Creation of memory–memory entanglement in a metropolitan quantum network,” *Nature*, vol. 629, no. 8012, pp. 579–585, May 2024, ISSN: 1476-4687. DOI: 10.1038/s41586-024-07308-0. [Online]. Available: <https://doi.org/10.1038/s41586-024-07308-0>.
- [12] K. Shinbrough, D. R. Pearson, B. Fang, E. A. Goldschmidt, and V. O. Lorenz, “Chapter five - broadband quantum memory in atomic ensembles,” in *Advances in Atomic, Molecular, and Optical Physics*, ser. Advances In Atomic, Molecular, and Optical Physics, L. F. DiMauro, H. Perrin, and S. F. Yelin, Eds., vol. 72, Academic Press, 2023, pp. 297–360. DOI: <https://doi.org/10.1016/bs.aamop.2023.04.001>. [Online]. Available: <https://www.sciencedirect.com/science/article/pii/S1049250X23000010>.
- [13] Y.-F. Hsiao, P.-J. Tsai, H.-S. Chen, *et al.*, “Highly efficient coherent optical memory based on electromagnetically induced transparency,” *Phys. Rev. Lett.*, vol. 120, 2018.
- [14] G. Heinze, C. Hubrich, and T. Halfmann, “Stopped light and image storage by electromagnetically induced transparency up to the regime of one minute,” *Phys. Rev. Lett.*, vol. 111, p. 033601, 3 Jul. 2013. DOI: 10.1103/PhysRevLett.111.033601. [Online]. Available: <https://link.aps.org/doi/10.1103/PhysRevLett.111.033601>.
- [15] J. Wolters, G. Buser, A. Horsley, *et al.*, “Simple atomic quantum memory suitable for semiconductor quantum dot single photons,” *Phys. Rev. Lett.*, vol. 119, p. 060502, 6 Aug. 2017. DOI: 10.1103/PhysRevLett.119.060502. [Online]. Available: <https://link.aps.org/doi/10.1103/PhysRevLett.119.060502>.

-
- [16] A. Rastogi, E. Saglamyurek, T. Hrushevskiy, S. Hubele, and L. J. LeBlanc, “Discerning quantum memories based on electromagnetically-induced-transparency and autler-townes-splitting protocols,” *Physical Review A*, vol. 100, no. 1, Jul. 2019, ISSN: 2469-9934. DOI: 10.1103/PhysRevA.100.012314. [Online]. Available: <http://dx.doi.org/10.1103/PhysRevA.100.012314>.
- [17] J. Nunn, “Quantum memory in atomic ensembles,” Ph.D. dissertation, University of Oxford, 2008.
- [18] D. G. England, K. A. G. Fisher, J.-P. W. MacLean, *et al.*, “Storage and retrieval of thz-bandwidth single photons using a room-temperature diamond quantum memory,” *Phys. Rev. Lett.*, vol. 114, p. 053602, 5 Feb. 2015. DOI: 10.1103/PhysRevLett.114.053602. [Online]. Available: <https://link.aps.org/doi/10.1103/PhysRevLett.114.053602>.
- [19] K. T. Kaczmarek, P. M. Ledingham, B. Brecht, *et al.*, “High-speed noise-free optical quantum memory,” *Phys. Rev. A*, vol. 97, p. 042316, 4 Apr. 2018. DOI: 10.1103/PhysRevA.97.042316. [Online]. Available: <https://link.aps.org/doi/10.1103/PhysRevA.97.042316>.
- [20] J. Rowland, C. Perrella, A. N. Luiten, *et al.*, “High-bandwidth warm-atom quantum memory using hollow-core photonic crystal fibers,” *Phys. Rev. Appl.*, vol. 21, p. 014048, 1 Jan. 2024. DOI: 10.1103/PhysRevApplied.21.014048. [Online]. Available: <https://link.aps.org/doi/10.1103/PhysRevApplied.21.014048>.
- [21] S. Thomas, S. Sagona-Stophel, Z. Schofield, I. Walmsley, and P. Ledingham, “Single-photon-compatible telecommunications-band quantum memory in a hot atomic gas,” *Phys. Rev. Appl.*, vol. 19, p. L031005, 3 Mar. 2023. DOI: 10.1103/PhysRevApplied.19.L031005. [Online]. Available: <https://link.aps.org/doi/10.1103/PhysRevApplied.19.L031005>.
- [22] P. Burdekin, “Towards interfacing single photons emitted from dibenzoterrylene with rubidium ensemble quantum memories,” Ph.D. dissertation, Imperial College London, 2023.
- [23] K. T. Kaczmarek, “Orca: Towards an integrated noise-free quantum memory,” Ph.D. dissertation, University of Oxford, 2017.
- [24] J. Hu, W. Chen, Z. Vendeiro, H. Zhang, and V. Vuletić, “Entangled collective-spin states of atomic ensembles under nonuniform atom-light interaction,” *Phys. Rev. A*, vol. 92, p. 063816, 6 Dec. 2015. DOI: 10.1103/PhysRevA.92.063816. [Online]. Available: <https://link.aps.org/doi/10.1103/PhysRevA.92.063816>.

-
- [25] T. Champion, “Towards storage and retrieval of non-classical light in a broadband quantum memory - an investigation of free-space and cavity raman memories,” Ph.D. dissertation, University of Oxford, 2015.
- [26] D. Steck, “Rubidium 87 d line data,” Jan. 2003.
- [27] W. Dür, G. Vidal, and J. I. Cirac, “Three qubits can be entangled in two inequivalent ways,” *Phys. Rev. A*, vol. 62, p. 062314, 6 Nov. 2000. DOI: 10.1103/PhysRevA.62.062314. [Online]. Available: <https://link.aps.org/doi/10.1103/PhysRevA.62.062314>.
- [28] R. H. Dicke, “Coherence in spontaneous radiation processes,” *Phys. Rev.*, vol. 93, pp. 99–110, 1 Jan. 1954. DOI: 10.1103/PhysRev.93.99. [Online]. Available: <https://link.aps.org/doi/10.1103/PhysRev.93.99>.
- [29] R. Wiegner, J. von Zanthier, and G. S. Agarwal, “Quantum-interference-initiated superradiant and subradiant emission from entangled atoms,” *Phys. Rev. A*, vol. 84, p. 023805, 2 Aug. 2011. DOI: 10.1103/PhysRevA.84.023805. [Online]. Available: <https://link.aps.org/doi/10.1103/PhysRevA.84.023805>.
- [30] M. Himsworth and T. Freearge, “Rubidium pump-probe spectroscopy: Comparison between ab initio theory and experiment,” *Phys. Rev. A*, vol. 81, p. 023423, 2 Feb. 2010. DOI: 10.1103/PhysRevA.81.023423. [Online]. Available: <https://link.aps.org/doi/10.1103/PhysRevA.81.023423>.
- [31] M. A. Zentile, J. Keaveney, L. Weller, D. J. Whiting, C. S. Adams, and I. G. Hughes, “Elecsus: A program to calculate the electric susceptibility of an atomic ensemble,” *Computer Physics Communications*, vol. 189, pp. 162–174, 2015, ISSN: 0010-4655. DOI: <https://doi.org/10.1016/j.cpc.2014.11.023>. [Online]. Available: <https://www.sciencedirect.com/science/article/pii/S001046551400407X>.
- [32] P. Barakhshan, A. Marrs, A. Bhosale, B. Arora, R. Eigenmann, and M. S. Safronova, *Portal for High-Precision Atomic Data and Computation*.